Title
Applications of Synthetic Microchannel and Nanopore Systems

Author
Hinkle, Thomas Preston

Publication Date
2017

UNIVERSITY OF CALIFORNIA,
IRVINE

Applications of Synthetic Microchannel and Nanopore Systems

DISSERTATION

submitted in partial satisfaction of the requirements
for the degree of

DOCTOR OF PHILOSOPHY

in Physics

by

Thomas Preston Hinkle

Dissertation Committee:
Professor Zuzanna S. Siwy, Chair
Professor Ilya Krivorotov
Assistant Professor Jun Allard

2017

Figure 1.5 a
Adapted by permission from Macmillan Publishers Ltd: Siwy, Z.S. and Davenport, M. Nanopores: Graphene opens up to DNA. *Nature Nanotechnology*, **5**, 697-698, 2010, copyright 2010.
Figure 1.7 (left)
Reproduced from Howorka, S. and Siwy, Z.S. Nanopore analytics: sensing of single molecules, *Chemical Society Reviews*, **38**, 2360-2384, 2009. doi: `http://dx.doi.org/10.1039/B813796J` with permission of The Royal Society of Chemistry.
Figure 1.7 (right)
Adapted with permission from Yang, C., Hinkle, P, Menestrina, J., Vlassiouk, I.V., and Siwy, Z.S. Polarization of Gold in Nanopores Leads to Ion Current Rectification. *The Journal of Physical Chemistry Letters*, 7 (20), 4152-4158, 2016. DOI: 10.1021/acs.jpclett.6b01971. Copyright (2016) American Chemical Society.
Figure 2.2
Adapted with permission from Yang, C., Hinkle, P, Menestrina, J., Vlassiouk, I.V., and Siwy, Z.S. Polarization of Gold in Nanopores Leads to Ion Current Rectification. *The Journal of Physical Chemistry Letters*, 7 (20), 4152-4158, 2016. DOI: 10.1021/acs.jpclett.6b01971. Copyright (2016) American Chemical Society.
Chapter 3 figures
Figures from Qiu *et al.*, Pores with Longitudinal Irregularities Distinguish Objects by Shape. *ACS Nano*, 9 (4), 4390-4397 2015, DOI: 10.1021/acsnano.5b00877. Copyright 2015 American Chemical Society.
Figure 3.3 (right)
Adapted with permission from Pevarnik *et al.*, Polystyrene Particles Reveal Pore Substructure as they Translocate. *ACS Nano*, 6 (8), 7295-9302, 2012. DOI: 10.1021/nn302413u. Copyright 2012 American Chemical Society.
Figure 3.9 (left)
Image adapted from *Müller et al.* Electrochemical Synthesis of $\mathrm{Bi}_{1-x}\mathrm{Sb}_x$ Nanowires with Simultaneous Control on Size, Composition, and Surface Roughness. *Crystal Growth and Design.* 12, 615-621, 2012. Copyright 2012 American Chemical Society.

TABLE OF CONTENTS

LIST OF FIGURES

Page

LIST OF TABLES

ACKNOWLEDGMENTS

I would like to express my gratitude to my advisor Professor Zuzanna S. Siwy for accepting me into her research group and providing invaluable mentorship and guidance throughout my doctoral work.

I would also like to thank Professor Jun Allard and Professor Ilya Krivorotov for serving on both my advancement to candidacy and doctoral committees.

Throughout my PhD work there were many friends, coworkers, and mentors that helped me along the way. In particular, I would like to thank my lab mates for providing an intellectually stimulating, and often fun, environment in which to conduct research. Thanks to Alexandra Perebikovsky for photolithography training, and to David Mallin, Matthew Wallace, and Peter Taborek for lending their lab's equipment. Without their generosity, one of these projects would have been severely delayed.

I sincerely thank Professor Padhraic Smyth and the University of California, Irvine Data Science Initiative for a Summer fellowship that I was awarded, which supported me through some of the work presented in this dissertation and allowed me the opportunity to focus on data science and writing software over that time. Additionally, I thank the Beall Foundation for funding that supported me through the final year of my research, and the National Science Foundation for financial support earlier on in my PhD work.

CURRICULUM VITAE

Thomas Preston Hinkle

EDUCATION

Doctor of Philosophy in Physics **2017**
University of California, Irvine *Irvine, California*

Bachelor of Science in Physics **2011**
The Ohio State University *Columbus, Ohio*

RESEARCH EXPERIENCE

Graduate Student Researcher **2012–2017**
University of California, Irvine *Irvine, California*

TEACHING EXPERIENCE

Teaching Assistant **2012–2016**
University of California, Irvine *Irvine, California*

Teaching Assistant **2012**
The Ohio State University *Columbus, Ohio*

REFEREED JOURNAL PUBLICATIONS

P. Hinkle, T.M. Westerhof, Y. Qiu, D.J. Mallin, M.L. Wallace, E.L. Nelson, P. Taborek, and Z.S. Siwy. A hybrid resistive pulse-optical detection platform for microfluidic experiments. *Scientific Reports*, 7(1):10173, 2017.

C. Yang, P. Hinkle, J. Menestrina, I.V. Vlassiouk, and Z.S. Siwy. Polarization of gold in nanopores leads to ion current rectification. *J. Phys. Chem. Lett.*, 7(20):4152-4158, 2016.

Y. Qiu, P. Hinkle, C. Yang, H. E. Bakker, M. Schiel, H. Wang, D. Melnikov, M. Gracheva, M. E. Toimil-Molares, A. Imhof, and Z. S. Siwy. Pores with longitudinal irregularities distinguish objects by shape. *ACS Nano*, 9(4):43904397, 2015.

SOFTWARE

nanoIV `https://github.com/tphinkle/nanoIV`
Keithley 6487 Picoammeter control GUI program. Allows measurement of current-voltage and time-series data.

Pore stats `https://github.com/tphinkle/pore_stats`
GUI program and Python library for extracting and analyzing resistive pulse data.

Cell controller `https://github.com/tphinkle/cell_controller`
GUI program built in C++ and Qt for controlling Phantom high-speed camera, syringe pump, and NI-DAQ card simultaneously. Used to record data in simultaneous resistive pulse/imaging experiments.

ABSTRACT OF THE DISSERTATION

Applications of Synthetic Microchannel and Nanopore Systems

By

Thomas Preston Hinkle

Doctor of Philosophy in Physics

University of California, Irvine, 2017

Professor Zuzanna S. Siwy, Chair

This thesis describes research conducted on the physics and applications of micro- and nanoscale ion-conducting channels. Making use of the nanoscale physics that takes place in the vicinity of charged surfaces, there is the possibility that nanopores, holes on the order of 1 nm in size, could be used to make complex integrated ionic circuits. For inspiration on what such circuits could achieve we only need to look to biology systems, immensely complex machines that at their most basic level require precise control of ions and intercellular electric potentials to function. In order to contribute to the ever expanding field of nanopore research, we engineered novel hybrid insulator-conductor nanopores that behave analagously to ionic diodes, which allow passage of current flow in one direction but severely limit the current in the opposite direction. The experiments revealed that surface polarization of the conducting material can induce the formation of an electrical double layer in the same way static surface charges can. Furthermore, we showed that the hybrid device behaved similar to an ionic diode, and could see potential use as a standard rectifying element in ionic circuits.

Another application based on ion conducting channels is resistive pulse sensing, a single particle detection and characterization method. We present three main experiments that expand the capacity of resistive pulse sensing for particle characterization. First, we demonstrate how resistive pulse sensing in pores with longitudinal irregularities can be used to measure the lengths of individual nanoparticles. Then, we describe an entirely new hybrid approach to resistive pulse sensing, whereby the electrical measurements are combined with simultaneous optical imaging. The hybrid method allows for validation of the resistive pulse signals and will greatly contribute to their interpretability. We present experiments that explore some of the possibilities of the hybrid method. Then, building off the hybrid method we present experiments performed to measure single particle deformability with resistive pulse sensing. Using a novel microfluidic channel design, we were able to reproducibily induce bidirectional deformation of cells. We describe how these deformations could be detected with the resistive pulse signal alone, paving the way for resistive pulse sensing based cell deformability cytometers.

Chapter 1

Introduction

In the least specific terms possible, this dissertation is about ions, the atoms with either a surplus or deficit of electrons that you hear about in chemistry but seldom talk about in physics. When you put salt into water, the water molecules pull apart the ionic bonds holding the two elements together, leaving one of the atoms with a positive charge (cation) and the other with a negative charge (anion). These ions disperse evenly in the solution, and because each ion has a net charge and can move around, the solution is electrically conductive. Next, you can build a system with a conduit connecting two fluid reservoirs that are large in comparison to the conduit. If you apply a voltage difference across the conduit, the established potential difference will induce an ionic current to pass from one electrode to the other. The type of system we've just described is the ionic analogue of the most introductory circuit possible, a single resistor under an applied voltage. Despite its simplicity, this system forms the foundation of the topics that I worked on in the course of my PhD and that I will discuss in this dissertation. These projects fall into two categories:

1. developing novel nanoscale ionic channels, and
2. advancing resistive pulse sensing applications.

The conduit in the system described above is an ionic resistor, meaning that a voltage difference can occur across it and induce a magnitude of current to flow through it in proportion to its resistance value. If the channel is very large, the resistance can be calculated *via* $R = \rho \int \frac{dz}{A}$, where R is the resistance of the channel, ρ is the ion solution's resistivity, and A is the cross-sectional area of the channel. However, so far we haven't talked about the surface of the conduit itself. It turns out that if you immerse a surface in ionic solution, it is essentially guaranteed that the surface will at least have some electrical charge on it, and hence will also have a surface potential. Because the solution it is immersed in is conductive, mobile ions of the opposite charge polarity as the surface (the 'counterions') will flow towards the surface, and 'coions', will flow away. The complex that emerges is a tiny sheathe of solution that has a varying ion charge density, and is known as the electrical double layer. While this tiny sheathe is present on virtually *every* surface in contact with a conductive fluid, it goes completely unnoticed in our day-to-day lives. It's only when we build a version of the system described above where the conduit is approximately 100 nm or smaller—less than one-one-thousandth of the thickness of a human hair—that we begin to see any activity out of it. In fact, as we scale down further in size the influence of this tiny sheathe becomes increasingly important, and eventually even begins to dominate the behavior of the entire system! To find inspiration for why this is important, we only need to look at our own bodies. Our cells and their surroundings are completely immersed in water. We are filled with all sorts of different types of ions, each that is essential to our ability to function. The scale of the tiny machinery that keeps us running is at the scale where surface properties dominate over bulk. One particular type of machine that is integral to our functioning is the nanopore, a class of holes on the order of 1 nm in diameter that allow passage of ions and biological particles. There are a wide variety of biological nanopores, but one of their chief functions is in acting as a gate keeper, allowing passage of some particles while denying others. For instance, signalling in nerves is achieved when an 'action potential' is propagated down an axon cell by pores that open and close for certain types of ions. Again, this functionality is achieved through the surface properties of the pores; passive conductors with only bulk behavior cannot create this type of behavior. It is clear that by studying the effects of surface charge in ion channel systems, we gain better insight into how our biology functions. Aside from pure scientific research, we can also see these systems as inspiration for amazing feats that can be achieved through clever nanoscale engineering, and perhaps artificially create systems ourselves that exhibit complex functionality. On that note, the first subject of this thesis concerns the conductance properties of a particular type of nanopore that is composed of part insulating and part conducting material, and we discuss how the specific arrangement of surface charges on the pore surface leads to a novel conductance behavior.

So far we have seen that ion conducting channels are integral components of biological systems, and we have been focused on understanding the properties of the pores themselves. However, it turns out that there is a technique that can be used wherein ion channels are used as a *tool* that can be used to study the properties of small particles. In this technique, called resistive pulse sensing, our subject is the particle of interest, and not the channel itself. However, much stays the same. We are still interested in measuring the conductance of the channel, and when employing resistive pulse sensing at the nanoscale the behavior of the electrical double layer may still be important. Resistive pulse sensing comprises the bulk of this thesis. First, we describe a protocol for measuring the lengths of unknown particles using resistive pulse sensing, and summarize the mesoscale experiments that were conducted to test the protocol. Next, we introduce a new type of microscale resistive pulse sensing application where we augment electrical measurements with optics. We show that the hybrid platform can be used to validate the measurements in resistive pulse experiments. Following up on this project, we perform resistive pulse sensing experiments with biological cells, and describe how resistive pulse sensing may be used to detect the cells' deformability. The hybrid resistive pulse-optical imaging platform is employed to help us better understand how deformability can be measured in the resistive pulse signal.

In the rest of this introductory chapter I go over additional information that will be useful before tackling the rest of this thesis. First, I get into the underlying physics that is important to the systems I studied. This includes the physics of ion and solvent transport, electrodynamics, and the electrical double layer and its related phenomena. Next, I introduce and go over the theory for resistive pulse sensing, the particle sensing technique that is the focus of chapters 3-5 in this thesis. Finally, I introduce some background information on nanopores, and while it's not necessary for the rest of this thesis, it may be useful for understanding why nanopore research is important, and what motivated some of the projects I worked on.

1.1 Physics background

1.1.1 Ion transport

This thesis is about measuring the current through conductive channels, and that current originates due to the motion of the ions. Therefore, it's fundamentally important to understand which forces are responsible for this motion.

Diffusion

The most basic type of motion ions undergo is diffusion. Ions are immersed in a particle laden environment; in fact, the ions in solution have a mean-free path of less than a nanometer before they collide with other ions or water molecules, randomizing their velocity. For this reason, individual ions undergo Brownian motion, jittering about in random directions. In a solution of ions with constant number density everywhere, there is never any net motion. For every ion that vacates a region, there will be another ion to take its place. However, this changes if there are two connected regions with an ion number density imbalance. The individual ions still move about aimlessly, but *on average*, they flow from the region of high concentration to low concentration due to the imbalance. In physics terms, there is a net flux of ions between the two regions. The flux depends on how large the imbalance in concentration is and on how quickly the individual ions diffuse around. The equation for the flux of an ion species i due to diffusion is known as Fick's law,

$$\vec{j}_i^{\text{diffusion}} = -D_i \nabla c_i. \tag{1.1}$$

In the above equation (1.1), $\vec{j}_i$ is the flux of species i, D_i is the species' diffusion coefficient, and c_i the concentration of the ions. The diffusion coefficient is essentially a measure of how fast the ions diffuse about, which depends on their size and temperature, and on the viscosity of the solution surrounding them. The diffusion coefficient is given by the Stokes-Einstein equation

$$D_i = \frac{k_B T}{6\pi\eta r_i}, \tag{1.2}$$

where k_B is the Boltzmann constant, T the system temperature, η the viscosity of the solution, and r_i the solvation radius of the ion.

Convection

If the solvent in which the ions is dissolved is moving, it will carry the ions with it. In this type of transport, we consider the ions concentration to be a *passive scalar*—the scalar value of the concentration travels freely with the solution. This type of transport is called convection, and the flux due to it is straight forward:

$$\vec{j}_i^{\text{convection}} = \vec{u}c_i. \tag{1.3}$$

In the above equation, $\vec{u}$ is the velocity of the fluid. The motion of the fluid itself can be due to any number of forces in the system.

Electrophoresis

Electrophoresis, or electrical migration, is the motion of the charged ions due to the presence of an electric field. Interestingly, the *electrophoretic velocity* of the ions is proportional to the magnitude of the electric force they experience, which indicates that the ions move with terminal velocity. The proportionality constant is known as the electrophoretic mobility. The flux of ions due to electrophoresis is

$$\vec{j}_i^{\text{electrophoresis}} = c_i \mu_i^{ep} \vec{E}, \tag{1.4}$$

where the proportionality constant μ_i^{ep} is the electrophoretic mobility, and $\vec{E}$ is the electric field vector. There is a connection between the diffusion coefficient and the electrophoretic mobility, a result of the fluctuation-dissipation theorem, captured by the Einstein-Smoluchowski relationship

$$D_i = \frac{\mu_i^{ep} k_B T}{q_i}, \tag{1.5}$$

where q_i is the charge of the particle, which can be reexpressed in terms of the ion valency as $q_i = z_i e$.

Nernst-Planck equation

Diffusion, convection, and electrophoresis are the three most important forces relating to ion motion. Summing the three terms, we arrive at the Nernst-Planck equation for the total ion flux

$$\begin{aligned} \vec{j}_i &= \vec{j}_i^{\text{diffusion}} + \vec{j}_i^{\text{convection}} + \vec{j}_i^{\text{migration}} \\ \vec{j}_i &= -D_i \nabla c_i + \vec{u} c_i + c_i \mu_i^{ep} \vec{E}. \end{aligned} \tag{1.6}$$

In working with ion channels, we're primarily interested with the *current*, not the flux of ions. To calculate the current of an ion flux, we simply multiply the flux by the charge of the ion species, $q_i = z_i e$. Additionally, we're also interested in the total current across all species which we obtain with a simple sum. The total current density is then

$$\begin{aligned}\vec{J} = \sum_{i}^{\text{species}} \vec{J}_i &= \sum_{i}^{\text{species}} \vec{J}_i^{\text{diffusion}} + \vec{J}_i^{\text{convection}} + \vec{J}_i^{\text{migration}} \\ &= \sum_{i}^{\text{species}} -z_i e D_i \nabla c_i + z_i e \vec{u} c_i + z_i e c_i \mu_i^{ep} \vec{E}.\end{aligned} \tag{1.7}$$

In experiments, the electrophoretic term is usually the most important. Diffusion can play a role in ion transport processes, but only when large concentration gradients are built up in the system. In most nanopore experiments, we work with symmetric solution across the pore, and while local gradients may build up, the diffusive flux is still usually smaller than the electrophoretic flux. The convective term usually also ends up being insignificant in comparison with the electrophoretic contribution. Because convection means that ions are carried around passively, cations and anions flow in equal number and therefore there is no net flux. However, in regions that have a net fluid flow *and* a net charge density, convection does contribute to the electric current. As we will see, this effect occurs in the vicinity of charged surfaces, where the polarized electrical double layer is preferentially comprised of one polarity of ion. In exotic systems, such as carbon nanotubes, the convective current may even be the dominant contribution of the measured current.

1.1.2 The equations of fluid motion

Next we consider motion of the fluid itself. For systems large compared to the size of molecules, we make the approximation that the fluid is a continuous rather than discrete medium. In reality, we know that fluids are not continuous but are composed of discrete atoms and molecules, which may make this approximation seem limiting, especially in nanopore systems. For instance, one type of pore we present in this thesis can be as small as 10 nm, and using the approximation that a single element is 0.1Åin diameter, we see that the diameter of the pore is spanned by as little as 1000 atoms! Even at this level where we can make out individual atoms and molecules in the system, the continuum approximation still holds. In fact, the continuum approximation has been shown to accurately describe fluids all the way down to the scale of a single nanometer, and thus are valid in most systems of interest [4].

The Navier-Stokes equations

Under the continuum approximation, the equations of motion of the fluid are described by the Navier-Stokes equation. The Navier-Stokes equations are actually three coupled 2nd order non-linear partial differential equations that yield the fluid vector velocity $\vec{u}$. Despite the apparent complexity of the equations, they can be derived simply using Newton's 2nd law $\frac{d\vec{p}}{dt} = \vec{F}$ and basic conservation principles.

Consider an integrable quantity ϕ that is convected in a fluid field with velocity $\vec{u}$. For a given control volume, the continuity equation relates the time rate of change of ϕ in the volume with the flux through the boundaries due to convection in the fluid field and the of sources and sinks that create or consume the field. The continuity equation is

$$\frac{d}{dt}\int_V \phi dV = -\int_A \phi\vec{u}\cdot\hat{n}dA - \int_V sdV,$$

where dV is the control volume, dA its bounding surfaces, $\hat{n}$ the unit normal to the surface dA, and s are the sources and sinks present in the control volume, with the convention that sinks are positive and sources negative.

If we consider the conserved quantity to be the momentum $\rho\vec{u}$ and simplify the equation, we arrive at the Cauchy momentum equation:

$$\begin{aligned} \rho\frac{\partial\vec{u}}{\partial t} + \rho\vec{u}\cdot\vec{\nabla}\vec{u} &= \vec{s} \\ \rho\frac{D\vec{u}}{Dt} &= \vec{s}. \end{aligned} \tag{1.8}$$

The derivative $\frac{D}{Dt}$ in the second term is known as the 'material derivative', which describes the time rate of change of the velocity of a fluid parcel given that its change is time and position-dependent. Written in this way, we see that the equation for momentum continuity in the fluid leads us to a Newton's second law type expression. The term $\rho\vec{u}\cdot\vec{\nabla}\vec{u}$ is known as the convective term, and describes the transport of momentum due to motion of the flow-field itself.

Next, we replace the sources and sinks $\vec{s}$ with physical terms. Because the quantity of interest is momentum, we recognize that the sources and sinks must be forces (force densities) in the system, which can generally be broken down into forces that act on the body, such as those due to electrostatics or gravity, and forces that act on the bounding surface of the volume. Therefore, we replace the source/sink term with $\vec{s} = \vec{\nabla}\cdot\sigma + \sum_i \vec{f_i}$, where σ is the Cauchy stress tensor and $\vec{f_i}$ is a body force acting on the control volume. We can further break down the Cauchy stress tensor into the sum of two separate pieces, an isotropic, diaganol pressure tensor with elements p and the stress tensor τ due to *viscous* forces. For Newtonian fluids like water, there is a fundamental postulate that the stresses σ are proportional to the strain rates $(\nabla\vec{u})$, with proportionality constant equal to η, the viscosity of the fluid. In this case, $\tau = 2\eta\epsilon$, where ϵ is the strain rate tensor which describes the deformation of the fluid due to velocity gradients. When the stress tensor τ is replaced with the strain rate tensor ϵ via the constitutive relationship for Newtonian fluids, we finally arrive at the full Navier-Stokes equations:

$$\rho\frac{\partial\vec{u}}{\partial t}+\rho\vec{u}\cdot\nabla\vec{u}=-\nabla p+\eta\nabla^2\vec{u}+\sum_i\vec{f}_i. \tag{1.9}$$

Solving the Navier-Stokes equation subject to boundary conditions yields the correct fluid velocity $\vec{u}$ at all points in the system. While it is a complex equation, in many systems it can be simplified and solved analytically. In small channels (the subject of this entire thesis), the inertial/convective term $(\vec{u}\cdot\nabla)\,\vec{u}$ is often negligible and can be dropped as long as the fluid velocity is not too great. To quantify this notion, we introduce a dimensionless parameter called the Reynolds number:

$$Re=\frac{\rho uL}{\eta}. \tag{Reynolds number}$$

L in the above equation is the characteristic length scale of the flow, which in pores or channels is chosen to be the diameter by convention. The Reynolds number Re is essentially a ratio of the strength of inertial/convective forces relative to inertial forces. For high Reynolds numbers, convective forces dominate and we expect turbulent and chaotic flow. At low Reynolds number, inertial forces dominate and fluid motion is laminar and smooth. The Reynolds number is useful for knowing which two regimes we are in, and can provide intuition about the behavior of our systems. In microfluidic systems, we are seldom in the turbulent regime, and are often at medium to low Reynolds numbers. Nanofluidic systems are almost certainly non-inertial for reasonable external pressures.

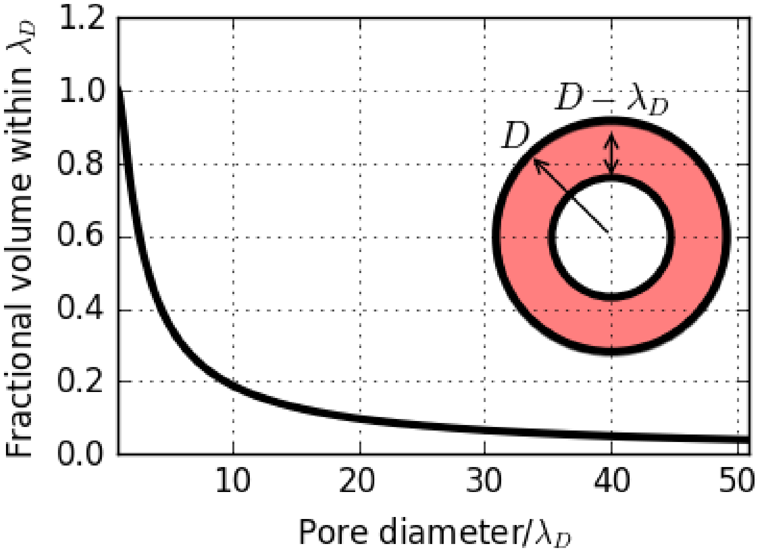

Figure 1.1: **Plot of fraction of volume in a nanopore that is within the EDL versus pore diameter.** The plot reveals a large super linear increase of total solution within the EDL as diameter decreases, starting at approximately $D \approx 10\lambda_D$.

1.1.3 The electrical double layer

As mentioned previously, when surfaces are immersed in solution they often acquire a finite surface charge, either by adsorption of charged components in the solution on to their surface, or through ionization of chemical surface groups native to their surface. In any case, the presence of this surface charge causes the ions in solution to redistribute themselves to screen the surface potential. This thin surface is known as the electrical double layer, and while its presence may seem trivial at first glance, it turns out that as we shrink our system size down more and more of the volume of the solution is contained in that thin layer. The structure of the electrical double layer is shown in Fig. 1.2. At some point, the electrical double layer begins to dominate the the behavior of the entire system. Figure 1.1 shows a plot of the fraction of volume in a nanopore that is within the EDL versus pore diameter. The electrical double layer is what leads to non-trivial conductance properties of the pore, and essentially is responsible for nanopores being a worthy field of study. In this section we will ‘derive’ the formation of the electrical double layer and review some of the phenomena associated with

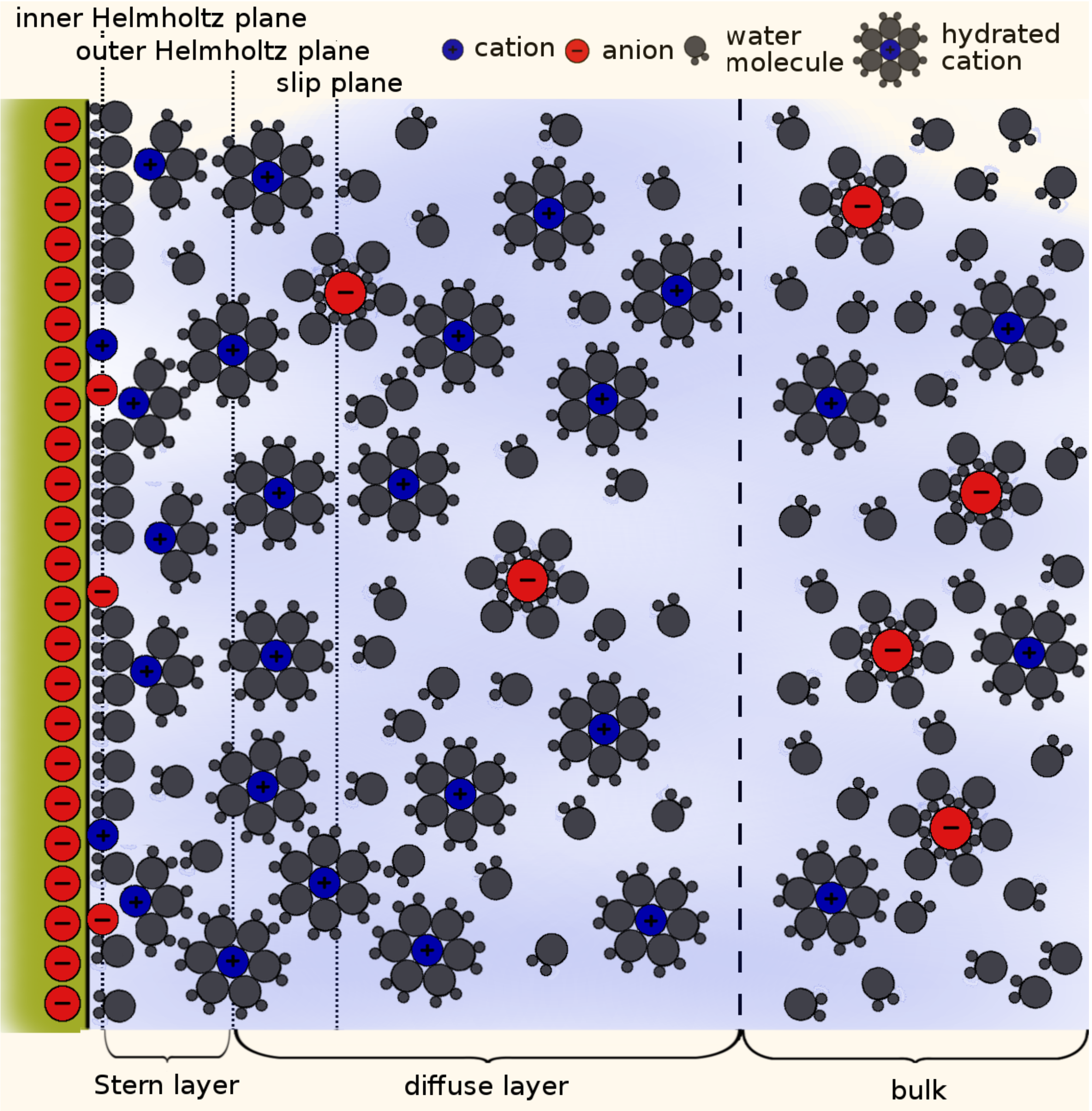

Figure 1.2: **Scheme of the electrical double layer under the Gouy-Chapman and Stern model.** There is an abundance of counterions near the pore surface and a reduced number of coions. Both species' concentrations are equal in the bulk.

its formation.

1.1.4 The diffuse layer—Poisson-Boltzmann equation

When any type of material is submitted in solution, charges tend to appear at the surface. Some of these charges are due to specific adsorption or immobilization of ions or molecules onto the surface, which give the surface some charge. The other charge type which is usually more significant is due to the ionization of chemical groups native to the surface of the pore. The type of chemical group present on the pore depends on the material out of which the pore is made. For instance, polymer pores prepared via the track-etch technique are formed when an etchant solution cleaves the polymer's monomer units in half. The chemical groups exposed during this etching procedure are often deprotonated at basic solution pHs, yielding an effective negative surface charge density. The electric potential due to all surface charges is known as the ζ potential.

Because the ion solution is conductive, mobile ions redistribute themselves near the charged surface to counter or 'screen' its $\zeta-$potential. This screening layer is known as the Debye layer or electrical double layer, and is characterized by an enriched number of counterions (ions of opposite charge polarity to the wall) and a depleted number of coions. As we will see, the electrical double layer has a characteristic length scale known as the Debye length λ_D, which ranges from $0.1 - 10$ nm for most solution concentrations. Figure 1.2 shows a scheme of the structure of hte electrical double layer.

The novel conductance properties of nanopores emerges when a non-negligible amount of the total volume is within a distance of λ_D of the pore wall. Figure 1.1 shows the fractional area of pore contained within λ_D of the pore wall as a function of the pore diameter D. For pores with diameter $D \gtrsim 10\lambda_D$, the total volume within the electrical double layer is negligible; however, below approximately $10\lambda_D$ the total volume within the EDL quickly increases. This explains why the ‘nano’ prefix in nanopore is important; as we approach the scale of the EDL, the structure of the solution very quickly changes, in a non-linear fashion, within the vicinity of a few nm of the pore wall.

In order to derive the appearance of the EDL, we consider the equations governing the distribution of ions in solution. In the solution, the ion species i have an electrostatic potential energy $U_i = z_i e\phi$, and have the following distribution in accordance with Boltzmann statistics

$$c_i = c_{0,i}\mathrm{e}^{-\frac{z_i e\phi}{k_B T}}. \tag{1.10}$$

The electric potential itself is given by the Poisson equation

$$\begin{aligned} \nabla^2\phi &= -\frac{\rho}{\epsilon} \\ \nabla^2\phi &= -\frac{1}{\epsilon}\sum_i z_i e c_i. \end{aligned} \tag{1.11}$$

Plugging the concentrations given by the Boltzmann equation into the Poisson equation, we arrive at the Poisson-Boltzmann equation

$$\nabla^2\phi = -\frac{1}{\epsilon}\sum_i z_i e c_{0,i}\mathrm{e}^{-\frac{z_i e\phi}{k_B T}}. \tag{1.12}$$

The Poisson-Boltzmann equation 1.12 is a second order non-linear differential equation for the electrostatic potential ϕ; after solving for ϕ, it can be plugged back into the Poisson equation 1.11 to obtain the ion concentrations c_i. The Poisson-Boltzmann equation is generally solved numerically, but analytic solutions exist for simplified assumptions about the geometry and magnitude of the electrostatic potential in the solution.

Consider a planar surface with unit normal pointing in the $\hat{y}-$ direction and uniform surface charge density σ immersed in a solution of water and symmetric ions with molar concentration $c_\pm$, valency $z_\pm = z$, and identical diffusion coefficients D_i. This ion configuration is a close approximation of a KCl electrolyte solution, a commonly used electrolyte in nanopore experiments due to the near-perfect symmetry of the ions. The ions have electrostatic potential energy given by $U_i = z_i \mathrm{e}\phi\left(y\right)$ where the electric potential ϕ is only a function of distance from the wall due to the system's symmetry. Under these assumptions, the Poisson-Boltzmann equation becomes

$$\frac{d^2\phi}{dy^2} = \frac{zec_0}{\epsilon}\left[\mathrm{e}^{ze\phi/k_BT} - \mathrm{e}^{-ze\phi/k_BT}\right]$$

Though the full solution can be solved analytically, a simple solution is obtained when we linearize the right hand side of the equation under the assumption $zec_0 \ll k_BT$ and apply the correct boundary conditions, an approximation known as the Debye-Hückel approximation. The solution is

$$\begin{aligned} \phi &= \phi_0 \mathrm{e}^{-\frac{y}{\lambda_D}} \\ c_i &= c_{i,0}\mathrm{e}^{-\frac{z_i e\phi_0}{k_BT}\mathrm{e}^{-y/\lambda_D}} \\ \lambda_D &= \sqrt{\frac{\epsilon k_BT}{2c_0z^2}}, \end{aligned} \tag{1.13}$$

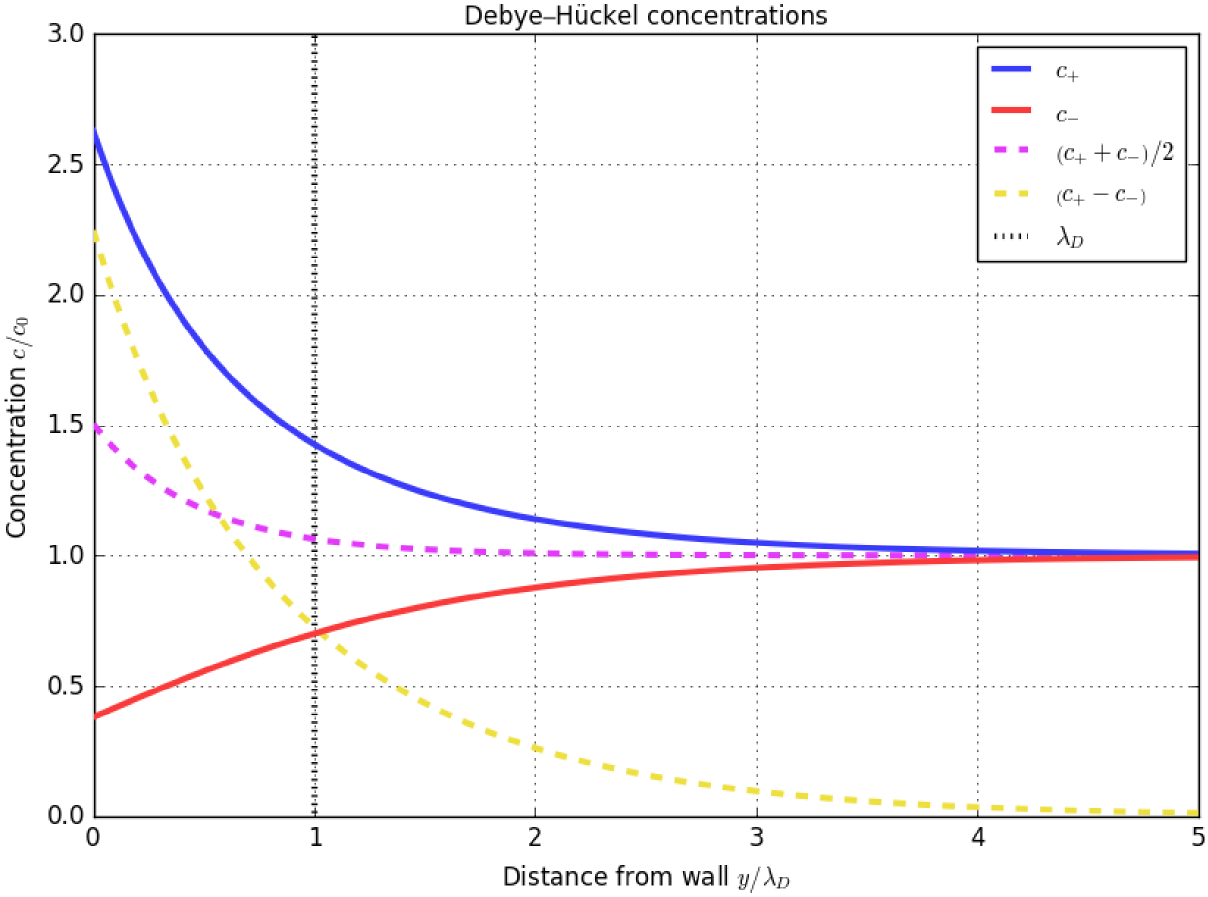

Figure 1.3: **Ion concentrations adjacent to a negatively charged surface according to the Debye-Huckel theory.** The plot reveals that the counterion concentration (blue) is enhanced near the wall, and decays approximately exponentially as distance from the wall increases. Oppositely, coions (red) are diminished near the wall. The *total* ion concentration at the pore surface is slightly higher than the total ion concentration in the bulk. The space charge density $\rho_E \propto [c_+(y) - c_-(y)]$ is non-zero near the wall, and decays to zero in the bulk.

where we introduced a new parameter, the Debye length λ_D. The solution to the 1-D lineared Poisson-Boltzmann equation reveals that the electrostatic potential exponentially decays away from the wall, that the counterion species are enriched at the surface, and the coions are diminished at the surface, but recover their concentration towards the bulk. The Debye length is perhaps the most useful parameter in nanopore systems since it gives a characteristic length scale for the region within the pore wall that departs from its bulk, ordinary behavior. The Debye length increases with dilute ion concentrations and decreases as the ion concentration is increased, and is typically somewhere in the range of $0.1 - 10$ nm for common solution preparations. Note that although we discussed the electrical double layer here in the context of a pore surface, nearly every body immersed in solution will have some surface charge and therefore its own electrical double layer. The electrical double layers of free-bodies i.e. particles are integral in explaining their motion in applied electrical fields.

The importance of the EDL in bestowing nanopores with their novel conductance properties cannot be overstated, and accordingly there are many phenomenon that arise as a direct consequence of the formation of the EDL. In the next few sections we will review some of these phenomena.

1.1.5 Electroosmosis

Ions migrate in externally applied electric fields, and ions of opposite polarity travel in opposite directions. When ions move, they tend to drag fluid along with them. In the bulk, this fact results in no net motion of fluid because for every anion that drags fluid in one direction, there is a cation that drags fluid in the opposite direction. These two effects cancel each other out so that there is no net motion of fluid. However, as we've just learned there *is* a net concentration of one ion polarity in the EDL, so we expect that an electric field applied parallel to a charged surface will induce motion of the fluid. This intuition turns out to be correct, and the effect is known as electroosmosis. Interestingly, although the effect originates due to the presence of the $\sim 1\,\text{nm}-$thick EDL, the induced fluid flow propagates into the bulk, and electroosmosis is observable in micro- and even milli-sized systems. This result, while surprising, is due to the simple viscous coupling of the fluid at the EDL surface to the rest of the fluid.

Because electroosmosis induces a general fluid flow, the effect couples with the motion of all unbound actors in the system, namely the ions species and any particles suspended in the solution. Electroosmosis in the bulk does not contribute any current due to the net charge neutrality there, however in the polarized electrical double layer, electroosmosis does contribute to the measured ionic current. This effect is usually small, but becomes increasingly important as the system size shrinks.

To understand electroosmosis, we look to the Navier-Stokes equations which describe the motion of fluids, and the Poisson-Boltzmann equation which yields the distribution of ions in the vicinity of the EDL. As an example, consider again an infinite charged plane with unit normal pointing in the $\hat{y}-$ direction, but this time with a constant electric field $\vec{E}$ applied parallel to its surface. The Navier-Stokes equation (eq 1.9) simplifies greatly in this case, and simply becomes

$$0 = \eta \frac{\partial^2 u}{\partial y^2} + \left[c_+\left(y\right) - c_-\left(y\right)\right] zeE_{ext}.$$

The equation shows that there is a momentum flux source term from the electric field acting on the charged solution in the EDL, which is proportional to the net charge in the solution (proportional to $c_+ - c_-$) times the electric field $\vec{E}$. The other term that balances the driving force is due to viscous forces between neighboring layers that have different $y-$ velocities u, i.e. due to velocity gradients perpendicular to the wall. In order to solve this equation, we can replace the charge density $\rho_E = ze\left(c_+ - c_-\right)$ with the Laplacian of the scalar potential ϕ via Ohm's law, and apply the correct boundary conditions. In the case of the infinite plane, the boundary conditions are that the fluid velocity equals zero exactly at the plane's surface (the 'non-slip' condition), and that the velocity gradients must disappear infinitely far away from the wall. Solving the equation, we arrive at

$$u = \frac{\epsilon E_{ext}}{\eta}\left(\phi - \zeta\right).$$

Interestingly, according to this equation the fluid velocity is proportional to the local electric potential in the screening layer, which is determined by solving the Poisson-Boltzmann equation (Eq. 1.12). Under the Debye-Hückel approximation of small surface potentials, the fluid velocity is zero at the walls, and exponentially approaches its bulk value as distance from the wall increases. This type of fluid flow profile is known as 'plug flow', since the velocity is approximately constant everywhere except in the thin EDL where there are sharp velocity gradients. Since the potential in the bulk is equal to $\phi = 0$, we find the bulk velocity to be equal to

$$\begin{aligned} u &= -\frac{\epsilon\zeta}{\eta}E_{ext} \\ u &= \mu_{EO}E_{ext}. \end{aligned} \tag{1.14}$$

The parameter $\mu_{EO} \equiv -\frac{\epsilon\zeta}{\eta}$ introduced is known as the electroosmotic mobility, and is the proportionality constant between the applied electrical field and the resulting fluid velocity. Typical values of the mobility are $\mu_{EO} = 10^{-8}\,[\mathrm{m}^2/\mathrm{Vs}]$ [25]. For reasonable values of the

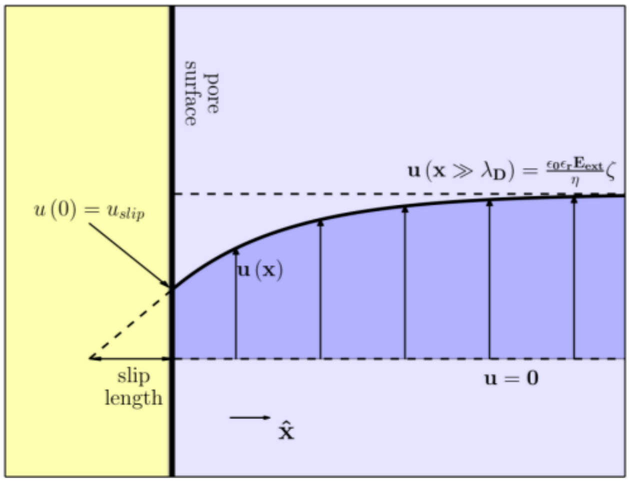

Figure 1.4: **Plot of electroosmotic flow along an infinite plane with finite slip length**. A net ion charge at the surface experiences a force in an electric field which drags fluid along with it. The force is only present in the electrical double layer, which viscously couples to the rest of the fluid. This fluid flow profile is known as plug flow, and extends far beyond the EDL where it originates.

electric field across a pore, this yields a fluid velocity of approximately 1 cm/s.

Figure 1.4 shows the fluid flow profile in a pore with a finite slip length u_{slip}; however, it must be noted that in the vast majority of experimental systems, $u_{\text{slip}} = 0$. It is possible to experimentally observe the fluid flow velocity, for instance by tracking the motion of small particles that move in the fluid flow, and therefore Eq. 1.14 provides a means for directly measuring the pore's $\zeta-$potential.

1.1.6 Surface conductance and conductance saturation

Ignoring electrical double layer effects, the conductance of an ion channel is proportional to the ion concentration in the solution; doubling the ion concentration exactly doubles the measured current. However, the presence of the electrical double layer breaks this perfect linear conductance relationship for two reasons. First, the total ion concentration in the EDL is greater than the ion concentration in the bulk, and thus the conductivity of EDL solution is greater than the conductivity of the bulk solution as well. Another important contribution to the measured current is the current from convection due to electroosmosis; because the EDL is polarized, fluid flow in that region contributes a convective contribution to the total ionic current. In total, under symmetric electrolyte conditions across the channel, there are three terms that contribute to the total current measured in a channel, migration of ions in the bulk, migration of the integrated ion *excess* in the EDL, and net convection of charge in the EDL due to electroosmosis. Without applying any equations, we can use what we learned about the EDL and some general logic to reason about what the current behavior should be in the limiting cases of very large ion concentration and very small ion concentration. The Debye length scales with bulk ion concentration like $\lambda_D \propto c_0^{-1/2}$; for very large ion concentration, the EDL should be negligible and therefore neither the effects of electroosmosis nor electrophoretic ion excess should be significant. At the other end of the scale, in the limit of nearly zero ions in the bulk we still must have charge neutrality in the pore, meaning a finite concentration of ions despite the bulk concentration being zero. In this case, the EDL fills the entire pore and the result is that the conductance is entirely due to the integrated excess and convective terms. This finite conductance at zero concentration is known as the *saturation current*. Therefore, as we increase the length of the EDL we expect the conductance discrepancy, the difference in bulk conductance versus conductance due to the two surface effects, to increase. The end result of all this is that the conductance is a non-linear function of ion concentration at sufficiently low ion concentration; removing ions past some point does not further reduce the conductance of the channel. Consider a nanopore immersed in solution of two symmetric ions denoted + and − (symmetric means their mobilities, valencies, and bulk concentrations are equal) with electrophoretic mobility μ_{EP} and electroosmotic mobility μ_{EP}. The following expression breaks down the total measured current into the three components described above:

$$
\begin{aligned}
&I = I_{\text{bulk}} + I_{\text{excess}} + I_{\text{EO}} \\
&I = \int 2c_0 \mu_{EP} Eez \, dA + \int \left[c_+ \left(z\right) + c_- \left(z\right) - 2c_0\right] \mu_{EP} Eez \, dA + \int \left[c_+ \left(z\right) - c_- \left(z\right)\right] u_{\text{EO}} \left(z\right) ez \, dA.
\end{aligned}
\tag{1.15}
$$

1.1.7 Ion selectivity

A phenomenon related to surface conductance is *ion selectivity.* Since the EDL has a higher concentration of counterions rather than coions, the total flux of ions through the pore is slightly skewed towards counterions. The ion selectivity is defined as

$$
S = \frac{|I_+ - I_-|}{I}. \tag{1.16}
$$

1.1.8 Ionic current rectification

An ion channel is said to be rectifying if its conductance for one voltage polarity is greater than the opposite voltage polarity. The presence of an EDL alone cannot account for this, since the system has symmetry with respect to switching the electrodes, and therefore no rectification will occur. However, by introducing asymmetry into a system, along with having the pore be partially ion selective, we can create rectifying pores. There are many ways to create asymmetric nanopores, but two obvious means are geometry and surface charge pattern based.

If the shape of a nanopore is asymmetric, for instance as in a cone, the ionic current will be rectified. A simple explanation for this is that at the tip-side of the pore (in the case of conical nanopores), there will be an excess of counterions in the vicinity of the entrance EDL, while the other side will more closely resemble the bulk. Because these ions are at the entrance of the pore, they will more easily enter the pore than when at the other side. The result is that for one voltage polarity the ionic current is greater than at the opposite polarity.

By similar reasoning, charge patterning asymmetry can also lead to rectification. By placing two charges of opposite polarity adjacent to one another inside the pore, for one voltage polarity a depletion zone is created in analogy with the depletion zone formed between the n- and p-doped regions in a semiconductor diode. The ionic current is rectified, and because the diode junction so severely limits the ionic current under one voltage polarity, the device is said to be equivalent to an ionic diode.[55]

Particle electrophoresis

Electrophoresis is the transport of a charged particle in the presence of an electric field. The effect of electrophoresis can be derived much in the way electroosmosis was derived, but instead of considering the fluid flow velocity at the surface of the particle to be zero, we set it equal to the electrophoretic velocity. For particles with thin electrical double layers (Debye-Hčkel approximation) and laminar flow (Stoke's flow), the particle velocity is

$$\begin{aligned} \vec{u} &= \frac{\epsilon \vec{E}_0}{\eta}\phi_0 = \mu_{\mathrm{EP}}\vec{E}_0 \\ \mu_{\mathrm{EP}} &= \frac{\epsilon\phi_0}{\eta}. \end{aligned} \tag{1.17}$$

In equation 1.17, we've again introduced a proportionality factor between the applied electric field E_0 and the induced velocity $\vec{u}$; this factor is known as the electrophoretic mobility. However, these equations are derived under the assumption that the applied electric field does not perturb the distribution of ions in the electrical double layer, which is only true for small surface potentials. If this assumption is invalid, additional effects related to the redistribution of ions must be taken into account; the net effect is a retarding force on the particle that slows its velocity.

Particle electrophoresis + electroosmosis

Transport of particles is in general a combination of electrophoretic and electroosmotic effects. Combining the two, the velocity of a charged particle translocating through a charged pore is

$$\begin{aligned} v &= \left(\mu_{EP} + \mu_{EO}\right) E, \\ v &= \frac{\epsilon}{\eta}\left(\zeta_{\text{particle}} - \zeta_{\text{pore}}\right) E \end{aligned} \tag{1.18}$$

In general the net velocity can be positive, negative, or zero depending on the relative sizes and signs of the electrophoretic mobility.

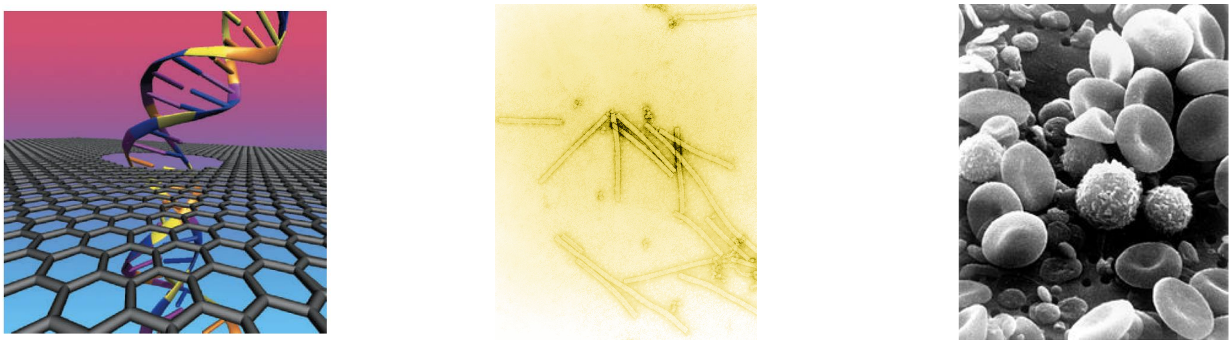

(a) **DNA passing through a graphene monolayer. Copyright: Adapted by permission from Macmillan Publishers Ltd: Siwy, Z.S. and Davenport, M. Nanopores: Graphene opens up to DNA. *Nature Nanotechnology*, 5, 697-698, 2010, copyright 2010.**

(b) **Tobacco mosaic virus.**

(c) **Blood cells. Image Credit: National Cancer Institute.**

Figure 1.5: **Three particles that can be studied with resistive pulse sensing.** The three systems span 4 orders of magnitude in size.

1.2 Resistive pulse sensing

1.2.1 Background

We finally arrive at resistive pulse sensing, which is the main topic of this thesis after the introduction and first chapter. Resistive pulse sensing is a method for particle detection and characterization. The first resistive pulse device was the Coulter counter and was used to size and count cells[6].

However, despite that resistive pulse sensing was originally proposed as a cell characterization platform, today it sees use in a wide variety of length scales and applications. For instance, resistive pulse sensing has been used to sequence DNA [22, 54, 57, 50, 12] ($\sim 1\,\mathrm{nm}$),

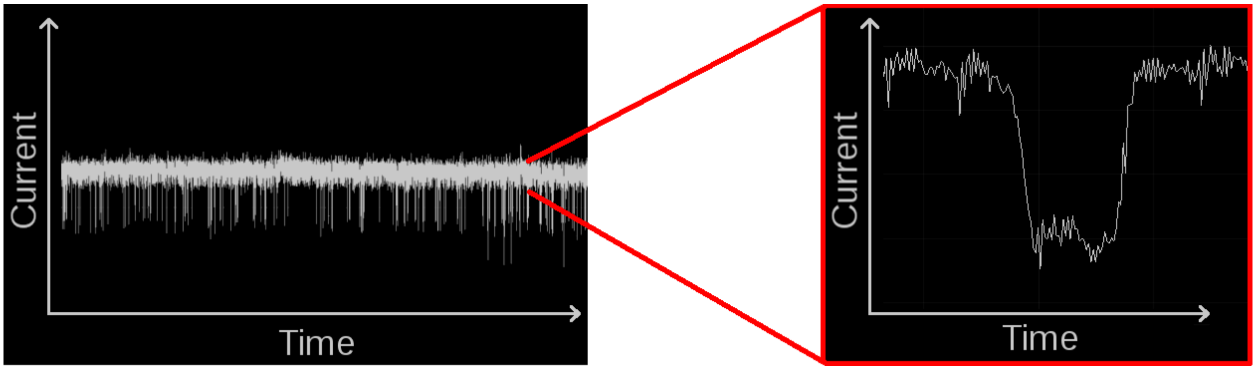

Figure 1.6: **Resistive pulse time series (left) along with a zoomed-in view of a single resistive pulse event (right).** Each spike in the signal on the left corresponds to the passage of a single particle through the channel or pore.

detect protein shape conformational changes [56] ($\sim 10\,\mathrm{nm}$), detect viruses [30, 9, 17, 59] ($\sim 100\,\mathrm{nm}$), measure the shape of aspherical nanoparticles [38] ($\sim 1000\,\mathrm{nm}$), and measure the properties of cells ($\sim 10\,000\,\mathrm{nm}$). These applications in total span four orders of magnitude! In order to understand how a single particle detection platform is viable in all these applications and scales, we need to go over the theory for how the method works.

1.2.2 Theory

As we've seen so far, ion conducting channels that span two reservoirs act as ionic resistors. When a voltage difference is applied across the channels, an ionic current develops inside the channel with magnitude given by the following (approximate) equation:

$$\begin{aligned} R_0 &= \int_{z=0}^{z=L} \rho \frac{L}{A} dz \\ &= \rho \frac{L}{A}, \end{aligned} \tag{1.19}$$

where R_0 is the resistance of the channel, L its length, and A its cross sectional area.

When a particle enters the channel, the system's resistance increases for two reasons. First, the particle occupies a region that would otherwise be occupied by conductive electrolyte, effectively decreasing the system's conductance. An additional effect for the increase in resistance is due to electrostatic boundary conditions imposed by the particle. Assuming the particle is insulating, the electric field lines must always be tangential to the surface in order for the normal components of the electric field to cancel. This distortion of the electric field lines means that their axial components decrease, reducing the measured current through the pore[7]. If the current is monitored during a resistive pulse experiment, whenever a particle enters the pore the current momentarily decreases while the particle transits. The properties of the dips, or 'pulses', may be related to the physical properties of the particles, including their size, shape, charge, and concentration[29]. Figure 1.6 shows a resistive pulse time series along with a zoomed in view of a single pulse. Perhaps the most useful equation for resistive pulse sensing is the equation for the amplitude of the dip when a spherical particle enters the channel:

$$\frac{\Delta R}{R_0} = \frac{3}{2}\left[1 - 0.8\left(\frac{d}{D}\right)^3\right]^{-1}\frac{v}{V}, \tag{1.20}$$

where ΔR is the changes in resistance when the particle enters the channel, d and D are the diameter of the particle and the pore, respectively, and v and V are their volumes. Notice that the expression contains a term that is the ratio of the volume of the particle to the channel; this term agrees with the basic intuition that the primary reason for the dip is due to the particle obscuring a volume that would otherwise contain conductive solution[7, 8]. The middle term enclosed in square brackets is known as the 'shape factor', and is a small corrective term that is mainly relevant for larger particles. In a typical resistive pulse experiment, the ionic current is monitored instead of the resistance. In this case, the resistance terms in equation 1.20 can be replaced with current via Ohm's law: $\Delta R/R_0 = \Delta I/I_p$, where I_p is the ionic current during the blockade. The utility in equation 1.20 is that it provides a means for sizing spherical or approximately spherical particles. Furthermore, due to the cubic dependence of the resistive pulse amplitude on the particle's diameter, the resistive pulses of particles strongly respond to their size. Even particles that are relatively close in size may be distinguished by their resistive pulse signals.

1.3 Nanopores

Unlike most physics jargon, the name nanopore is entirely self-explanatory. In fact, the following is a terse (but accurate) definition of a nanopore:

Definition 1.1. *A nanopore is a hole on the order of* $1\,\text{nm}$ *in size*

Nanopores generally belong to two classes, biological and synthetic. Because nanopores can be found in biology, many scientists are interested in studying them to gain a better understanding of their role in the natural world. On the other hand, nanopores, both biological and synthetic, can be used in a surprisingly large variety of applications, with the total count of such applications constantly increasing. In this section we will briefly discuss the types of biological nanopores and where they are found in nature, and then move on to describing different types of synthetic nanopores. Given the loose criteria required by the above definition 1.1 for something to be considered a nanopore, listing off every type of either biological or synthetic nanopores would be impossible; instead, I seek to introduce the most relevant types, with an admitted bias towards the types of nanopores I am most familiar with and that I have worked with in my research. After discussing the various types of nanopores, I will give a summary of some of the applications in which nanopores see use. Some of these applications, for instance resistive-pulse sensing, are a major part of this dissertation and will therefore be discussed in much greater detail later on. Other applications, such as DNA sequencing, are important enough to be mentioned but not discussed in significant detail. An extensive list of references, including those not explicitly referenced in this work, will be included should the reader wish to read more on a particular topic.

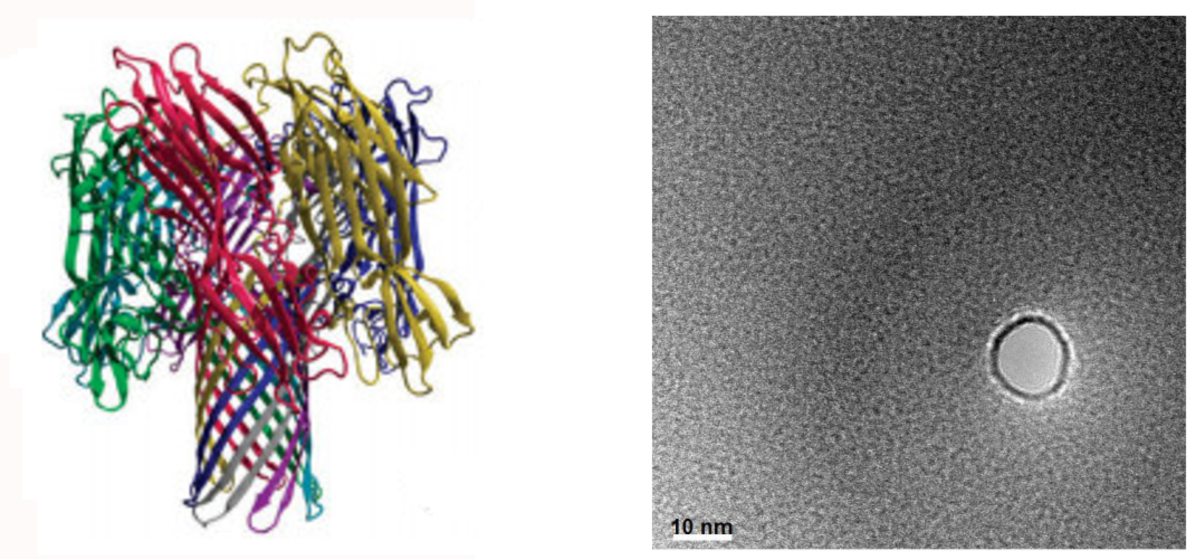

Figure 1.7: **Two types of nanopores. Left:** α-hemolysin, a biological type of nanopore approximately 1 nm in diameter. **Right:** A silicon nitride nanopore drilled using a transmission electron microscope (TEM), approximately 10 nm in diameter.

1.3.1 Biological nanopores

As mentioned before, nanopores exist naturally in biology. Their most important function is to enable passage from one region to another, much like a tunnel does; however, where a tunnel permits cars, trucks, etc., the passengers in nanopore systems are water, ions, proteins, etc. Nanopores typically connect regions that are necessarily divided in order for a cell to function. Membrane-bound nanopores are structures made out of protein that are embedded in a cell's lipid bilayer that connect the outside of a cell to the inside of a cell. They serve the useful function of regulating osmotic pressure by allowing water to enter and exit the cell, and also balance voltage differences by allowing passage of important electrolytes such as sodium, potassium, and chloride. Therefore, maintaining homeostasis is one of the chief functions of these types of nanopores. These pores also enable passage of messenger molecules that enable extracellular messenging, crucial to all multicelled organisms. Like lipid bilayer pores, there are also pores in the nuclear membrane that enable transport into and out of the nucleus of a cell. These pores' chief responsibility is to allow the passage of messenger molecules in and out of the nucleus.

The most fascinating property of nanopores is their capacity for active management of transport. For instance, some nanopores may open or close when the voltage difference across them surpasses a threshold; other types of nanopores are *ion selective*, permitting passage of some types of ions while denying passage to others. *Active* transport is absolutely crucial to biological systems; if all nanopores were passive holes that permitted anything to pass through, the system would equilibrate in a homogeneous, non-functional soup—life simply could not exist. Fortunately for us, nanopores are active transport regulators and life goes on. Going back to our tunnel analogy, nanopores act more like regulated tunnels, for instance some with guards that permit small cars only and deny trucks, or permit passage in only one direction, etc.

1.3.2 Synthetic nanopores

Advances in nano- and microfabrication have led to an enormous number of different types of synthetic nanopores. These pores can be made from a variety of different types of materials, and often their geometry (shape and size), as well as their surface chemistry properties, can be tailored to introduce specific types of behavior. However, the type of material used to make the nanopore most often determines the types of geometries and chemistries that are allowed. The following is a list of common types of nanopores, with a description of the type of material they are made from, their permissable length scales, and other miscellaneous relevant facts about them.

Monolayer pores. The invention of graphene, a monolayer of carbon atoms, and later MoS2, opened the possibility of creating nanopores with atomic thickness. These types of pores are created by punching through the thin monolayer, typically with an electron or ion beam. While still a very new field of study, these pores may see future use in desalination (removing electrolyte ions from water)[49].

Carbon nanotubes. A carbon nanotube can be conceptually understood as a rolled up tube of one or a stack of graphene layers. Graphene is a a monolayer of carbon atoms, and therefore a carbon nanotube itself is a type of pure crystal structure. The lattice arrangement of carbon atoms permits only certain tube diameters, which itself depends on the chirality of the tube (the way the tube is rolled up). Carbon nanotubes are interesting to researchers because of the exotic behaviors they exhibit that are not present in most other types of nanopores—for instance, they exhibit frictionless transport of water, hydrogen-dominant conductance (*via* the Grotthus mechanism), ion selectivity, and more. As of the submission of this dissertation, the use of CNTs as nanopore is still a new field of study, and the physical mechanism for the previously mentioned behaviors is still poorly understood. Nevertheless, the extreme confinement (1 nm and below for small CNTs) and the atomic-level precision of their structure are believed to be responsible. Another interesting aspect of the smallest CNTs is the breakdown of mean-field physics in describing their behavior. For instance, the Navier-Stokes equations which describe fluid dynamics, breaks down at this level because the water must be considered at the molecular level; the mean-field approach is no longer valid. Because they are still new, we do not yet know the exact applications that these nanopores will see use in. However, it is likely that they could be used in desalination applications (removing ions from water), or in ionic circuits as cation selective elements[41, 53, 5].

Silicon nitride. Silicon nitride is a type of crystalline semiconductor that permits engineering of nanopores through several different fabrication processes. Briefly, very thin layers of silicon nitride (e.g. $10 - 100$ nm) are grown, and a hole is bored through via either electron or ion beam milling. For instance, in one project of this dissertation I describe a project conducted with silicon nitride pores that were drilled via high-energy transmission electron microscope (TEM). Depending on the type of mill used (ion or electron), the size of these nanopores ranges, but the diameter is generally in the range of $1-100$ nm. One advantage of silicon nitride pores is their smooth interior geometries, as well as the native silane chemistry on the surface that permits many types of chemical modifications. These types of pores are used as ionic rectifiers (after modification), and in resistive pulse applications[48].

Glass nanopipettes. Quartz pipettes can be heated and slowly stretched, reducing the tip diameter with the possibility of reaching the nanoscale. Unlike the previously mentioned pores which all had an approximately cylindrical geometry, these nanopipettes have a conical shape. These pores have a couple advantages. First, the stretching process itself is simple and can be used to create many pores over a short amount of time. Second, the surface chemistry of the glass or quartz is amenable towards chemical modification. These pores may be used in ionic circuits, in resistive pulse sensing, or as a surface probe, by monitoring the current through the pipette as it approaches a charged surface.

Track-etched polymer nanopores. These types of pores are perhaps the most robust, dependable types of nanopores. Pore formation is a multistep process. First, untouched polymer membranes are irradiated by a single heavy isotope of an element such as gold and xenon, that has been accelerated to high speeds in a particle accelerator. The ion rips through the membrane, uniformly dispersing some of its kinetic energy into the surrounding polymer, and breaking the bonds in the polymer surrounding its trajectory. This location of damaged polymer bonds is known as the ‘damage track’. An ion detector is placed at the exit point of the membranes so that the beam can be switched off when a single ion is detected. This detection, along with a solid mask placed in front of the beam that blocks the vast majority of the ions in the beam, ensures that films that only have a single damage track can be prepared. This step, known as irradiation, must be performed off-site at a particle accelerator. After heavy ion irradiation, the membranes are immersed in an etchant solution such as NaOH or KOH. The etchant preferentially attacks the polymer in the damage track, clearing out the polymers along the track much faster than elsewhere in the membrane. Once the track has been etched out, the rest of the membrane is isotropically etched slowly by the NaOH. Pores prepared by the track-etch technique have a few advantages, including a customizable size and geometry. By putting etching solution on only one side of the membrane, it is possible to create conical pores of various aspect ratios. By applying a voltage across the pore during the etching process, the ionic current can be monitored and the etching process can be stopped at a particular current level, allowing the researcher customize the pore diameter. Another advantage of these pores is the carboxyl groups native to their surfaces, which permit many types of useful chemical modifications.

Hybrid biological-synthetic nanopores. Biological nanopores, such as alpha hemolysin, aerolysin, or MSPA to name a few, can be isolated from their host biological systems and inserted into synthetic systems, forming a hybrid biological-synthetic complex. In these cases, the pore is entirely biological, but the complex does not appear naturally in nature, and the pores may be used in engineering or scientific applications. To make matters even more confusing, such pores may also be genetically modified to change some of their behavior, meaning they are derived from biology but are synthesized in the lab. For instance, the company Oxford nanopore invented a genetically modified alpha hemolysin nanopore that is especially adept at differentiating between nucleotides, and is currently being used in DNA sequencing applications.

1.3.3 Applications

So far, I have hinted at or referred to nanopore applications without getting into specifics. Just as there are too many types of nanopores to enumerate, there are too many applications of nanopores to list them all off. This is a list of some of the most important applications of nanopores.

Analyte detection and characterization with the resistive pulse technique. Surprisingly, nanopores may be used as a sort of particle characterizer using something called the resistive pulse technique, which works as follows. A voltage is applied across the nanopore, which induces a measurable ionic current to flow through the channel. If a particle enters the nanopore, the particle will occupy a volume that otherwise would be occupied by high-conductivity ions, increasing the pore's resistance, and decreasing the measured current. It turns out that by studying the nature of the decrease in the current, we can gather some information about the transiting particle. For instance, by counting the number of pulses in the measured ionic current, we can determine the concentration of particles in the suspension. The size of the particle can be determined by relating it to the depth of the pulse—larger particles block the current to a larger degree, and therefore create deeper resistive pulses. If the particle is at least partially driven through the channel *via* electrophoresis (discussed later), then the particle's surface charge can be determined by the length of the pulse, or 'dwell time' of the particle.

One advantage of resistive pulse sensing is its scale-independence, which is a result of the generality of the physics involved. For this reason, resistive pulse sensing has been used in a large number of applications. The original use of the resistive pulse technique was in performing red blood cell counts (channel size approximately $\sim 100\,\mu$m which was achieved by Coulter in 1953; this is the reason why sometimes the resistive pulse technique is referred to as the Coulter counter priniciple, or simply the Coulter principle. Since Coulter's original design, the resistive pulse technique has been used in counting smaller specimens such as exosomes, proteins, and viruses, used to measure particle rigidity, and perhaps most importantly, in DNA sequencing. The basic idea of resistive-pulse sensing for DNA sequencing is that the four types of nucleotides have slightly different sizes, and therefore lead to four unique current blockages. DNA can be slowly threaded through a nanopore while the current is monitored, and the discrete states in the resulting time-series of the measured current yield the sequence of DNA.

Water desalination. Charged nanopores are slightly ion selective, meaning they preferentially allow one polarity of charge over another to pass through. If one side of a nanopore membrane is filled with electrolyte solution and a pressure is applied, water will pass through the pore, and due to the selectivity of the membrane, fewer ions will pass through than are contained in the bulk. In this way, nanopores can be used for water desalination. This mechanism of salt rejection is electrostatic, since the finite potential in the vicinity of the pore walls is responsible for screening ions. Traditional water desalination relies on reverse osmosis membranes that are completely impermeable to salts, and therefore *sterically* reject ions. In future sections we will discuss the physics involved with water desalination.

Nanopore ionics and ionic circuits. Ion transport is fundamentally important to all cellular life. At the most basic level, single cells maintain homeostasis with their environment by maintaining a careful balance of salt ions across their membranes. This balance is regulated by a rich variety of ion channels, each with their own specific functionality. For instance, potassium can diffuse through potassium channels at nearly the bulk diffusion rate (i.e. the channel hardly impedes their motion), while sodium is completely blocked, an amazing feat considering the ions are nearly identical, save a minute difference in their hydration radii. Beyond maintaining homeostasis, ion channels are also responsible for propagating electric signals along axons, crucial for signaling in multicellular organisms.

One of the holy grails in nanopores is being able to reproduce the functionality of these biological pores, that were created by millions or billions of years of evolution, in synthetic systems. The ability to do so could create a revolution in ion conducting systems, analagous to the revolution in electronics that was created by the invention of the solid-state transistor. However, the goal of ionics is not to replace wires, capacitors, and transistors with ion channels and pores; indeed, ions travel orders of magnitude slower than electrons, and therefore ionic systems are expected to act more slowly than electronic systems. Instead, integrated ionic circuits could be used for complex signaling since each ion carries its own information, and for controlling the transport of biomolecules. One needs only to look at biology for inspiration on the application of complex ion channels.

Chapter 2

Experimental study of ion conductance property of hybrid conductor-insulator nanopores

2.1 Background

In the introduction of this thesis we discussed the electrical double layer (EDL) which is a screening layer of ions that forms in the vicinity of a charged surface. The vast majority of pores studied are non-conductive insulators, and their surface charge properties primarily come from the functionalization of chemical groups at their surface. For instance, the base of the pore studied in this section is $Si3N_4$ (silicon nitride), whose native silane chemistry means there are exposed alcohols at the surface that are either negative or neutral depending on pH. However, charge on a surface can arise *via* other means. When a metal is exposed to an electric field, electrons in the metal rapidly redistribute themselves on the surface to cancel the external applied field. If we assume the metal was originally overall neutral, the charge pattern will consist of an abundance of negatively-charged electrons at one end and an abundance of positively-charged holes at the other. A natural question is whether these *induced* charges have associated EDLs in the same way that static charges do.

Previous studies suggest they do. For instance, Squires *et al.* and Pascall *et al.* performed experiments with applied external electric fields on various metal surfaces and discovered that electroosmotic flow occurred. They reasoned that the induced electroosmosis was a result of polarization of charges according to the model discussed above [46, 35]. However, these types of induced-charges have been seldom discussed in the context of nanopore transport, especially in the context of a realizable experimental platform. In order to understand the effect of induced charges on nanopore transport, we considered a hybrid metal-insulator pore created by evaporating a thin layer of gold onto the pore surface. If the pore was made only of one uniform material, its IV curve would be symmetrical due to the lack of any symmetry breaking in the system. The addition of the metallic layer breaks this symmetry, and we expect the current-voltage characteristic to also be asymmetric, a phenomenon known as current rectification. However, ionic current rectification alone is insufficient for proving that induced surface charges contribute to the pore's conductance; this is because essentially most types of symmetry breaking in a pore, including a difference in static surface charges between two regions, a difference in geometrical shape between two regions, *or* induced surface charges, will lead to ionic current rectification [55].

In order to provide evidence that induced charges directly contribute to a pore's conductance properties in this system, we need to devise a model for the manner of the induced rectification properties and to check if the model accurately describes experimental data. Figure 2.1 is a scheme of our proposed induced-charge model. To predict the conductance of the pore under this model, it is sufficient to examine the polarization that develops in the EDL in the various regions of the channel. First, the insulating part of the pore has an approximately uniform surface charge due to ionization of the chemical groups on its surface.

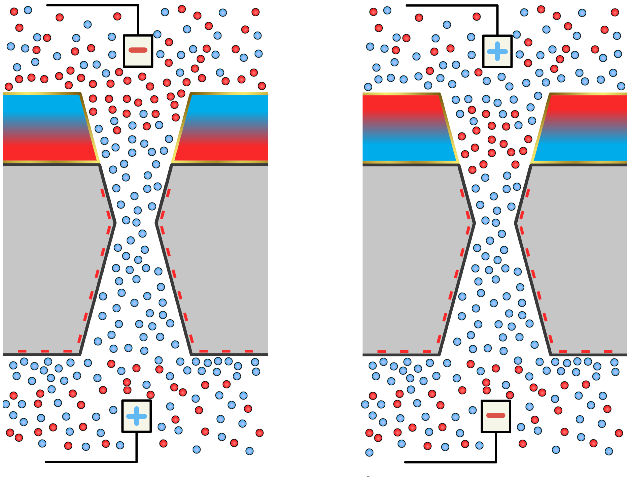

Figure 2.1: **Model for the induced-charge and EDL charges in the hybrid conductor-insulator nanopore. Left:** Negative bias applied to gold side. **Right:** Positive bias applied to gold side. For the positive bias, a depletion zone forms at the junction between the gold and SiN, which is expected to severely limit the conductance. For the negative bias, no depletion zone forms and therefore the conductance is expected to be unhindered. The double conical geometry reflects the expected geometry of SiN pores drilled *via* a transmission electron microscope (TEM) electron beam.

On the gold (conductor), the charge patterning depends on the applied voltage. When a negative bias is applied on the gold side of the pore, electrons are repelled from the electrode while holes are attracted. Keeping in mind that the charge in the electrical double layer has the opposite polarity as the surface charges, the charge pattern in the solution from the gold to the insulator is then $-++$ (left hand side of Fig. 2.1). Oppositely, when a positive bias is applied on the gold-side of the pore, holes flee to the inside of the pore while electrons are drawn towards the electrode. Therefore, from the positive electrode to the negative electrode the EDL charge pattern is $+-+$ (right hand side of Fig. 2.1). The primary difference in the charge pattern as it relates to the influence on the nanopore between the two voltage polarity cases is the charge juntion at the conductor-insulator interface; in the latter case (positive voltage applied on the metallic side), the $+-$ junction indicates the presence of a bipolar junction that leads to a depletion zone in the EDL, as discussed in the section on ionic current rectification in chapter 1. This depletion zone is characterized by having a very large resistance, and therefore limits the total current through the pore. For the opposite polarity, the depletion zone is not present and therefore we do not expect any significant limiting of the current. This model, which we call the induced-charge model for hybrid conductor-insulator nanopores, was tested experimentally in this work.

2.2 Experimental setup

In order to test the induced-charge model, we devised a platform consisting of thin nanopores in silicon nitride (SiN) with gold (Au) deposited on top. The crucial elements of this setup consisted of the silicon nitride (SiN) membrane, evaporated gold (Au) layer, transmission electron microscope (TEM) drilling of the pore, and the current-voltage characterization measurements.

2.2.1 Silicon nitride

Silicon nitride was used as the substrate through which to drill the nanopore. The effects of polarization of the gold should be apparent in truly nano-scale systems, so it was important to choose a material through which a small pore could be fabricated. As of the writing of this thesis, silicon nitride (chemical formula Si_3N_4) is a popular choice for creating small nanopores given its mechanical stability and well-understood silane surface chemistry[48]. The method of pore formation, TEM drilling (discussed below) can enable the creation of pores ranging from $1-20$ nm in diameter, and is capable of drilling through substrate lengths of at least up to 100 nm[24, 48, 21]. It is predicted that pores with very low aspect ratios, i.e. short pores, will have severely diminished rectification propeties[37]. In order to ensure large rectification, the solution must be subjected to a sufficient length of EDL. In order to strike a compromise between TEM's capabilities and the undesirable low-aspect ratio effects, a substrate thickness of 50 nm was chosen. The silicon nitride substrate is commonly used in TEM microscopy, and therefore is available from commercial vendors. The substates were ordered from the SPI company. The substrate itself is grown onto a thicker layer of silicon, through which a window is drilled on the backside to expose the silicon nitride. The final result is a 50 nm thick membrane of SiN supported by a silicon chip. After pore fabrication, silanol groups native to the pore surface are ionized when immersed in solution of the right pH value[45].

2.2.2 Gold deposition procedure

Although the model of induced-charge rectification described above is independent of the type of conductor used, we chose to use gold (Au) because of its mechanical stability after deposition and its resistance to corrosion and oxidation, which create a surface chemistry effect that could potentially obscure the relationship with the induced surface charges. With the conductor's material chosen, we think about the desired deposition thickness. In the model of induced-charge rectification described above, it is necessary to have a bipolar junction far enough inside the pore that a depletion layer can form. For this reason, we aimed to deposit a 30 nm layer of gold onto the surface of the SiN. There are a number of means of depositing metals onto surfaces, but given the thinness of the desired layer we chose to deposit *via* an e-beam evaporation process. In this process, the metal to be evaporated is inserted into a crucible contained in a vacuum chamber, and the sample is placed on a flat stage above the crucible, facing downwards towards the metal. The chamber is then sealed and pumped down to low pressures. Next, a beam of highly energetic electrons is fired at the material, which heats up under the kinetic barrage. The atoms then hit the surface of the substrate and stick. Although Au *can* be deposited directly onto the surface of SiN, a thin layer (3 nm) of chromium (Cr) was first evaporated, which facilitates adhesion of the Au.

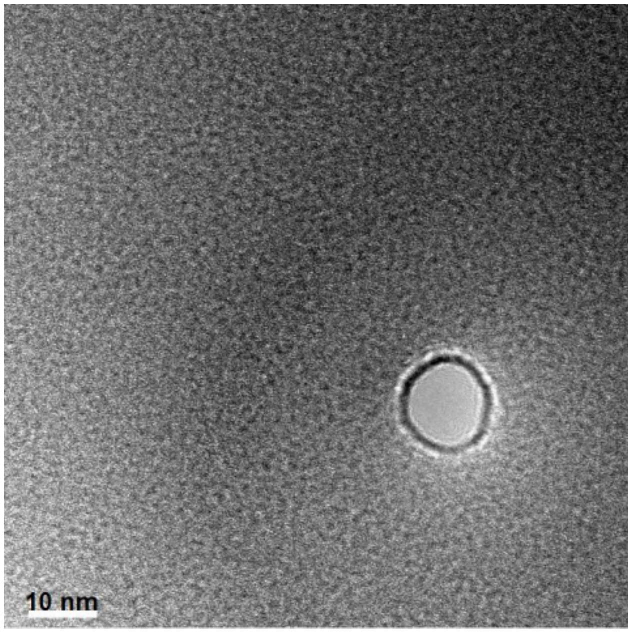

Figure 2.2: **A** $\sim 15\,\mathrm{nm}$ **SiN pore drilled *via* TEM.**

2.2.3 Transmission electron microscope drilling

The transmission electron microscope (TEM) is a super resolution imaging technique that is typically used to image objects below the optical diffraction limit of 200 nm. However, if the electron beam is sufficiently energized and focused, the electron beam can act as a drill for forming nanopores instead of for imaging[48]. This technique was used to drill pores through the SiN-Au hybrid device described in the above two steps. A highly focused beam in the TEM's scanning (S) mode is applied to the surface. The energetic electrons strike the surface and eject atoms, while simultaneously the entire structure melts. The final result is a pore with the same thickness as the substrate, and with a double conical geometry which is a result of the simultaneous ballistic ejection and melting[24]. Because the drilling is performed inside the TEM, the resulting pore can also be immediately imaged. Figure 2.2 shows an example of a $\sim 15\,\mathrm{nm}$ in diameter pore after TEM drilling.

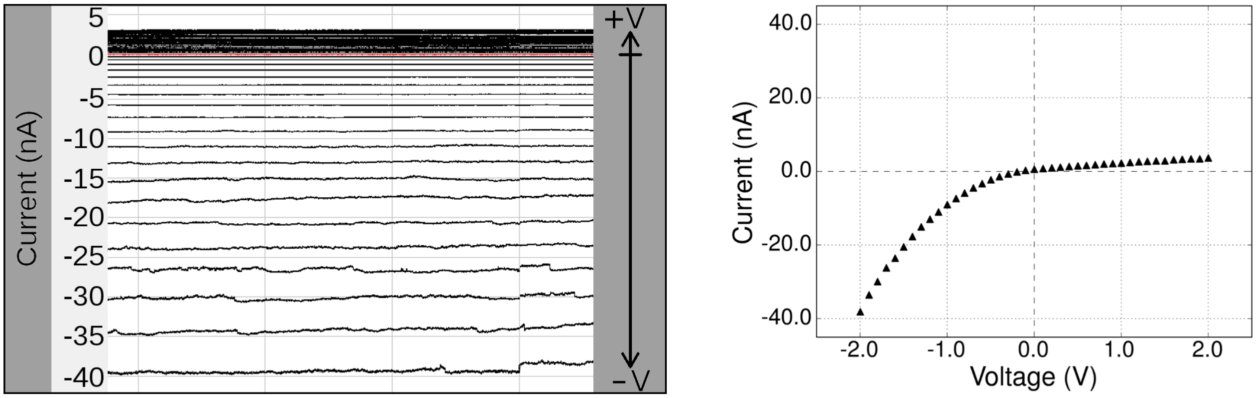

Figure 2.3: **A current-voltage time series alongside the current-voltage curve produced from it. Left**: Current-voltage time series. Each continuous line corresponds to one voltage setting; once a voltage value is set, the current does not significantly vary. **Right**: Traditional pore I-V curve. The asymmetry in the current with respect to voltage (present in both signals) is the hallmark indicator of ionic current rectification.

2.2.4 Pore conductance characterization

In order to test the induced-charge model, we measured the current-voltage (IV) response of each of the fabricated nanopores in 100 and 500 mM KF and KCl salt solutions. The total surface charge of a pore ‘felt’ by the ions in the solution is given by a combination of the ionized chemical groups on its surface and any chemical species that are adsorbed to the surface. Cl is known to adsorb to the surface of gold, and so we expect that the gold in KCl solutions will have net charge given by the adsorbed chloride ions and the induced-charges[33, 39]. For this reason, measurements were performed primarily with KF solution. However, it was predicted that adsorption of chloride on the Au surface would diminish the effects of the induced-charge, and this model was tested by performing measurements with KCl on chips that had already been measured in KF, to see if their conductance behavior changed according to this prescription.

Due to the small sizes of the pore and the low surface charge density of the silanols on the SiN surface, the interior of the pore is difficult to wet, meaning any vapor present inside the pore can be stable and difficult to remove[42]. If this is the case, ions cannot pass through.

Often times these vapor phases are quasi-stable and the pore will spontaneously undergo wetting-dewetting transitions. In order to reduce these hydrophobic effects, we use an even 50/50 mixture of water and ethanol solvent; the combination of both solvents promotes wetting of the pore.

In principle, during IV measurements one needs only to sweep the voltage along the desired range, stopping to record the current at each voltage value. Usually a pause time of $\sim 1\,\text{second}$ is applied after changing the voltage to allow for the system to equilibrate, e.g. due to system capacitance charging/discharging. However, in systems in which the system conductance can stochastically change, e.g. due to the spontaneous wetting/dewetting transitions discussed above, it is advantageous to record a time series of the current voltage sweeps rather than measure single data points. If a transition occurs, it can be observed in the time series of the signal and appropriately dealt with afterwards. Single data points offer little interpretability; if the IV curve shows ionic current rectification, is the rectification caused by behavior in the electrical double layer, or did the pore spontaneously dewet and inhibit the flow of ions? By measuring the time-series of current rather than measuring single data points, we are more certain that the IV curves generated reflect the true state of the fully wetted pore. The protocol for measuring IV curves is then to apply a fixed voltage, record the current for a fixed amount of time, and repeat for all of the desired voltages. Then, an IV curve is produced by averaging the current time-series for a fixed interval of time (averaging is performed to smooth over the small amount of noise in the signal). In this study, voltages were applied for a total of $20\,\text{s}$ and the current values in the last $0.5\,\text{s}$ were averaged to create the current measurement value. Figure 2.3 shows an example current-voltage time series and the IV curve produced from it for one of the pores used in the study measured in KF solution. On the left is a current-voltage time series plot that shows the current value time series for different voltage settings, while the right hand side of the figure shows a traditional I-V curve of the pore.

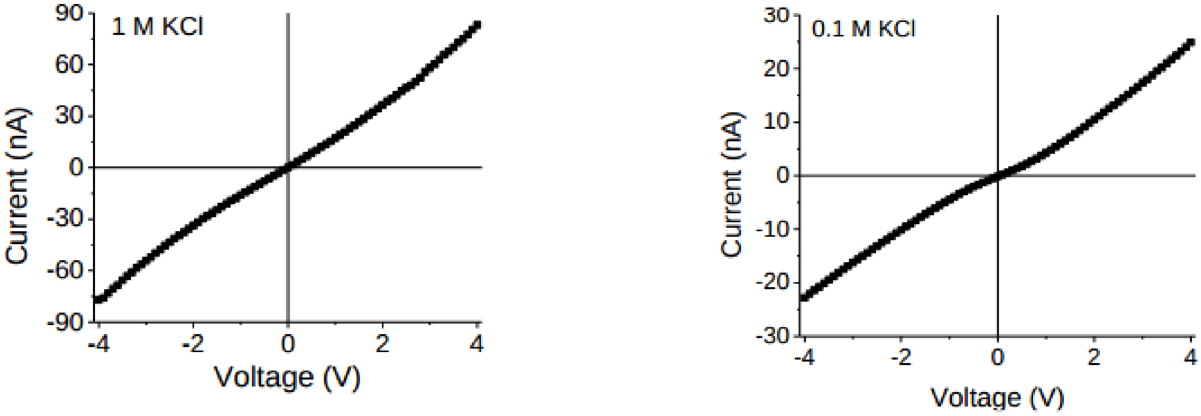

Figure 2.4: **IV curves taken of bare SiN pores**. The symmetry in the IV curve reveals no inherent rectification of the TEM drilled pores.

2.3 Experimental results

A number of conductor-insulator pores were tested, along with plain SiN pores to test if the pores intrinsically rectify the current (e.g. due to a geometrical asymmetry).

Figure 2.4 shows two IV curves gathered for the SiN-only (insulator pore only). The plot shows approximately symmetric IV curves, indicating a symmetric nanopore.

On the other hand, figure 2.5 shows two IV curves collected for a single nanopore approximately 9 nm in diameter. The IV curves taken in KF show significant rectification, with a ratio of approximately $R = 0.5$ for the 100 mM concentration and $R = 0.7$ for the 500 mM KF concentration. The increase in rectification R towards $R = 1$ with increasing salt concentration is consistent with the decrease in thickness of the EDL [40, 25]. In the model we developed for the induced-charge rectification, a depletion region is expected to form in the interior of the pore. Typically pores that have depletion zones experience much greater rectifications due to the 'off-state' voltage polarity having nearly zero conductance[55]. While this pore's rectification is not small enough (e.g. not close to zero) to describe it as an ionic diode, the rectification direction is nevertheless consistent with the proposed model. We

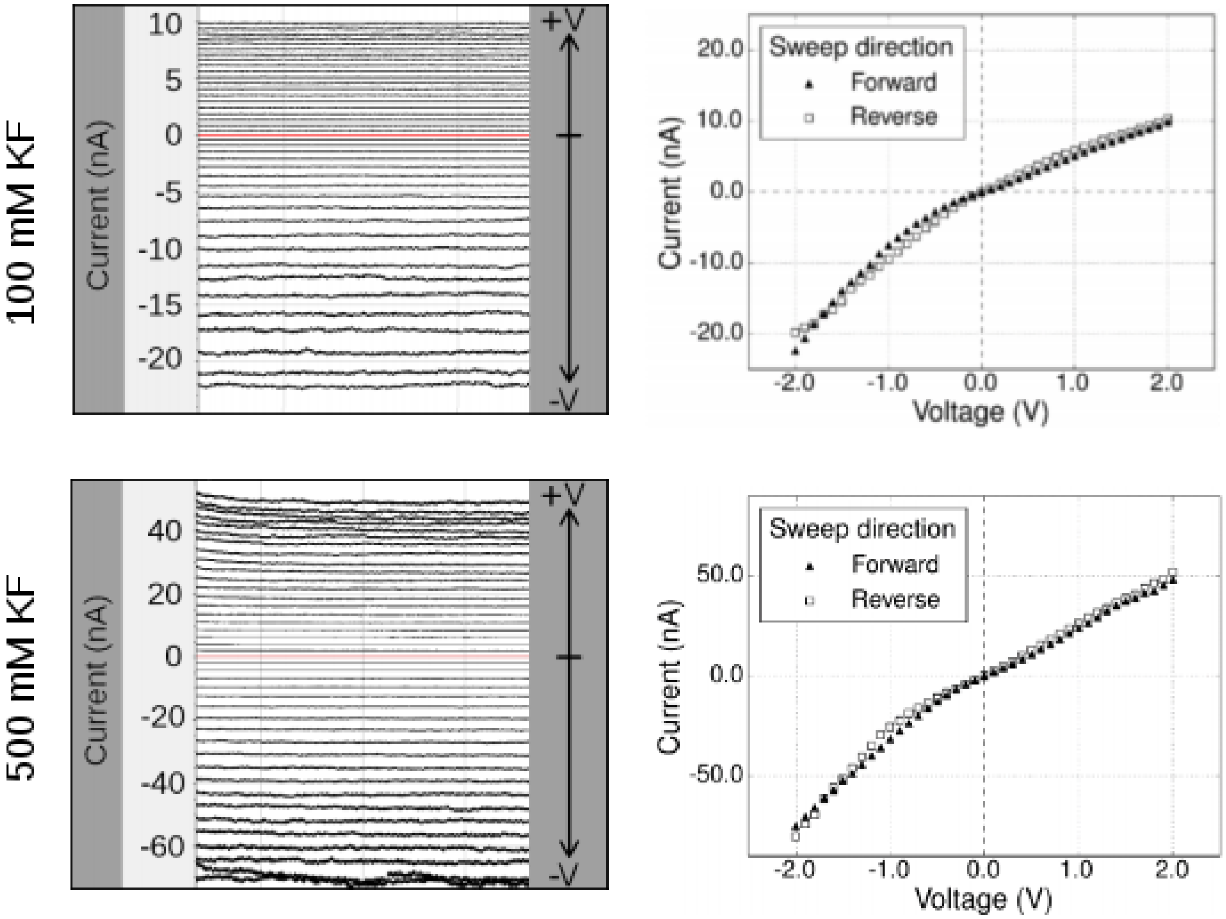

Figure 2.5: **IV curves taken of Au-SiN pore in** 100 mM **and** 500 mM **KF.** The symmetry in the IV curve reveals no inherent rectification of the TEM drilled pores. The ion rectification ratio R is lower in the higher concentration solution, as is expected from basic considerations of EDL thickness.

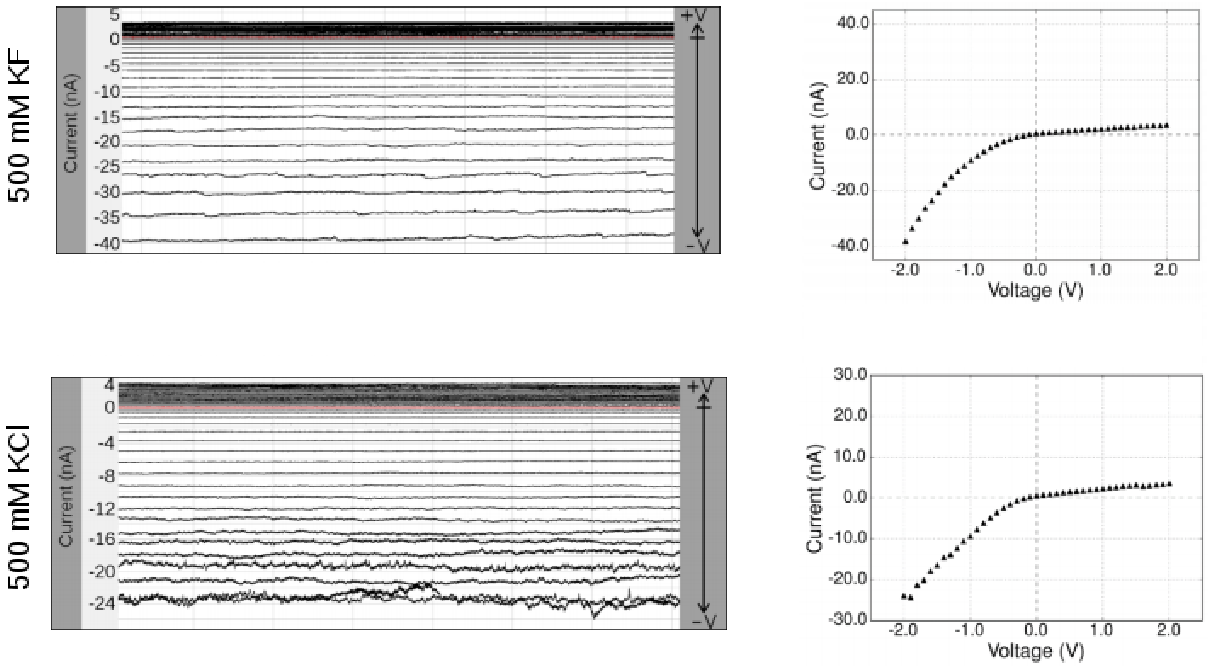

Figure 2.6: **IV curves taken of Au-SiN pore in** 500 mM **KCl and KF.** The rectification ratio R is lower in the KCl solution than in the KF solution, which is expected due to the additional contribution of the static charge from adsorbed Cl^- ions on the gold surface.

note that this direction of rectification is inconsistent with models having only static charges on the SiN and Au, barring the case where the Au has positive charges adsorbed onto its surface, which is unexpected for the ion species used in this study.

In order to understand the effect of a static charge superimposed on top of the induced-charge, we next performed experiments in KCl in addition to KF. Figure 2.6 shows a 12 nm pore with IV curves measured in 500 mM concentration of both types of salts. Note that both salts give the same type of rectification as in the previous example. This result is not entirely unexpected, as the presence of adsorbed chloride will bring the two charges in the depletion zone closer together in magnitude, while still maintaining a finite, albeit reduced rectification. If the Cl^- ions adsorbed to the surface of the gold to the extent that they dominated both the induced-charge on the gold and the surface charge on the SiN, then it is possible the rectification direction could even flip direction such that $R > 1$. However, we did not observe such an effect.

2.4 Modelling results

In order to provide an additional line of evidence pointing to induced-charge based ion current rectification found in experiments, we performed finite-element analysis simulations using the COMSOL Multiphysics software package. The models were designed to emulate the experimental set up, e.g. the channel geometries and salt concentrations used were similar. However, rather than try to reproduce the double conical geometry expected for TEM drilled pores, we worked with a cylindrical geometry which greatly facilitated convergence of the solutions with the very minor penalty of not adhering exactly to the experimental conditions. Because the cone angle is expected to be shallow[24] and because the COMSOL results are meant to be interpreted semi-quantitatively, and are primarily used to draw conclusions about the rectification direction and mechanism, replicating the exact geometry of the pore was deemed unneccessary.

The results of the simulations are found in figures 2.8 and 2.9. We simulated IV curves for the model device and calculated the average concentrations of the cations, anions, and combinations at various axial positions inside the pore, and used these calculations to calculate the width of the depletion zone that forms for positive voltages. Figure 2.8 shows IV curves of the simulated pore at various concentrations. Notice that at low concentrations the pore rectifies in the negative direction i.e. $R = |I_{-}/I_{+}| > 1$ and the rectification ratio R decreases with increasing electrolyte concentration, both results are consistent with the experimental data. Figure 2.9 shows the average concentrations of C_K, C_{Cl}, $C_K + C_Cl$ and $C_K - C_Cl$ at various axial positions. The concentrations of C_K and C_{Cl} along the length of the gold surface are consistent with the polarization model of gold: when a positive potential is applied on the side of the metal, electrons are drawn to the entrance of the pore, inducing formation of an EDL more positive than at the opposite terminal, and the opposite occurs for the opposite voltage. Along the length of the SiN far from the junction, the concentration of potassium is enhanced due to the negative charge of the surface, and chloride is reduced.

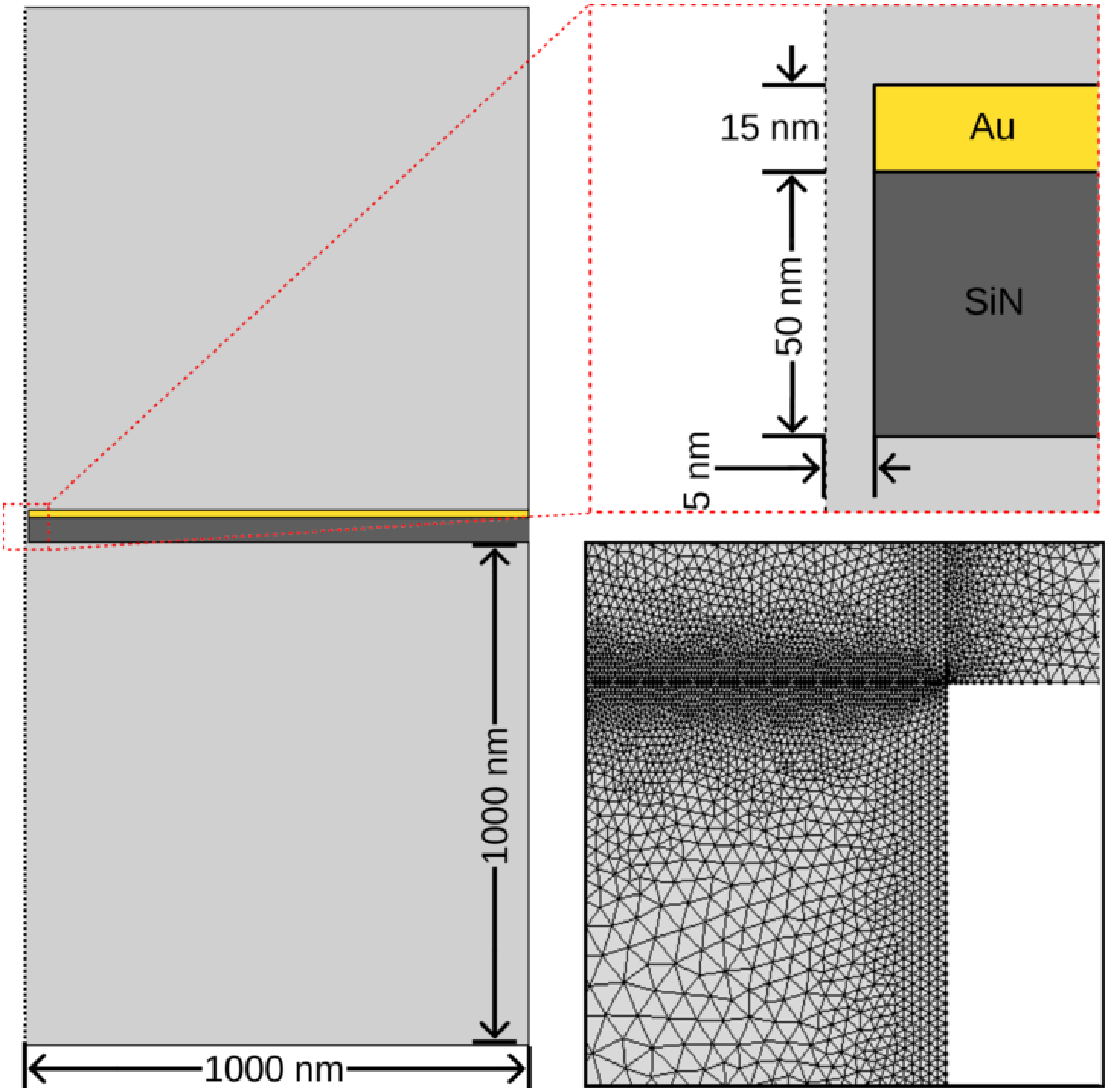

Figure 2.7: **Simulated SiN-Au hybrid pore geometry.** The two large gray squares are the reservoirs. The right inset shows the geometry of the simulated pore. The bottom right portion of hte fiture shows the mesh density used in the simulation.

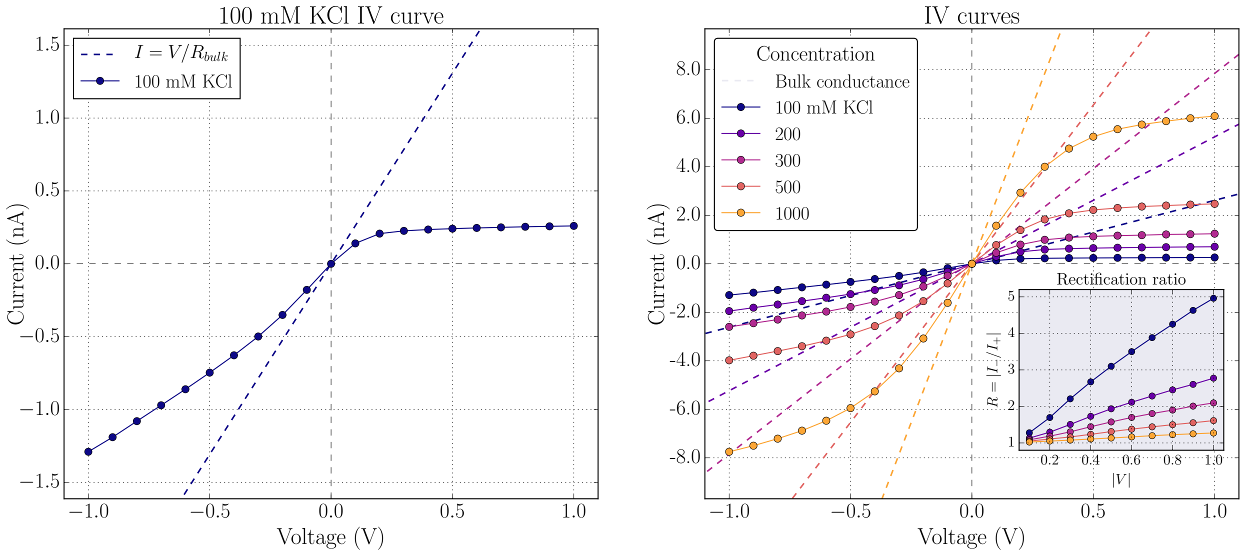

Figure 2.8: **IV Curve results for multiple KCl concentrations. Left:** 100 mM KCl simulated IV curve, along with a dashed line indicating the bulk resistance of the pore. **Right:** Multiple simulated IV curves. **Inset:** Rectification ratio.

In the plot of $C_K + C_{Cl}$ which reflects the total ion concentration (bottom center), at positive voltages there is a drop in the concentration in the vicinity of the junction. In this region the total concentration is far below its bulk value, while elsewhere it is much closer to the bulk. This severely reduced charge density reflects the formation of the depletion zone, the zone created when ions near the diode junction are pulled apart under the applied bias. The resistivity $\rho \propto (C_K + C_{Cl})^{-1}$, so the depletion zone has a very large resistance and therefore limits the current through the pore as a whole. Depletion zone regions like the one that appears in the simulation severely limit current, which can be seen in the near-zero slope of the current for positive voltages in the IV curve. The current is limited by the depletion zone, and we identify this type of pore as a diode. The bottom-left plot of figure 2.9 shows the width of the depletion zone as a function of voltage. The depletion zone was defined as the width along the pore axis such that the total ion concentration is below half of the total ion concentration (in this case, below 100 mM, since $C_K = 100\,\text{mM}$ and $C_{Cl} = 100\,\text{mM}$. While increasing the voltage increases the current, the depletion zone is also widened with increasing voltage, resulting in a net sub-linear relationship between voltage and current at

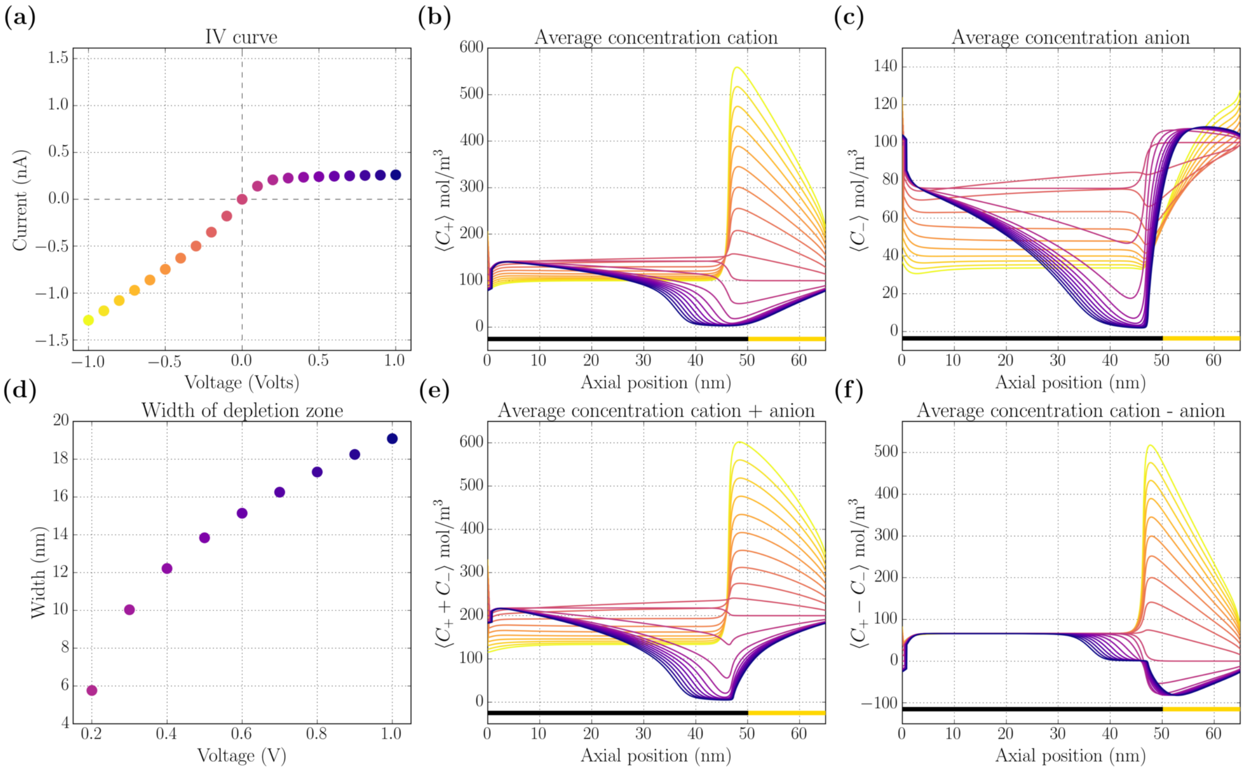

Figure 2.9: **Results of COMSOL simulation showing the expected ion distributions inside the pore.** **a**: Simulated IV curve for 100 mM KCl. **b:** Average concentration K at various axial positions, with the colors representing the same voltage values as in **a**. **c:** Same as **b**, but for chloride ions. **d**: Width of the depletion zone, as determined by the width of the region in **e** where the total ion concentration is less than half its bulk value. **e**: Sum of potassium and chloride concentrations. **f**: Difference of potassium and chloride concentrations, which is proportional to the net charge.

positive voltages.

The COMSOL results show that the model of induced-charge based electrical double layers is possible, and that the magnitude of the effect is enough to greatly influence the pore. Furthermore, the results show that the model system results in rectification ratio $R > 1$, in the same direction of the experiments' IV curves.

2.5 Conclusion & Future Work

The work presented in this chapter demonstrates the capabilities of conducting layers in affecting the ionic conductance properties of nanopore systems. We developed a model for the system, in which a dynamically induced charge acts in concert with the static ionized silanol groups native to the SiN surface to create a diode-like rectification behavior. This type of rectification and its direction cannot be explained with static charges alone, and therefore we conclude that the induced charges on the gold layer were significant in contributing towards the total rectification of the device. Furthermore, numerical simulations using COMSOL multiphysics provided another line of evidence that the induced-charges contributed to the device's conductance. In the simulations, for the 'off-state' of the device at positive voltages there was a clear depletion zone in the channel, in agreement with our a priori expectations based on the physics of the device.

The ability to fabricate single nanopores with novel ion conductance properties is crucial in fabricating integrated ionic circuit devices. These non-trivial conductance properties are usually achieved *via* chemical modification or *via* or modification with biomolecules such as DNA. However, this work has revealed another potential way of creating diode-like nanopores with the addition of permanent embedded metallic layers.

Chapter 3

Resistive pulse studies of aspherical mesoparticles

3.1 Background & Theory

In the introduction of this dissertation we introduced and explained the theory behind resistive pulse sensing, a particle characterization technique that works by monitoring the change in conductance of a nanopore as small particles pass through it. Probably the most important application of RP sensing is in measuring the sizes of particles. An analytic model was devised by DeBlois *et al.* to relate the size of a particle to its resistive pulse amplitude [7, 8]. The solution is essentially an electrostatics boundary-value problem: given an insulating particle inside a pore and a known externally applied voltage, calculate the electric field distribution inside the pore, and from the electric field distribution calculate the pore's expected resistance with the particle inside it. When this calculation is performed for spherical particles travelling along the axis of long cylindrical pores, the change in resistance or

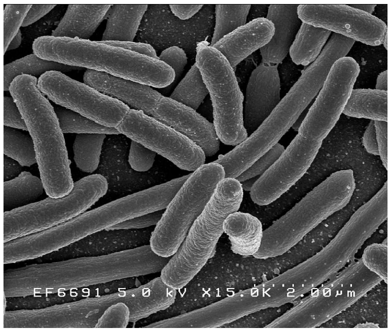

(a) Escherichia coli (E. coli) bacteria.

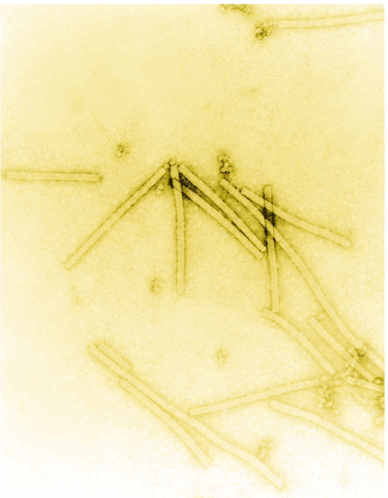

(b) Tobacco mosaic virus

Figure 3.1: **Two examples of natural aspherical biological entities.**

current is found to be

$$\frac{\Delta R}{R_0} = \frac{\Delta I}{I_p} = \frac{3}{2}\left[1 - 0.8\left(\frac{d}{D}\right)^3\right]\frac{v}{V}. \tag{3.1}$$

Equation 3.1 is useful for relating the change in current—or resistance—to the diameter of spherical particles. The factor of $\frac{v}{V}$ is no accident—it reflects that the primary reason for the change in resistance of the channel is from the loss of conductive volume in the pore due to the presence of the insulating particle[7].

While this equation is useful, it is very often the case that particles of interest are not spher-

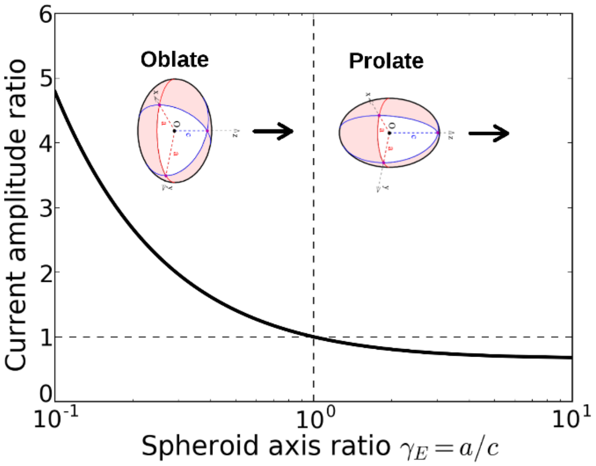

Figure 3.2: **Resistive pulse amplitude $\Delta I/I_p$ relative to that of a sphere.** Inset images show the geometry of the ellipsoid. The central axis is for spheres, particles with equal axis lengths. To the right of the central line the geometry is described as prolate with respect to the direction of motion, and to the left it is oblate. The equation 3.2 predicts that the current amplitude decreases for prolate geometries, and sharply increases for oblate geometries.

ical. For instance, many biomolecules such as viruses and proteins are poorly approximated as spheres, and are more rod-like in shape (see Fig. 3.1). In this case, the resistive pulse amplitude of on-axis translocations through a cylindrical pore is given by

$$\frac{\Delta R}{R_0} = \left[f_\perp + \left(f_\parallel - f_\perp \cos^2\alpha\right)\right]\frac{v}{V}, \tag{3.2}$$

where $f_\perp$ and $f_\parallel$ are so called ‘shape-factors’, that depend on the particle’s major and minor axis lengths, and α is the orientation of the particle with $\alpha = 0$ being axially aligned[15]. Notice that again the factor of v/V shows up as it did in the Eq. 3.1. Figure 3.2 shows a plot of the relative $\Delta I/I_p$ for various ellipsoids of the same volume but different axial lengths.

While equation 3.2 is useful for determining the volume of spheroidal particles from their resistive pulse amplitudes, it would be useful to devise a method for measuring the length of particles in addition to measuring their volumes as an additional physical marker for their identification in a sample. However, it is not immediately obvious how this could be achieved. In the following sections, we suggest a measurement protocol that can be used to determine the length of particles, first in a qualitative manner that can be used to rank particles of different lengths, and then in a quantitative manner to actually measure the length of unknown particles.

3.1.1 Length measurement protocol

Consider a pore with a rough, non-uniform interior. Due to the irregular interior, the channel cross sections will have a range of resistance values; for instance, a large cavity in the channel will have a smaller resistance than a more narrow constriction. Therefore, we can consider the resistive pulse signals of particles passing through the pore to reflect the pore's interior shape. If we ignore the effects of electrostatic boundary conditions on the resistive pulse amplitude, the following yields the resistive pulse amplitude for non-constant width pores:

$$\Delta R\left(z'\right) = \frac{\rho}{\pi}\left[\int_{z=z'}^{z=z'+l_p}\left(\frac{1}{r_P^2\left(z\right)-s_p^2\left(z\right)}-\frac{1}{r_P^2\left(z\right)}\right)dz\right]. \tag{3.3}$$

As a concrete example of when this occurs, Pevarnik *et al.* performed experiments with small polystyrene beads in polyethylene terephthalate pores, and found the resistive pulse were characterized by irregular, jagged shapes. They reasoned that this non-traditional resistive pulse profile must be due to the shape of the pore itself, and confirmed the hypothesis by imaging the interiors of the pores using a reverse metal replica procedure[36]. This concept is demonstrated in Fig. 3.3.

So far we have made mention of the *local* pore radius. From Eq. 3.3, we can see that

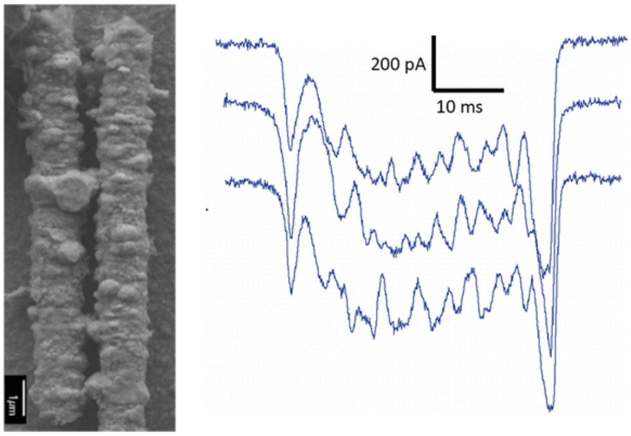

Figure 3.3: **Metal replica of PET pores (left) and samples of resistive pulse amplitudes of polystyrene beads collected through pores of the same material (right).** The resistive pulse amplitudes is a measure of local pore resistance, and is reflective of the local pore's diameter. Copyright: Figure adapted from Innes *et al.* Velocity Profiles in Pores with Undulating Opening Diameter and Their Importance for Resistive-Pulse Experiments. *Analytical Chemistry*, 86 (20), 10445-10453, 2014. DOI: 10.1021/ac502997h.

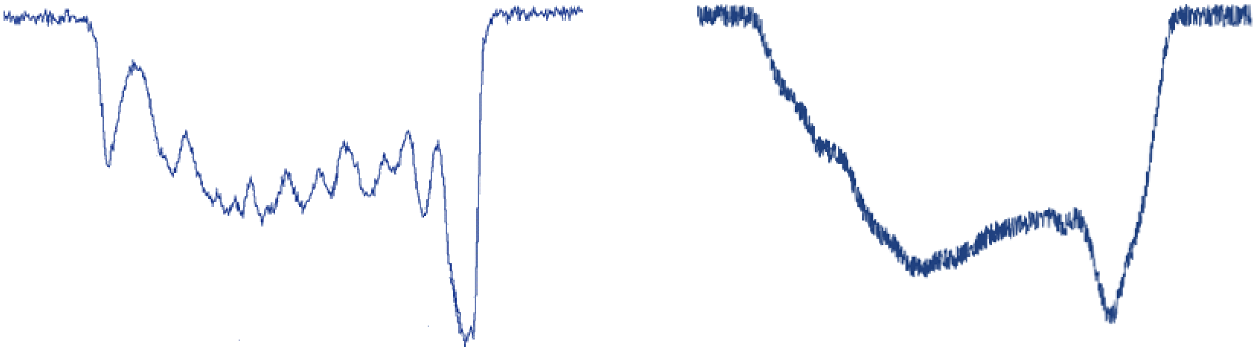

Figure 3.4: **Signal of a small sphere (left) and simulated signal of a longer particle (right) through a PET pore.** While the short particle reveals the pore's small scale interior features, the longer particle is not capable of resolving these features.

the change in resistance is only due to the area of solution surrounding the particle, and does not depend on the resistance of the pore elsewhere. According to this equation, not only do pores measure the interior geometry of the pore, but they measure it with a *length dependent* resolution. For particles that are shorter than the characteristic length scale fo the undulations in the channel, the resistive pulses are high resolution mappings of the inner pore geometry. These small particles are able to explore minor cavities and protrusions in teh channel. On the other hand, if we consider a particle whose length extends along many of such irregularities, it may occupy several different regions of resistance at a time. In this case, the particle maps the pore's inner geometry with a low resolution. Figure 3.4 shows an example of a sphere passing through a PET pore alongside a simulation of the signal a longer particle would produce. The key difference between the two is in there resolution, as described above. While the small sphere is able to reveal the fine features of the pore's interior, the longer particle's signal averages over these features.

The above arguments reveal that the signals of short and long particles through irregular pores are fundamentally different, and this immediately suggests a means for qualitatively determining the length of a particle. First, we pass 'tracer particles', particles of known length through the pore and record their resistive pulse signals. Then, we record the passage of particles of unknown lengths. After both the tracers and unknown particles are recorded, we rank the unknown particles according to the amount of resolution present in their resistive pulse signature. Figure 3.5 shows a picture describing this qualitative algorithm for ranking particle lengths.

While this qualitative length ranking algorithm is useful, it would be desirable to devise a means for *quantitatively* determining the lengths of unknown particles. In order to under-

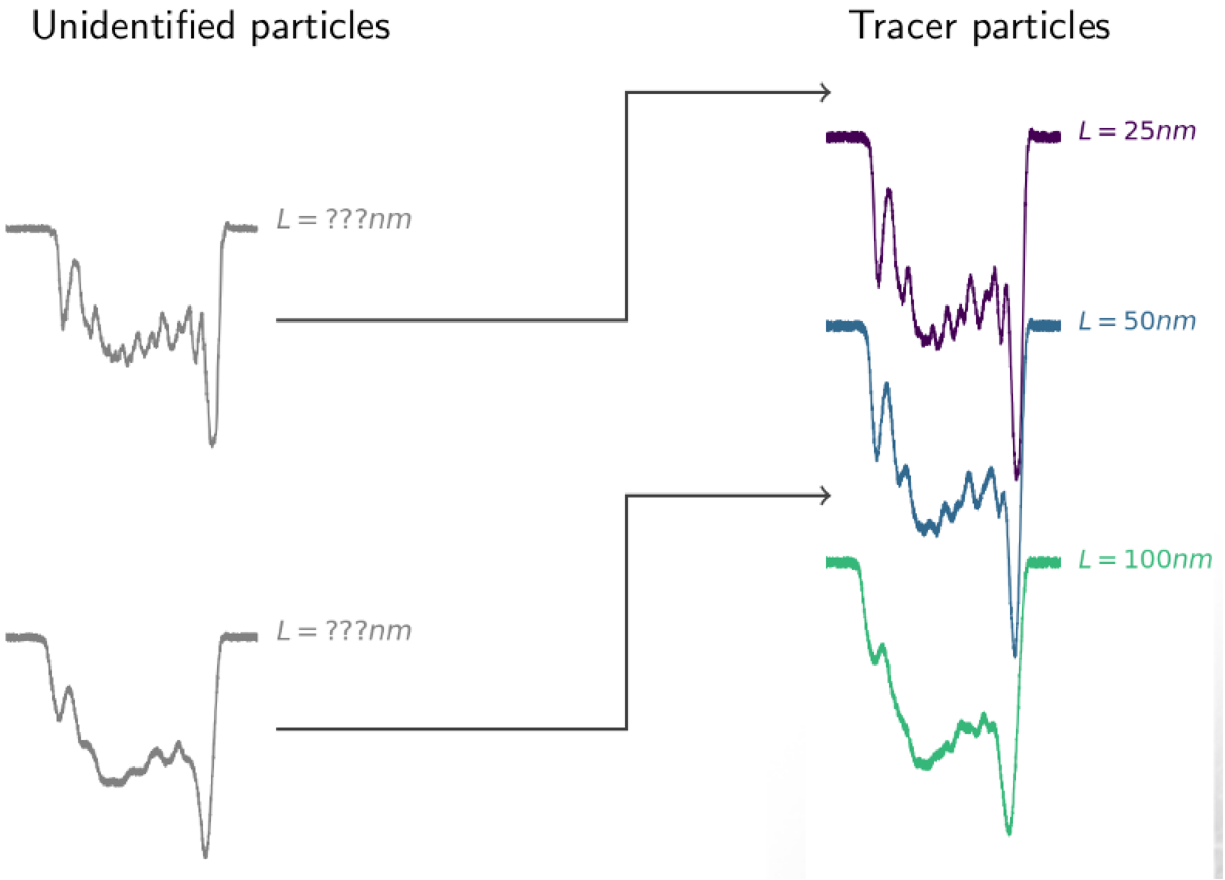

Figure 3.5: **Protocol for qualitatively determining particle length.** Resistive pulse signals of particles of unknown and known length are shown on the left and right, respectively. The particles of known length on the right are 'tracer particles', particles that are recorded so as to provide a means for comparing other particles' signals with. Each unknown particle is ranked according to the resolution its signal provides and compared with the tracer particles' signals. This method does not yield an accurate measure of length, but can be used to obtain a semi-quantitative estimate.

stand how this can be done, we rewrite Eq. 3.3 as follows:

$$\begin{aligned}
\frac{\Delta R_l}{R_0} &= \frac{\rho}{\pi}\left[\int_z^{z+l_p}\left(\frac{1}{r_P^2\left(z'\right)-s_p^2\left(z'\right)}-\frac{1}{r_P^2\left(z'\right)}\right)dz'\right]/R_0 \\
&= \sum_{i=0}^{n-1}\frac{\rho}{\pi}\left[\int_{z+il_s}^{z+(i+1)l_s}\left(\frac{1}{r_P^2\left(z'\right)-s_p^2\left(z'\right)}-\frac{1}{r_P^2\left(z'\right)}\right)dz'\right]/R_0 \\
&= \sum_{i=0}^{n-1}\Delta R_s\left(z+il_s\right)/R_0.
\end{aligned} \tag{3.4}$$

In this form of the equation, we break the integral for the change in resistance of a long particle into smaller parts of equal length. Because resistance add in series, each of these small parts of the integral corresponds to the resistance of a shorter particle, and therefore we recognize that the resistive pulse amplitude of a long particle can be reexpressed as the sum of the resistive pulse amplitudes of smaller particles at various points in the channel. This suggests a new means of *quantitatively* measuring particle length: we record resistive pulse amplitudes of smaller particles, and use the transformation given by Eq. 3.4 to *simulate* the resistive pulse signal of a particle of longer length. We generate many such simulations over a range of lengths, and then compare each of the simulated signals with the signal of the particle of unknown length. The comparison that yields the greatest similarity is declared as the true length of the unknown particle.

Instead of exactly using Eq. 3.4, we instead use a convolution or moving average of the signals of the shorter particles given by the following equation:

$$\begin{aligned}
I_i \rightarrow I_i^{l'} &= \frac{1}{N}\sum_{j=i-\frac{N}{2}}^{j=i+\frac{N}{2}} I_j, \\
N &= \frac{fl'}{v},
\end{aligned} \tag{3.5}$$

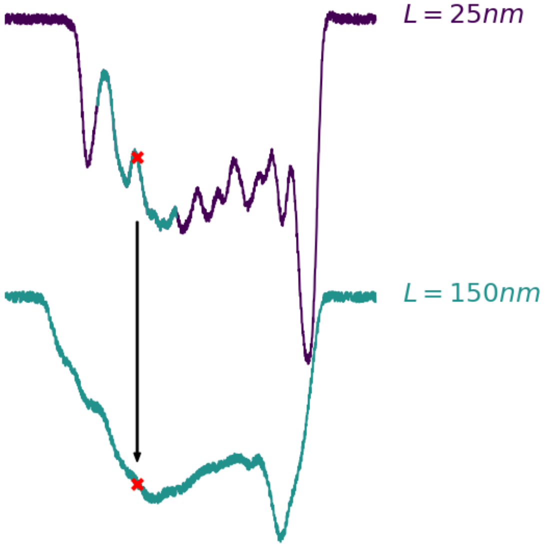

Figure 3.6: **Visualization of the moving average process.** The teal shading in the top resistive pulse indicates the length over which the moving average is performed. This point is mapped onto a point in the transformed signal below it, and this transformation is applied to all points in the original signal.

where N is the total number of points in the moving average, I_i is the ith current measurement in the signal of the unprocessed short particle, $I_i^{l'}$ is the transformed data point for a moving average over length l', f is the sampling frequency of the current acquisition instrument, and v is the *average* velocity of the particle during its translocation through the pore. However, equation 3.5 slightly oversamples particle positions in the middle of the moving average compared to particle positions at the very ends, along a distance equal to half the length of the small particle at each end. For this reason, the moving average estimate of the correct transformation should slightly overestimates the length of long particles. However, when $l \ll l'$, i.e. the tracer particle's displacement length is much less than the longer rod's displacement length, the effect is negligibly small. Figure 3.6 shows a visualization of the moving average process and its effect on the smoothed signal.

After computing the moving averages of the tracer particles over an array of lengths, a similarity measure is calculated between every pair of convoluted-raw signals for the tracer

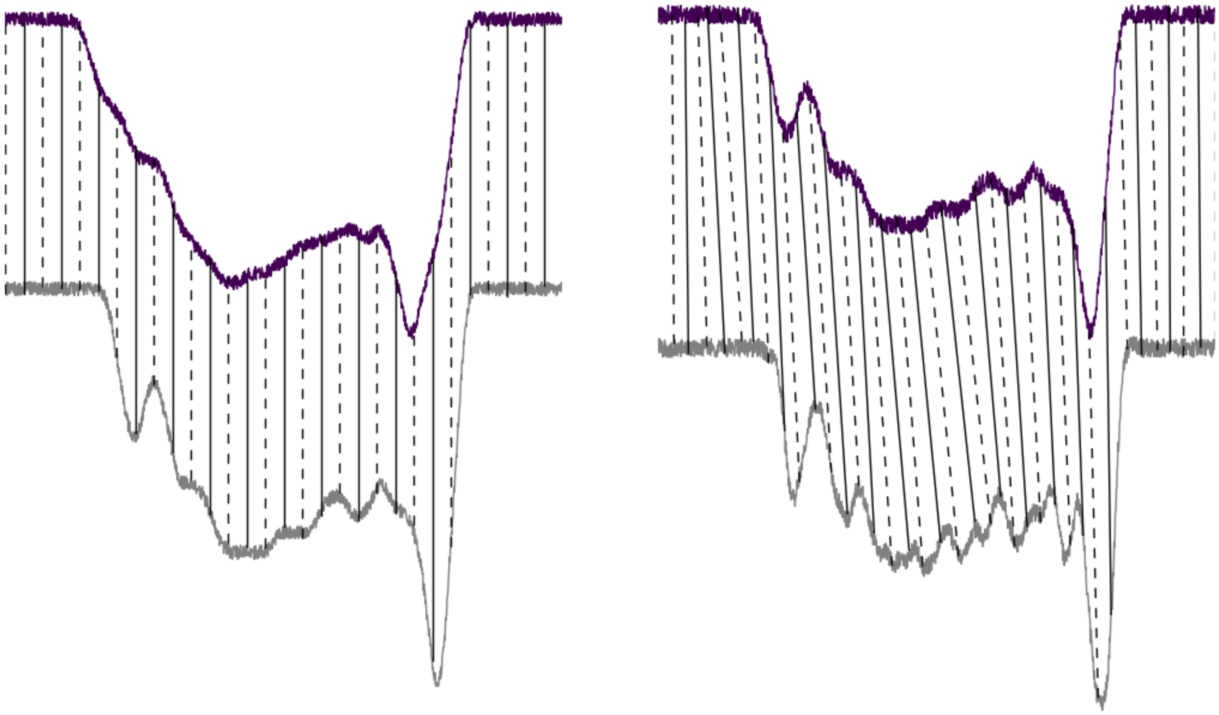

Figure 3.7: **Comparison of standard Euclidean distance metric (left) and distance metric as determined by dynamic time warping (right) with four random simulated resistive pulse events.** Notice that the Euclidean distance does not take into account small displacements of the two signals in time, despite their obvious similarity. On the other hand, dynamic time warping is able to account for small mismatches in time by finding the connections between points that minimizes the total cost.

particle and the long particle, and the length with the greatest similarity measure is chosen as the correct length of the particle.

Probably the simplest similarity measure of two time-series is the point-wise summed Euclidean distance between the two signals given by the following formula:

$$C\left(S, S'\right) = \Sigma_{i=0}^{N-1}\left(S_i - S'_i\right)^2 . \tag{3.6}$$

However, the problem with the similarity measure in Eq. 3.6 is it is not robust against small variations in the phases of the two signals, i.e. if the two signals evolve in time noisily in such a way that they are not instantaneously exactly in phase. For instance, Fig. 3.7(left) shows two resistive pulse time-series taken during an experiment and overlapped exactly in time, with lines connecting the points that would be summed in the Euclidean distance metric[23]. Notice that the two sequences are very similar, but due to a non-perfect alignment of identical features in time, the aligned Euclidean distance metric will greatly penalize the similarity of the two signals. It seems that we need a technique that is more robust against local time distortion in order to better measure the similarity of the two signals.

3.1.2 Dynamic time warping

One method of measuring the similarity of two time-series that accounts for time offsets is dynamic time warping[23]. Figure 3.7(right) shows two time-series signals that have been aligned after dynamic time warping. The image shows that the algorithm is capable of matching points that are not perfectly aligned in time, but that reflect the actual *physical* progression of the two signals. With regards to our case, local features in two RP signals that correspond to the same position in the channel may not vertically overlap perfectly in time, but the dynamic time warping algorithm is capable of recognizing that the two features are same.

The dynamic time warping algorithm works as follows. First, a matrix $D_{i,j}$ of the point-wise Euclidean distance between all two points in the two signals is created, as shown in Fig. 3.8 (left). For instance, point $D_{3,4}$ is the Euclidean distance between point 3 and 4 in signals S and S', respectively. The objective is to traverse through the distance matrix along the path that minimizes the total accumulated distance, or the cost C, subject to certain kinematic constraints. Each step in the trajectory is defined by the indices from the two respective signals (i, j). The non-warped Euclidean distance metric given by Eq. 3.6 would correspond to a straight diagonal trajectory through the matrix, e.g. no warping at all.

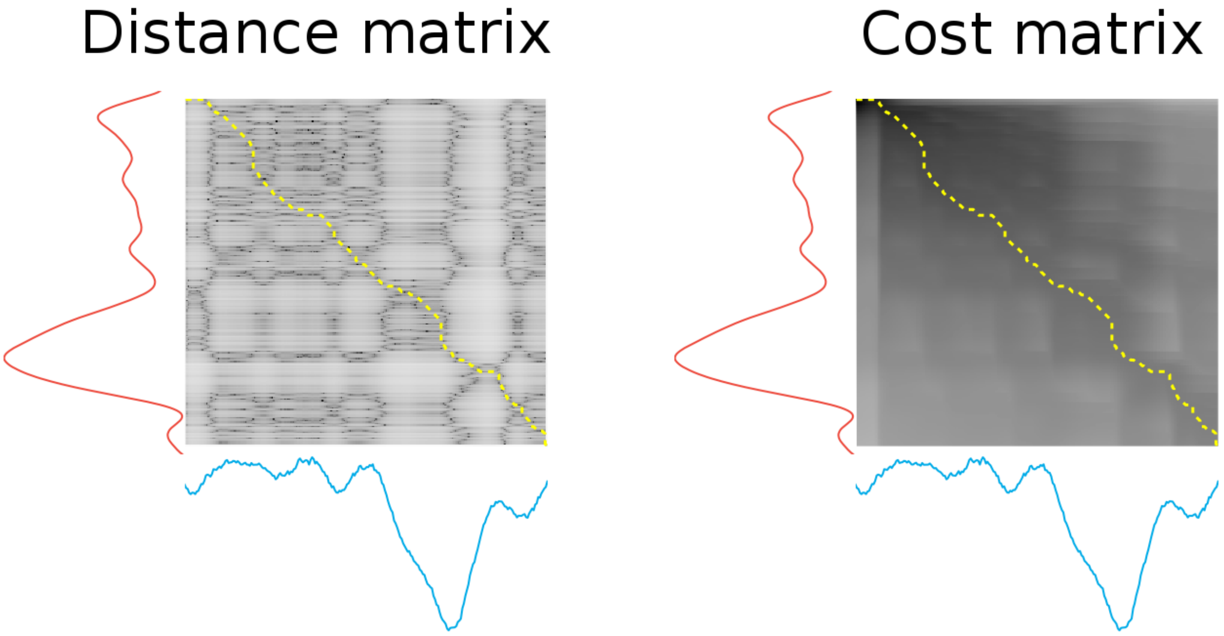

Figure 3.8: **Distance (left) and cost matrices (right) of two resistive pulse signals as determined by dynamic time warping.** The element (i, j) in the distance matrix represents the Euclidean distance between the two signals, $\left(S_i - S'_j\right)^2$. Every element in the cost matrix represents the summed Euclidean distance along the minimum path that arrives at that point. Therefore, the point at the lower right-most point in the distance matrix is the summed cost to completely connect the two signals. The path that yields the cost of that element in the matrix is represented by the yellow dashed line.

Although there are several formulations of dynamic time warping, the original method only allows for three types of motion such that $(i, j) \to (i+1, j)$ (progressive vertical motion), $(i, j) \to (i+1, j+1)$ (progressive diagonal motion), or $(i, j+1)$ (progressive horizontal motion). Regressive motion, which would correspond to taking a step backwards in the path back towards the upper left cell in the matrix, is forbidden. The key to dynamic time warping is the means by which we determine the optimal path that minimizes the total accumulated distance. The problem of finding the ideal path through the distance matrix according to the kinematic constraints is combinatorically large, and the number of unique trajectories has lower bound $\binom{N'+N-2}{N'-1}$, where N, N' are the number of data points in each of the two signals. Due to this scaling, random searching of paths through the matrix is not a feasible means of determining the optimum path for large $N + N'$.

As the name implies, dynamic time warping (DTW) is a dynamic computational algorithm for determining the minimum path, described as follows. First, we must recognize that, due to the kinematic rules for stepping through the matrix, the minimum path to arrive at point (i, j) must pass through one of points $(i-1, j)$, $(i-1, j-1)$, or $(i, j-1)$. Therefore, the cost C of point (i, j) is given by

$$C_{i,j} = D_{i,j} + \min\left[C_{i-1,j}, C_{i-1,j-1}, C_{i,j-1}\right]. \tag{3.7}$$

With this in mind, we can build up the complete cost matrix $C_{i,j}$, the cost to arrive at point i, j *via* the minimum path, by starting from the top-left corner $C_{0,0}$ and propagating through the matrix with Eq. 3.7. We repeat this process until we arrive at point $C_{N-1,N'-1}$, which is the minimum cost of a complete matching up of the two signals. At this point we have arrived at the answer we seeked in the beginning, the total distance metric between the two signals. However, it is often informative to calculate the actual trajectory that the

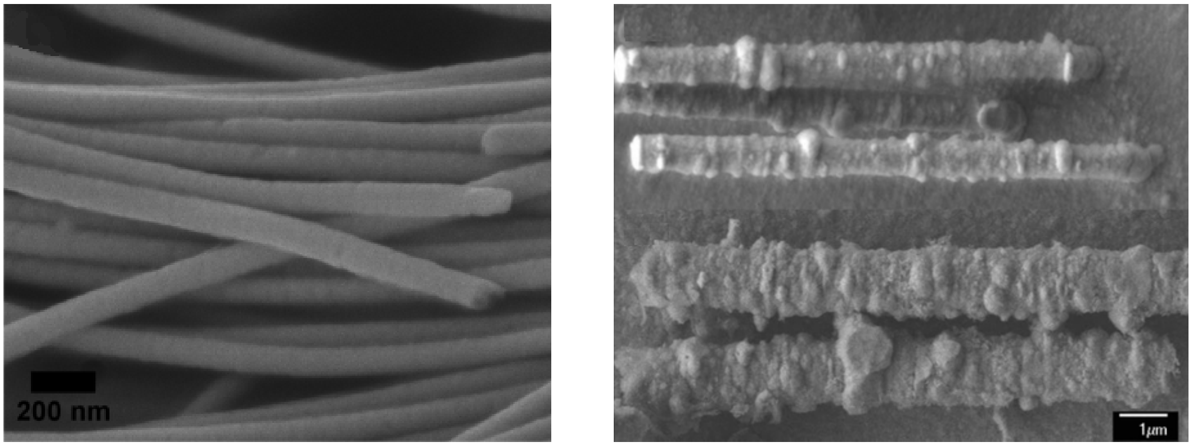

Figure 3.9: **Scanning electron microscope images of metal replica of track-etched PC (left) and PET (right) pores[20].** The pores were filled with metal and the polymer was completely etched a way, leaving a metal structure that is the inverse image of the pore. The metal was imaged in a scanning electron microscope. While the PC pores are nearly perfectly cylindrical in shape, the PET pores are characterized by rough inhomogenities across their entire surface, punctuated with large local bumps. The large bumps in the images of the metal replicas correspond to equally large cavitities in the PET pore. **Copyright:** Left: Image adapted from Müller *et al.*. Cryst. Growth Des. **12**, 615-621 (2012). Copyright 2012 American Chemical Society. Right: Figure adapted from Innes *et al.* Velocity Profiles in Pores with Undulating Opening Diameter and Their Importance for Resistive-Pulse Experiments. *Analytical Chemistry*, 86 (20), 10445-10453, 2014. DOI: 10.1021/ac502997h.

dynamic time warping algorithm has determined, so as to verify that the point matching system is meaningful. In order to do so, we traverse through the matrix starting at point $(N-1, N'-1)$ in reverse, according to the reverse kinematic rules. At each step, we move to the nearest adjacent point with the minimum distance. This algorithm is guaranteed to return us to the starting point $(0,0)$ along the complete minimum path between start and finish. This trajectory is shown by the yellow dashed lines in figure 3.8, and the pointwise connections are shown in Fig. 3.7(right)[23].

3.2 Experiment

In order to test the method described above for determining the lengths of particles, we performed resistive pulse experiments with single mesopores ranging from $800-1000\,\mathrm{nm}$ in

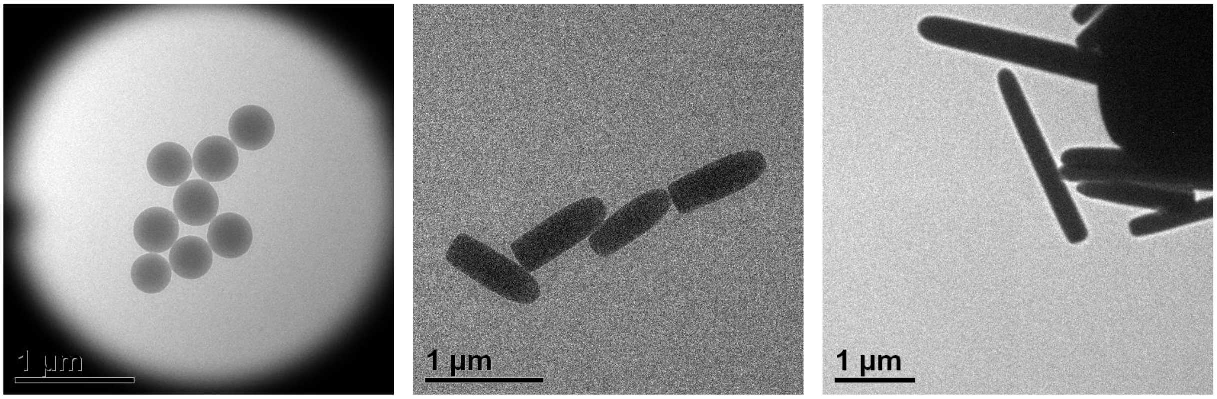

Figure 3.10: **Transmission electron microscope images of polystyrene beads and silica nanorods.** While the polystyrene beads are nearly perfectly spherical, the silica nanorods are approximately ‘bullet shaped’. For the purposes of this work, we approximated their shapes as ellipsoids in order to apply equation 3.2.

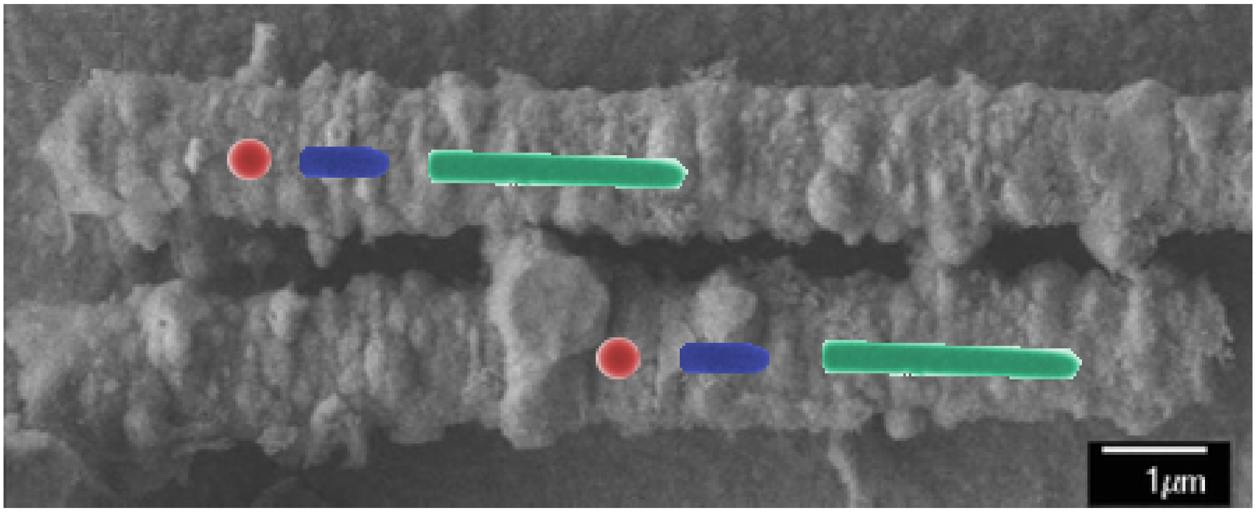

Figure 3.11: **Images of particles alongside PET pores, to scale.** Notice that the spheres and rods are small enough to accurately map the interiors of the pores, since their length is comparable to or smaller than the length of the length scale of the irregularities in the pore. On the other hand, the long rods extend along many such irregularities at any given time, and therefore will produce low-resolution maps of the pores’ interiors. **Copyright:** Figure adapted from Innes *et al.* Velocity Profiles in Pores with Undulating Opening Diameter and Their Importance for Resistive-Pulse Experiments. *Analytical Chemistry*, 86 (20), 10445-10453, 2014. DOI: 10.1021/ac502997h.

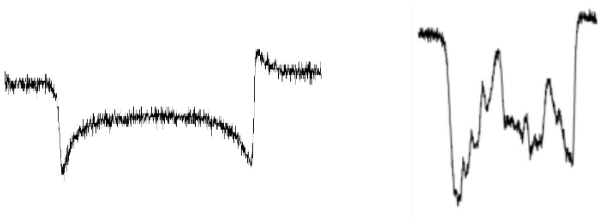

Figure 3.12: **Resistive pulse events through PC (left) and PET (right) pores.** As expected, the PET events are highly irregular and reflect the interior irregularities of the PET pore itself. On the other hand, the PC pores show no such irregularity. The events show that PC pores have large resistances at the beginning and end, reflecting the narrow, 'pinched' diameters at the openings of the pores.

diameter. The materials used were polyethylene terephthalate (PET), a polymer which is known to have highly irregularly shaped interiors when pores are prepared *via* the track-etch technique, and polycarbonate (PC), another polymer but with no axial inhomogeneities. The PET pore will be used to test the length measurement protocol, while the PC pore will be used as a control pore. Figure 3.9 shows images of both of these types of pores. For the particles, 280 nm and 410 nm in diameter polystyrene beads ('spheres') and silica rods[27] of length 590 nm, diameter 210 nm ('short rods') and 1920 nm, diameter 240 nm ('long rods'). The particles are shown in figure 3.10, and a figure showing the relative sizes of the particles to the PET pores is shown in figure 3.11. Particles were suspended in 100 mM KCl solution with 0.5% Tween 80, a surfactant which prevents particle aggregation. The solution was then injected into both sides of a conductivity cell, and a voltage was applied across the pore. The resulting ionic current was sampled at 20 kHz and recorded. The polystyrene spheres used had a larger $\zeta -$ potential than the pore, and therefore they translocated through the pore electrophoretically. On the other hand, the rods had a lower magnitude $\zeta -$ potential than the pore, and therefore travelled through the pore under electroosmotic convective forces[38].

3.3 Analysis & Discussion

3.3.1 Anomalous resistive pulse amplitude for short rods

Events were extracted from the current time series and studied separately; figure 3.12 shows two events, one from a PC pore and one from a PET pore that are representative of the translocations through each type of pore. In the initial analysis, we looked at the average $\Delta I/I_p$ of the beads and rods and compared with the theoretical predictions of Eqs. 3.1 and 3.2.

Figure 3.13 shows the results for two pores, one 770 nm and another 1200 nm in diameter. For the two spheres studied, the measured $\Delta I/I_p$ was very close to the theoretical prediction (Eq. 3.1). The theoretical predictions were also very close to the measured values for the long rods. However, for both pores the theoretical prediction of the resistive pulse amplitude $\Delta I/I_p$ is far off for the short rods: the data shows a nearly 100% discrepancy, i.e. the measured $\Delta I/I_p$ is nearly twice its expected value. This significant of a discrepancy is highly unusual, and one of the goals in this work was to determine its cause. The discrepancy is made even stranger by the fact that the short and long rods are both made of silica, so any material contribution to the discrepancy e.g. due to large $\zeta-$potentials. Instead, we hypothesized that this discrepancy is due to rotational dynamics. Equation 3.2 predicts that a prolate spheroid (like the rods) will have a larger $\Delta I/I_p$ when they are oriented with an off-axis component, but the equation only considers static positioning. A very large rotational speed of the rods could couple to the measured $\Delta I/I_p$ amplitude in ways not captured by the equation, for instance by stirring the local solution in such a way that the local ion mobility—and hence conductivity—is reduced. Furthermore, this hypothesis is consistent with the non-observance of the increased $\Delta I/I_p$ for the long rods, since at their length of $\sim$ 1920 nm they are too large to fully rotate in even the larger of the two pores (1200 nm in diameter). In any case, the net result is a measured volume for these particles that is

(a) 770 nm PET pore

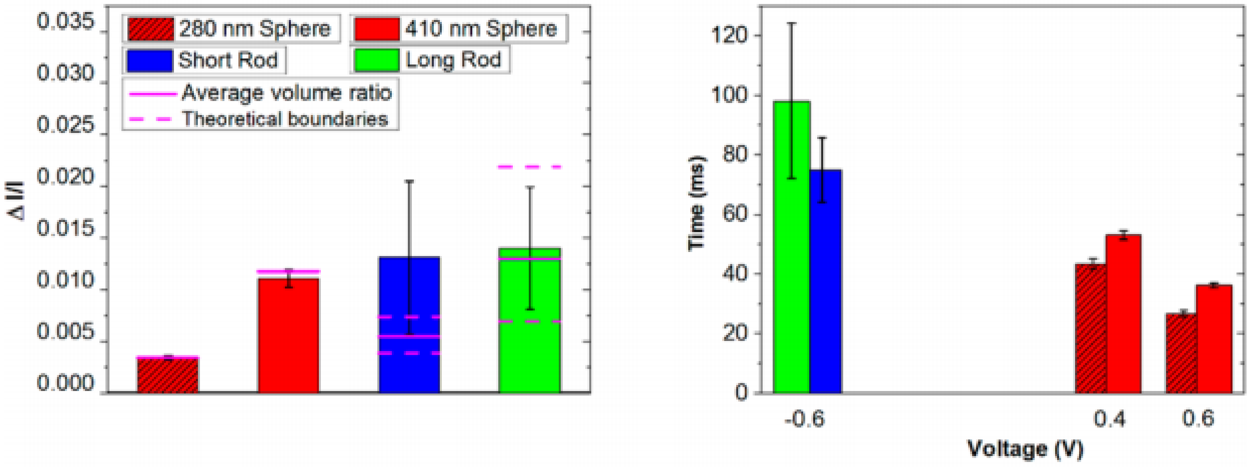

(b) 1200 nm PET pore

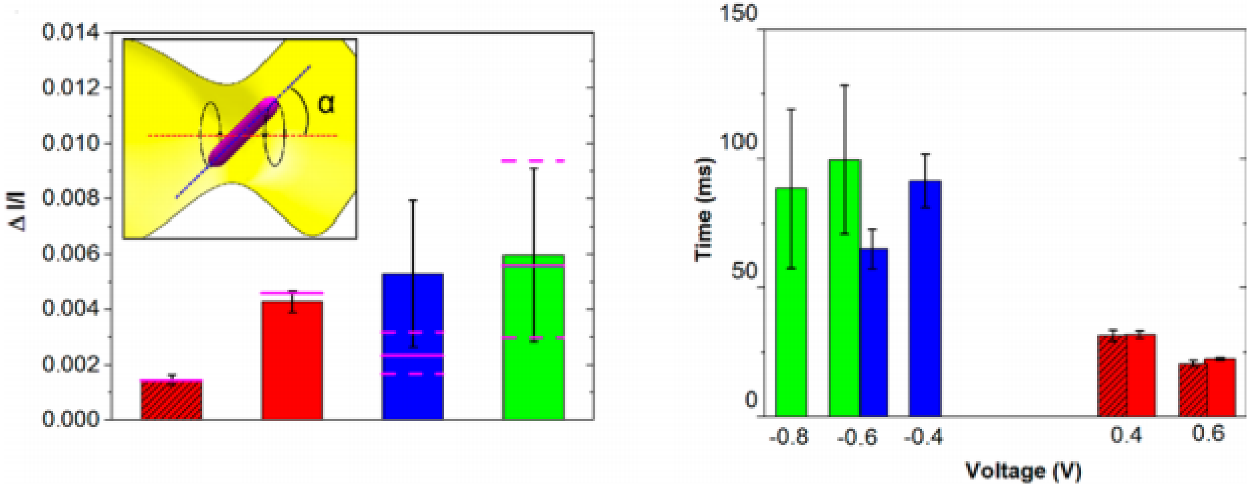

Figure 3.13: **Resistive pulse amplitude average and standard deviation for the particles studied in two types of pores and their theoretical predictions (left), and event duration versus voltage plots (right).** The experimental predictions for the resistive pulse amplitudes are largely correct, except for the short rod events (blue box), which is off by at least a factor of two in both cases.

approximately 2× larger than their actual volume, which was confirmed with a combination of transmission electron microscopy images and dynamic light scattering.

3.3.2 Length measurement protocol test

Next, we return to the idea of using the PET pore signals to measure the lengths of unknown particles. Figure 3.14 shows sample events of the three types of particles used in this study.

In order to demonstrate the qualitative differences between the signals of the long rods and the signals of the spheres and short rods, we plot three representative samples together in Fig. 3.15. The top signal of each column in the figure shows the raw signal of each of the particles. We plot the signals that have been transformed *via* the moving average process below these raw signals. The time over which the moving average was calculated corresponded to the duration in time over which the particle travelled a distance equal to the length of the longer particle with which it is being compared. We determined the average velocity of a particle from the total translocation distance (the known length of the pore, $L' = L - D$) and the translocation duration measured from the RP signal, Δt. The velocity is then $v = L'/\Delta t$. The moving average window then has length (in time) of v/l, which corresponds to a window of $N = f \times \frac{v}{l}$ data points. In the central column, the transformed sphere and short rod bear similarity, but this is unsurprising due to the fact that both particles are smaller or comparable to the characteristic size of the pore's undulations, as shown in Fig. 3.11. On the other hand, in the third column we show the transformed signals of the sphere's signal and the short rod's signal under the long rod's raw signal. Notice that the moving average transformation, for both the sphere and the short rod, has produced a signal that is qualitatively very similar to the long rod. In particular, the sub-minima and maxima in each of the raw signals of the short particles have disappeared, leaving only the larger scale features in the signals. Without making any quantitative arguments, we are able

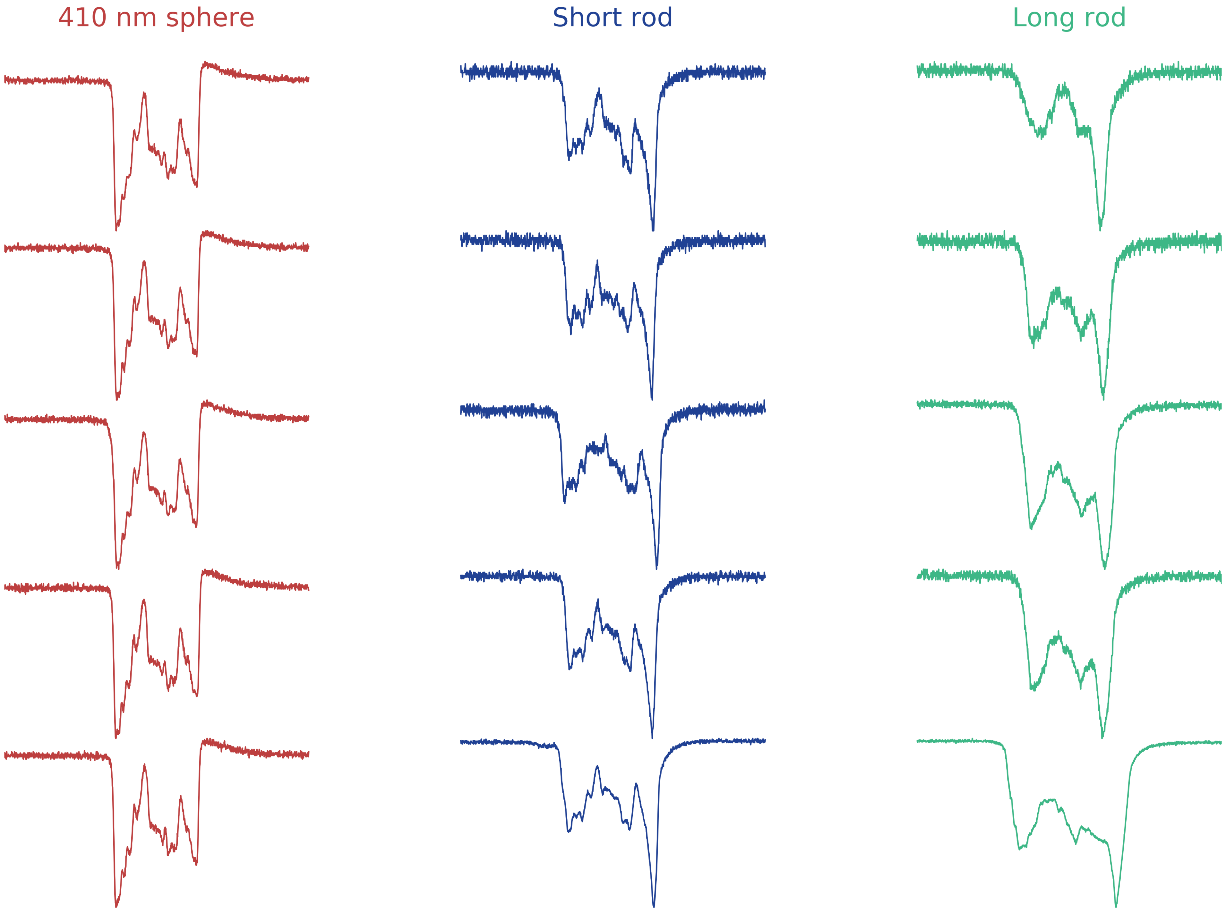

Figure 3.14: **Resistive pulse events for polystyrene spheres, short rods, and long rods through a particular PET pore.** The pulses indicate that the resistive pulse process is repeatable, as only small variations exist from signal to signal. While the signals of the spheres and rods are similar, in agreement with the model presented for how they accurately resolve the interior features of the channel, the signals of the long rods are quite different. Each of the long rod signals resembles the signals of the spheres and short rods, but with less resolution.

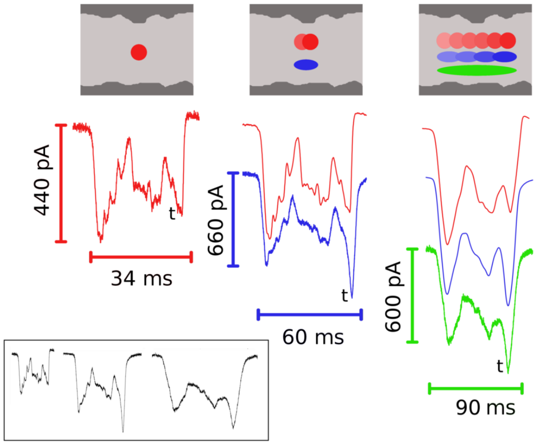

Figure 3.15: **Resistive pulse events of a** 410 nm **diameter sphere (red), and** 590 nm **(blue) and** 1920 nm **(green) in length rods.** The top row shows a cartoon scheme of the pore with the particles inside its interior. The bottom resistive pulse event in each column corresponds to the raw recorded data; events above this are smoothed *via* the moving average transformation. The bottom left figure shows the raw events on the same scale.

to conclude that the particle corresponding to the green event is longer than the particle corresponding to the red and blue events event[38].

In order to test the quantitative algorithm for particle length determination, we used the short rods as the 'tracer particle'. In principle we could use the signals of the spheres, but while their moving average signal is qualitatively similar to the long rod's signal, it still differs in significant ways. In particular, the initial and final minima have drastically different amplitudes. This effect is due to entrance/exit effects related to increased sourcing of ions due to the charge of the particle, and is therefore expected [31].

In order to measure the lengths of the long rods, we performed the dynamic time warping technique described in the preceding section. Figure 3.16 shows a shorter rod particle averaged over many different length intervals. As the short rod is averaged over a greater length interval, it continuously transforms into a shape that bears a stronger resemblance to the signal of the long rods, up to a point at which is smoothes the signal beyond the way the long rod does. Of all the fits calculated in Fig. 3.16, the correct length is determined by

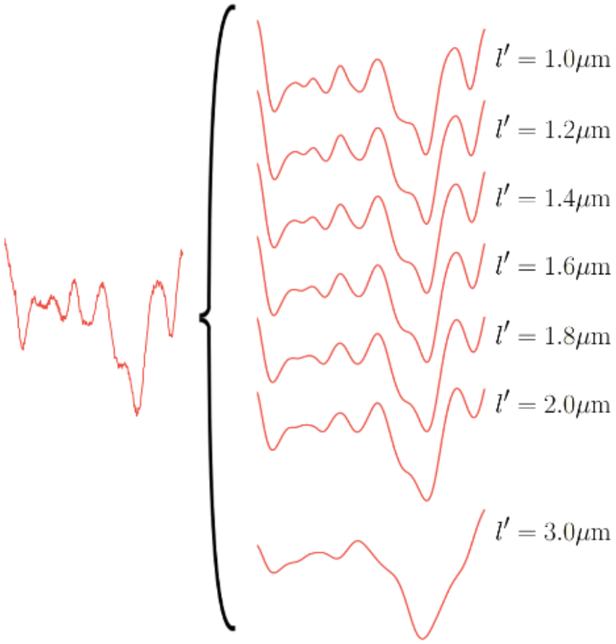

Figure 3.16: **Resistive pulse signal of a single short rod passing through a PET pore alongside many simulated instances of the event for moving average transformations applied over a variety of lengths.** As the length interval is increased, the finer structure of the resistive pulse signal is smoothed over. For the greatest length measured, many of the features prominent in the raw signal have disappeared.

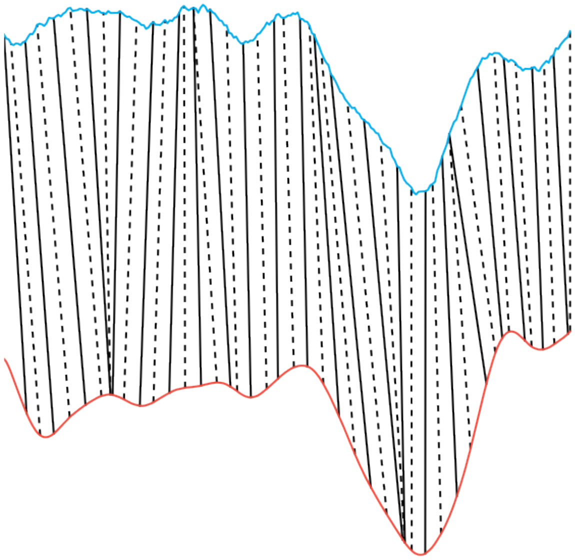

Figure 3.17: **Raw resistive pulse signal of a single long rod matched with the signal of a short rod that has been transformed via the moving average process.** The aligned points were determined by the dynamic time warping algorithm, and the particular transformation shown was the one that minimized the difference between the two signals, also determined by the dynamic time warping algorithm.

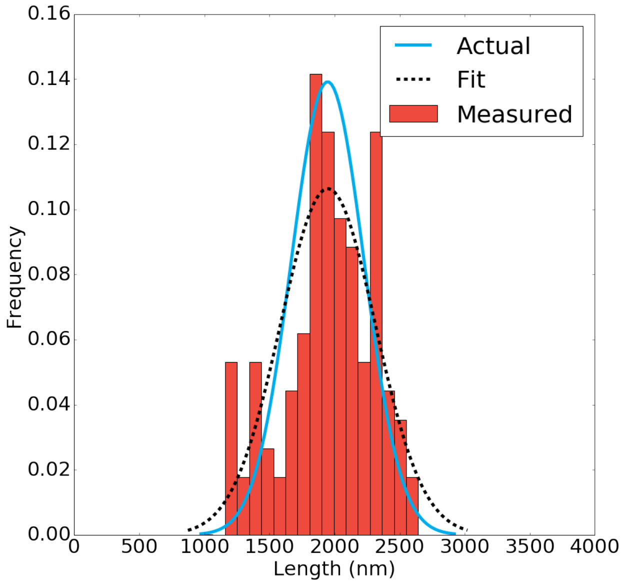

Figure 3.18: **Histogram of particle length as determined by dynamic time warping along with the actual distribution of sizes determined by electron microscopy imaging.** A normal distribution is fit to the histogram of particle lengths as determined by dynamic time warping and shown to be in good agreement with the expected distribution.

the fit with the smallest cost as determined by dynamic time warping. An example resistive pulse signal of a long rod and a shorter rod that has been transformed *via* the moving average equation is shown in Fig. 3.17. Finally, after performing the moving average and dynamic time warping minimization approach described above, we were able to determine the expected lengths of the long rods according to this algorithm. Figure 3.18 shows a plot of histograms of the lengths as determined by this approach, alongside a Gaussian fit to the histogram, and a Gaussian distribution that shows the actual distribution of the lengths of the long particles as determined by electron microscopy. The figure reveals that, in this case, the dynamic time warping algorithm is able to successfully recover the real distribution of the known lengths relatively accurately.

3.4 Conclusions

In summary, we presented resistive pulse experiments performed with spherical and non-spherical particles in two types of pores, those with smooth interiors (PC) and rough interiors (PET). We devised a protocol for measuring the lengths of long particles by taking advantage of the rough interiors of PET pores, which reflect in the measured resistive pulse signals of all the particles. Longer particles displace a greater distance along the pore's length, and therefore their signals are a more smoothed version of the signals of shorter particles[38]. This smoothing attribute can be recovered by taking the moving averages of shorter particles. By performing moving averages for many different particle lengths and measuring the similarity between the raw signal of the long particles with each of the transformed signals of the shorter particles, we were able to determine the length distribution of the long particles used in experiments. Dynamic time warping was used as a means of effectively comparing the similarity of the signals of the two particles[23]. While the general premise of the 'smoothing' of the resistive pulse signals by long particles compared to short particles is convincingly established, more research must be performed on the hybrid moving average-dynamic time warping method. The protocol was only tested for a small number of pores and only two types of particles, short and long rods. In the future, an ideal experiment could be performed with short rods of known length, and rods of various unknown lengths. The experiments and analysis would be performed in a blind fashion, and only after the analysis is complete would the true length distribution of the long rods be revealed. If the length measurement protocol survives this blind study, it would prove to be a very effective means of determining the lengths of particles.

Additionally, an unrelated phenomena was discovered where short, aspherical particles created far greater (up to 2x) resistive pulse amplitudes than predicted by the well-established classical equations. The exact reason for this effect is still unknown, however we laid out arguments that explain rotational dynamics as a likely culprit. We reasoned from our studies that an extremely rapid rate of rotation could effectively increase the radius of the particle, possibly by disturbing the local solution and decreasings its conductivity. Such rotations would not be possible for the longer rods due to their prohibitively long lengths compared to the diameter of the pore. However, more investigation must be performed in order to convincingly show that not only do short rod like objects deviate strongly from the classical equations, but also that rotational dynamics is the culprit. Additional experiments must be performed with a larger variety of short rods to show that the effect is general and not limited to the rods used in this study. Furthermore, experiments could be designed in such a way as to retard the rods' rotations, perhaps by using smaller pores or solution with an increased viscosity[38].

Chapter 4

Hybrid resistive-pulse optical detections in microfluidic systems

4.1 Background & Theory

As we have seen, resistive pulse (RP) sensing is a method for determining the physical properties of particles by way of measuring the change in resistance of a conducting channel they create as they pass through it[6, 8, 7, 2, 18]. RP's primary advantage is that it can be employed at many scales and in a diverse number of applications, and is especially useful at the nanoscale where the number of particle characterization techniques is limited—in particular, optical imaging is prohibited at this scale. To first order, the mechanism for the RP current pulses is straight forward: when the particle enters the channel, it occupies a volume that would otherwise be occupied by ions, decreasing the conductance, and increasing the total system resistance. According to this simple model, the resistive of the system is determined solely by the equation

$$R = \rho \int A^{-1}(x)\, dx, \tag{4.1}$$

where R is the system resistance, $A(x)$ is the annular cross-section of the channel at position x, and ρ is the resistivity of the solution[7]. In most RP set ups, the current is measured instead of the resistance, so Eq. 4.1 is usually inverted via Ohm's law to obtain the current: $\Delta I/I_p = \Delta R/R_0$, where I is the measured current, and the subscripts 0 and p denote quantities when the channel is empty, and occupied, respectively. While Eq. 4.1 serves as a good approximation for the RP amplitude that may be accurate in some cases, it fails to take into account the electrodynamic boundary conditions present in the system, namely that the normal component of the electric field vanishes at the surface of the insulating layer, or $\vec{E} \cdot \hat{n} \,|_{\text{surface}} = 0$. The effects of boundary conditions can have a large influence on the measured RP amplitude that is position and geometry dependent, and therefore, most importantly can affect measurement of the size of a particle from the RP amplitude. Therefore, significant efforts have been directed towards finding more accurate expressions for specific particle and channel geometries. For instance, Smythe calculated the expected RP amplitude for spheres passing along the axis of cylindrical channels, and arrived at the expression

$$\frac{\Delta I}{I_p} = \frac{d^3}{LD^2}\left[1 - 0.8\left(\frac{d}{D}\right)^{-3}\right]^{-1}, \tag{4.2}$$

where d and D are the diameter of the particle and pore, respectively, and L is the length of the channel[7, 43]. Equation 4.2 is probably the single most useful equation for sizing particles in RP experiments, however due to the preceding arguments we know it is only an approximation. For instance, the equation does not consider particles that travel off-axis, and it also assumes a channel length that is far greater than the length of the particle to be sized. Furthermore, it is only accurate for cylindrical channels and spherical particles. Few real-world experimental RP systems hold to these sterile conditions.

The typical route taken in cases where Eq. 4.2 cannot fully capture the experimental findings is to devise a model that relates the position of the particle, the particle's geometry, and the geometry of the channel to the expected RP amplitude. Then, based on the model, conclusions are drawn from the RP signal about the positioning and dynamics of the translocation. As a concrete example, Berge *et al.* observed a positive correlation between the translocation times and the RP amplitudes of microbeads that were driven through their channels by an applied pressure. They argued that, due to the Poiseuille flow profile present in their channel, a larger translocation time correlated to an off-axis displacement. The correlation between translocation time and amplitude then suggested a correlation between off-axis displacement and increases RP amplitude, which they explained was due to the increased distortion of the electric field, which increases the total system resistance, when the channel drifted laterally from the channel axis[3]. As another example of an RP system which invalidated the conditions of Eq. 4.2, Tsutsui *et al.* performed RP experiments with spheres in low-aspect ratio pores and found a significant variance in the observed RP amplitudes that could not be explained by size variance in the population alone. They argued, therefore, that the combination of particle and channel geometry created a unique situation where the observed RP amplitudes were highly trajectory dependent, and they then devised a model to relate the trajectory to the RP amplitude[52, 51].

In both of the above examples, the one-dimensional RP data set is used to study the complex dynamics of particle translocations through pores. The authors' inferences could very well be accurate, but could easily be validated or clarified by simply observing the translocations while simultaneously recording the RP data. However, the difficulty in performing such an experiment is the physical scale at which they worked; at the nanoscale, only electron microscopy is viable due to the optical diffraction limit. In most cases, *in situ* electron microscopy during an RP experiment is prohibitively difficult. However, because RP experiments are largely scale independent, one possible option is to scale the solution up to a size where optical diffraction is possible, and to perform simultaneous RP and optical measurements. Such experiments could be used to clarify the positional dependencies of the RP signal, and the results could be generalized back down to the nanoscale.

In order to resolve the positional dependencies of the RP amplitudes, we devised a microfluidic experimental and data analysis platform that allows simultaneous RP and IM measurements and analysis. The experimental system is based on a high-speed camera combined with an optical microcope which captures images of particles as they pass through a microfluidic channel while the ionic current is simultaneously recorded (described in greater detail in the following section). By tracking particles simultaneously in the two data streams, we are able to create a position-RP amplitude mapping for each particle. The mappings of many particles are combined to create a 'resistance map' of the channel, a two-dimensional plot of the local resistance in the channel as measured by the instantaneous RP amplitude $\Delta I/I_p$, and which can address specific questions about the positional dependencies of the resistive pulses. Such questions include but are not limited to:

- At which axial position does the RP amplitude attain its maximum value?
- What is the effect of lateral displacement of a particle inside the channel on its resulting RP amplitude?
- How is the variance distributed in variable-width channels, such as channels having a central cavity?

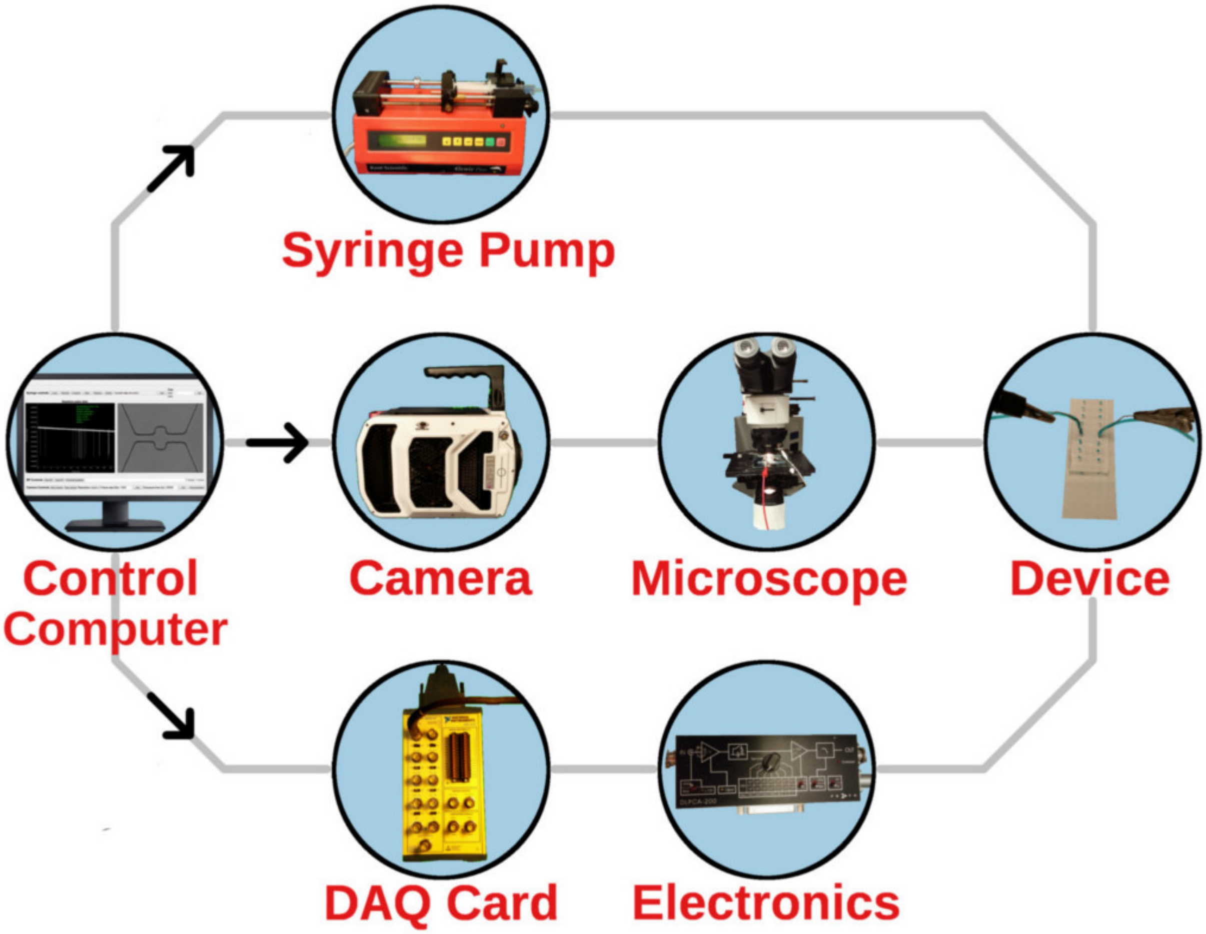

Figure 4.1: **Hardware set up for the hybrid RP-IM experiments.**

4.2 Experimental hardware and software

We devised a hybrid resistive pulse-optical imaging platform that is capable of resolving the spatial dependencies of the RP amplitude signals. The set up (Fig. 4.1) consists of a high-speed camera combined with an optical microscope, all of the electronic equipment used to acquire the RP signal, a syringe pump to drive particle suspensions through the system, a planar microfluidic channel, and a central control computer used to run the experiment and record data.

The program used to control each of the instruments used in the experiment was written in C++ and makes use of the Qt framework to provide a GUI environment in which to run the

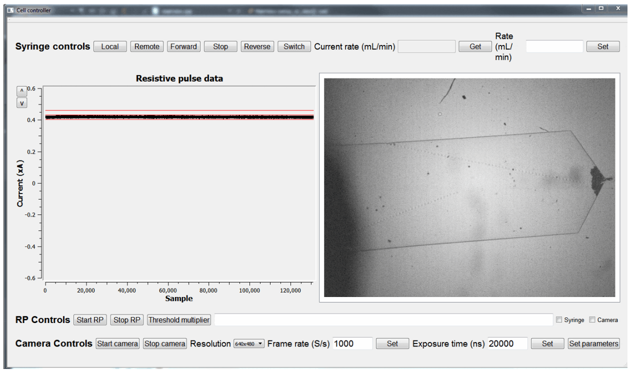

Resolution 640x480

Frame rate (S/s) 1000

Exposure time (ns) 20000

Figure 4.2: ***cell_controller*, a GUI program written in C++ and the Qt Framework**. The program controls the instruments used to run the experiment and enables simultaneous recording of the RP and camera data.

experiment. The program is open-sourced and available at https://github.com/tphinkle/cell_controller. The software controls the high-speed camera, a data acquisition (DAQ) card used to record the current measurements, and the syringe pump. Each instrument uses its own communication protocol; the high-speed camera is controlled by commands sent via TCP/IP protocol over a 1 GB/s ethernet line, the DAQ card is controlled using the National Instruments NIDAQmx API, and lastly, the syringe pump is controlled via serial commands sent over an RS-232 line. A screen shot of the program is shown in Fig. 4.2.

The channels used for these experiments were made from PDMS bonded to a glass slide. The entire fabrication procedure is described in the above table. PDMS is a transparent elastomer that is relatively inert, durable, and inexpensive, and for these reasons is probably the most common material used in microfluidic experiments today[10]. Two classes of channels were created in PDMS, constant-width and variable-width, which will be discussed separately in the discussion section. Within each class of channels, different geometries were considered. Images of some of the channels used in the experiments are shown in Fig. 4.6, along with lines indicating the tracked trajectories of individual particles (discussed below).

$5\,\mu$m polystyrene beads were used as the experimental particle to track, and were suspended in $1\,$M unbuffered KCl solution at concentration 2×10^8particles/mL. The high molar con-

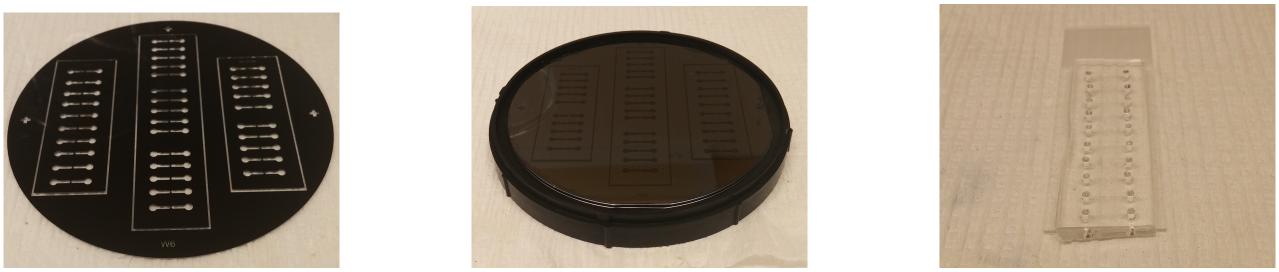
(a) **Printed phototransparency of microfluidic channel designs.**

(b) **Channel mold patterned on SU8 photoresist, on a silicon wafer.**

(c) **Final PDMS and glass device configuration.**

Figure 4.3: **Key ingredients in the microfluidic channel fabrication process.** The transparency image is patterned onto the SU8 using soft photolithography techniques. PDMS is poured over the patterned SU8, which acts as a mold, and is cured on a hot plate. After curing, individual devices are cut out and have holes punched through them at the inlet and outlet points to allow access for the tubing. The glass was bonded with the PDMS channels after both were treated in an oxygen plasma. Each row of holes corresponds to a single channel.

centration of solution was chosen to maximize the signal-to-noise ratio of the RP events. The syringe pump rate was chosen to be 0.005 mL/min. This flow rate was chosen to enable a large number of events to be detected while also allowing for good sampling of individual events in both the RP (250.000 kHz) and IM (50.000 kHz sample, 10 μs exposure) signals. At this flow rate, particles traveled a small (<5 μm) distance in between frames, and minimal blurring occured. The *cell_controller* program recorded the camera and RP data simultaneously so that the two data streams were guaranteed to capture the same particle translocations.

4.3 Data analysis software

A software library called *pore_stats* was written in Python and PyQt to facilitate analysis of the RP data. The program includes a GUI application that can be used to quickly isolate the RP from the entire time-series. The GUI application has a number of features that facilitate signal extraction, including functions to find events in a drifting or unsteady baseline, to

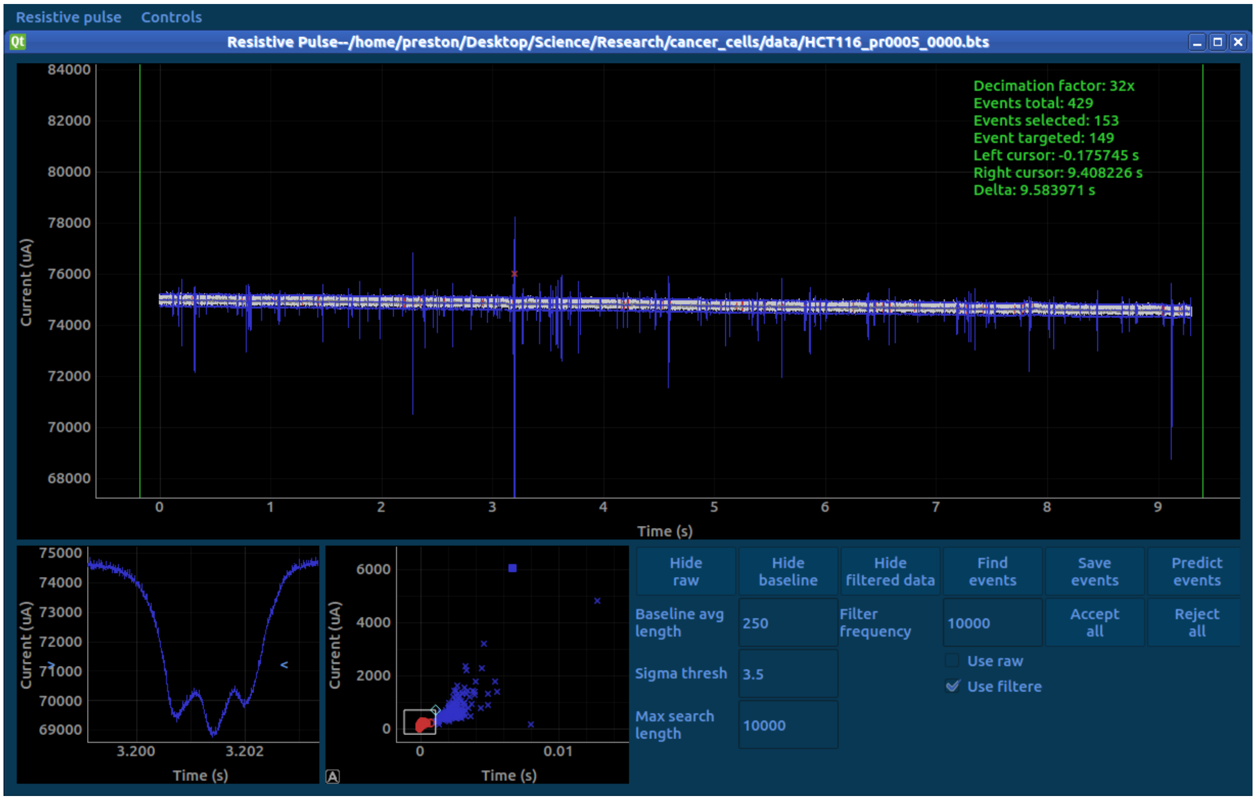

Resistive Pulse--/home/preston/Desktop/Science/Research/cancer_cells/data/HCT116_pr0005_0000.bts

Decimation factor: 32x
Events total: 429
Events selected: 153
Event targeted: 149
Left cursor: -0.175745 s
Right cursor: 9.408226 s
Delta: 9.583971 s

Baseline avg length: 250
Filter frequency: 10000
Sigma thresh: 3.5
Max search length: 10000
☐ Use raw
☑ Use filtere

Figure 4.4: **Screen capture of the GUI component of the *pore_stats* software library.** The program enables fast and accurate extraction of RP events from the baseline data. The main panel shows the raw time-series data (zoomed out), with events that were detected with the program highlighted in blue. The bottom left plot shows a single event that has been targeted by the user. The bottom right plot shows a scatterplot of the current amplitude and duration for all events detected, and shows how bulk events can be rejected by slicing out regions of interest. The bottom right buttons and fields are used to change the search parameters, to begin the search, to filter data, and to perform various other functions.

Step name	Instrument	Parameters
Preprocess cleaning	Isoproponal	
Wafer dehydrate	Dry oven	95°C, 30 min
First spin	Laurell spinner	(parameters)
Second spin	Laurell spinner	F
Soft bake (cold)	Hot plate	65°C, 1 min
Soft bake (hot)	Hot plate	95°C, 5 min
UV flood exposure	AMV	52 seconds (intensity varies, adju
Post-exposure bake (cold)	Hot plate	65°C, 1 min
Post-exposure bake (hot)	Hot plate	95°C, 5 min
SU8 develop	SU8 develop solution	5 min soak, with periodic agitat
SU8 developer rinse	SU8 developer solution	
Soft bake (hot)	Hot plate	95°C, 5 min
Post-photolithography bake	Hot plate	95°C, 2 hours
PDMS preparation	Sylgard-184 and curing agent	10:1 by volume Sylgard-184 t
PDMS degassing	Vacuum	30 min
PDMS cure on SU8 mold	Hot plate	75°C, 150 min
PDMS-glass bond	Harrick-Plasma oxygen plasma chamber	300 mT, med. power,

Table 4.1: SU8 photolithography procedure

apply a low-pass filter to the data that helps uncover events buried in the baseline, to rapidly filter events based on their amplitude and duration, and a function that allows the user to train a logistic regression machine learning model in order to make automatic future accept/reject predictions. A screenshot of the program is shown in Fig. 4.4. Aside from the GUI program, *pore_stats* contains a wide variety of functions contained in a library that can be called to perform operations on the RP data, such as filtering, minimum/maximum detection, etc., and to calculate the relevant RP parameters such as duration, amplitude, sub-amplitudes, number of events, event velocity, etc. Finally, because the experiments used for this project include simultaneous RP and optical tracking, the *pore_stats* library contains modules for analyzing the imaging data. The library enables detection of particles in individual frames, tracking of particles across frames, and a host of image processing tools that allow the user to calculate physical parameters of interest, such as particle size, aspect ratio, position, etc.

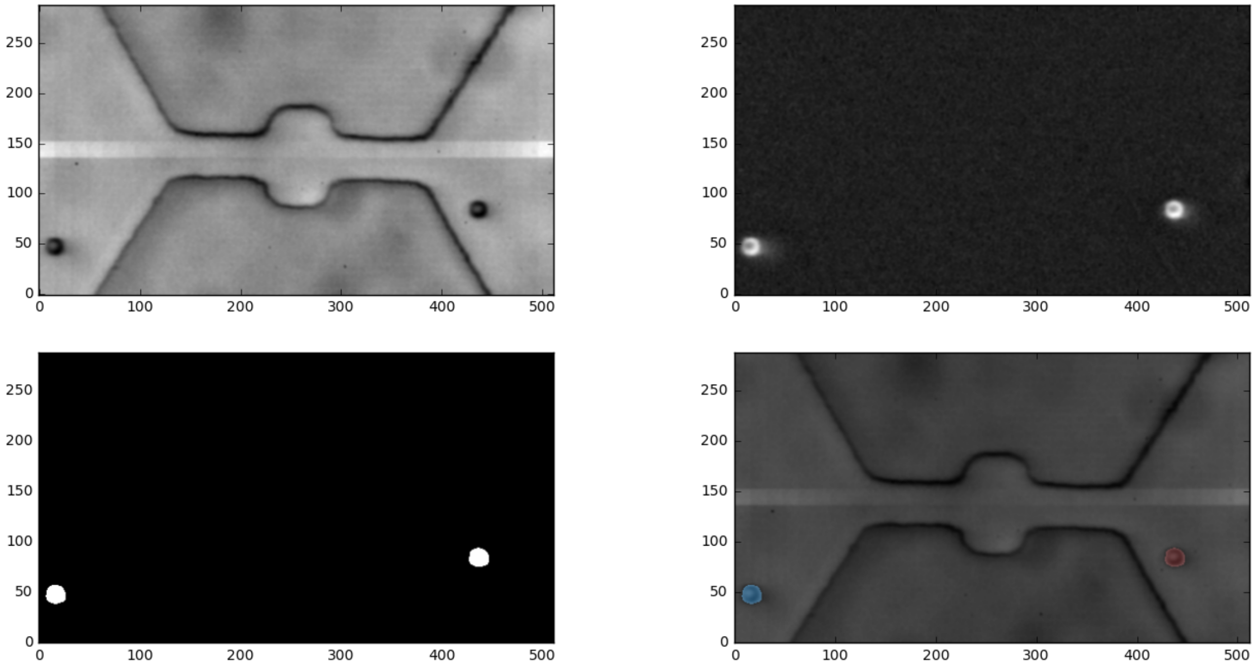

Figure 4.5: **Particle detection protocol. Top left:** Raw image. **Top right:** The raw image is subtracted off of the template image, which does not have any particles present in it. **Bottom left:** The negative image from the previous step is thresholded, so that all pixels exceeding some intensity threshold are set to white, and all pixels below this threshold set to black. **Bottom right:** Clusters are detected in the binary image in the previous step. Because the two particles are not touching, they are recognized as individual clusters, reflected in the image by their different coloration.

4.4 Results & Discussion

4.4.1 Data analysis explanation

The experimental hardware and software, and the data analysis software described above were used to perform the experiments and analyze the obtained data. The data analysis pipeline is as follows. First, the RP data was opened using the GUI application within the *pore_stats* library, which was used to extract the detected RP events. Once RP events were detected in the baseline of the time series, they were saved separately.

Next, the camera images were analyzed in order to track optical events. Particles were detected within individual frames using a thresholding approach, which works as follows.

A frame in which no particles were present was used as a template, which was subtracted off individual frames (the ‘negative’). Pixels that surpass a certain intensity threshold in the negative frame signal the presence of a new object in the frame, i.e. a particle. A flood-fill algorithm was then used to cluster all incidents of pixels surpassing this threshold. Each cluster of pixels corresponds to a unique particle detection in that frame. The detection scheme is then repeated for the next frame in the video, and the clusters detected in this frame are connected with the clusters in the previous frame using a minimum-distance approach. We repeat this for every frame in the video, continuously tracking individual particles as they pass through the channel. The end result is a list of optical ‘events’, where each event is a list of clusters, each cluster corresponding to the detection of that particle in a given frame. Figure 4.5 shows the process of how individual detections are located within a figure.

Because we know the exact geometry of the channel, we are also able to determine the physical length of a pixel in the camera image. This is useful because we can then measure distance in physical units (e.g., microns) instead of pixel units. Additionally, we can also use the lines of the channel to create a coordinate system with axes aligned with the axial and lateral directions of the channel. The end result is that through the coordinate transformation and particle tracking, we are able to calculate the actual trajectory in physical units that a particle undertakes when passing through a channel. The trajectory is then described by a sequence of pairs $\{x_c, y_c\}$, where $\{x_c\}$ are the axial and $\{y_c\}$ the transverse coordinates of the particle with respect to the channel’s coordinate frame, in physical units of microns. We chose a coordinate system such that $x_c = 0$ corresponds to the particle crossing the channel’s threshold, and $y_c = 0$ the channel’s axis.

In order to compare the events tracked via RP and IM, a protocol had to be established for matching the events appropriately. In order to do this, we first constructed two time series corresponding to the times of events of the tracked RP and IM signals. The times from one signal were shifted until both sequences were seen to overlap. In many cases tracking

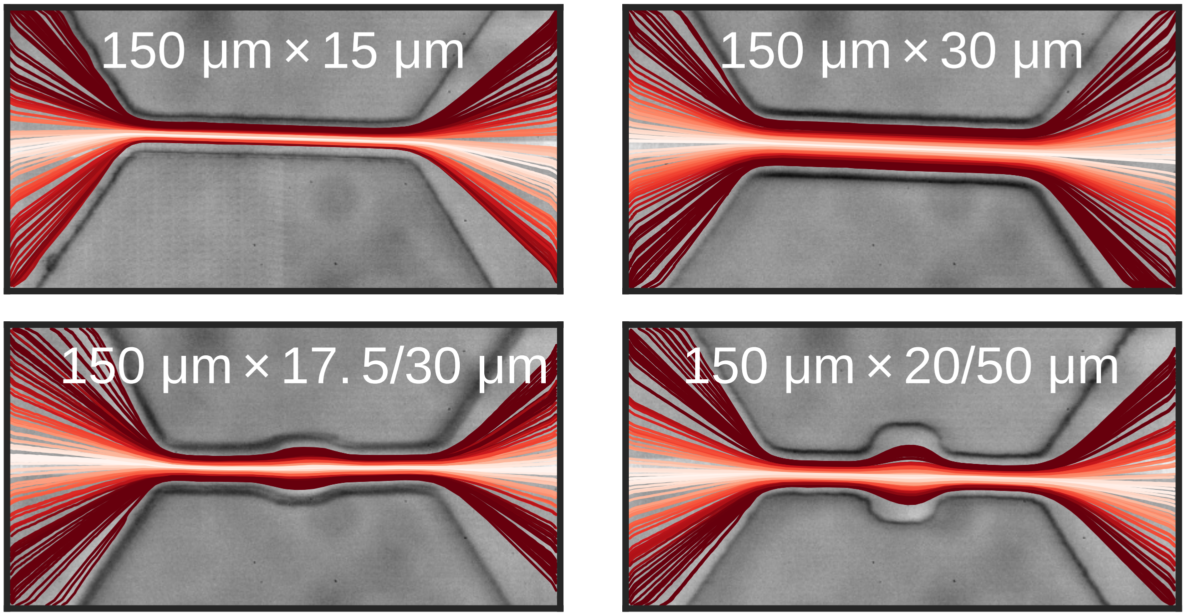

Figure 4.6: **Images of some of the channels used in this study with trajectory lines overlaid.** Each line corresponds to the passage of a single particle through the channel. The channels fall into two categories, channels that are completely straight and channels which have central cavities.

of some particles fails in either signal. For instance, in the RP signal there could be a brief burst of noise that prevents detection of a pulse in the baseline. In the camera data, failure to track a single particle was less likely to occur, although still possible in principle. Unpaired events were dropped from the respective sequence to which they belonged. After this coarse alignment, we are left with two sequences IM and RP such that every event i in one signal has a matching event i in the other signal that is known to correspond to the same physical particle translocation. However, in order to compare actual data points between the RP and IM signals, a more fine-tuned alignment must be made. In order to perform this exact matching, we find two data points that are known to correspond to the same instant in time (up to the precision of the slower of the two instruments' sampling periods). For instance, for a pair of detected events in the RP and IM signals, we find the camera frame where the particle occupies the exact center of the channel, and find the middle-most data point in the RP signal; we know that both data points correspond to the

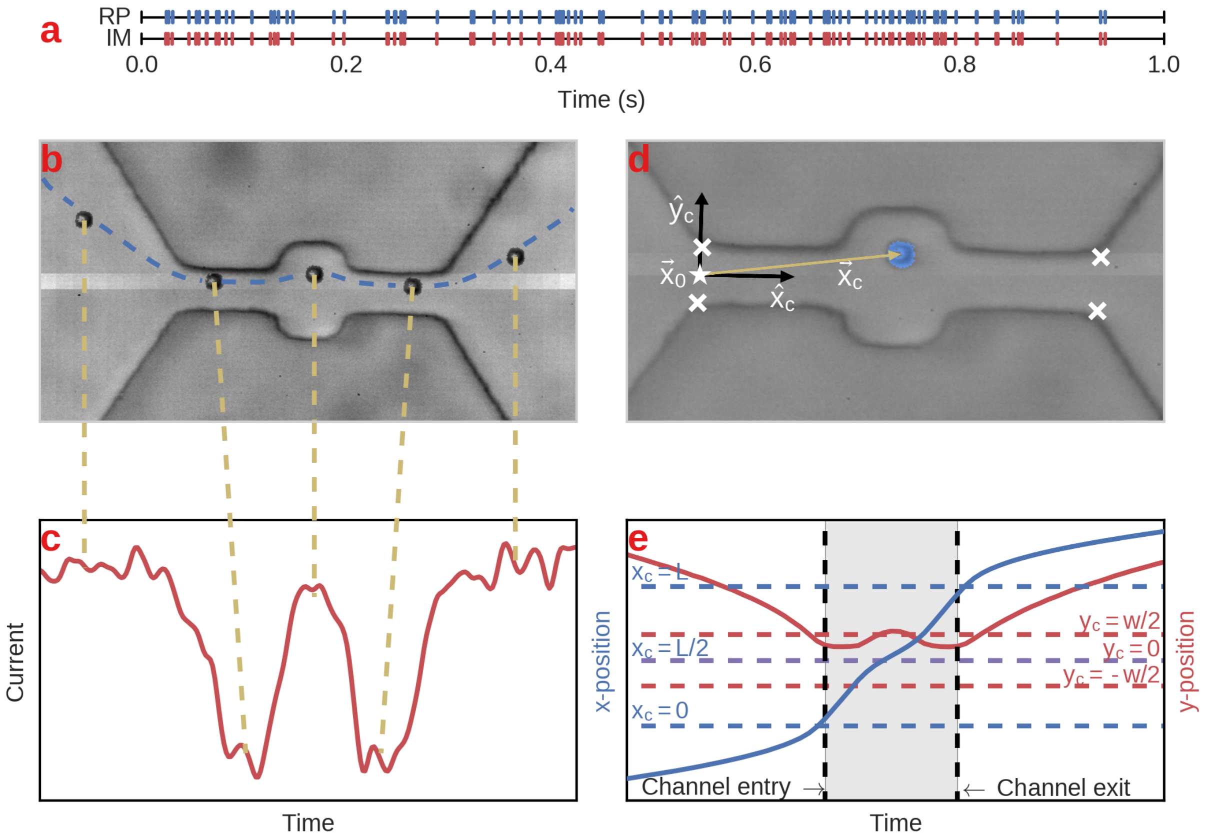

Figure 4.7: **Event matching protocol for the RP and IM signals. a**.

same instant in time (again, with precision given by the slower of the two sampling periods). Fine alignment of the two time series for each event is then achieved by adding a simple time offset to one of the signals, equal to the difference in times of the two corresponding data points. In principle, if the camera and DAQ card sampled at exactly the rates specified by their hardware specifications, fine alignment of the entire time-series would be possible by simply aligning the RP and IM data of a single particle translocation. However, in practice we find that if we apply this offset for a single particle, the signals become out of sync at a later time, which is due to slight inaccuracies in their reported sampling periods. For this reason, we apply a unique alignment for every pair of events that we compare. The inaccuracies that cause asynchronization of the two data streams across the entire recording are too insignificant to cause any misalignment over the duration of a single event.

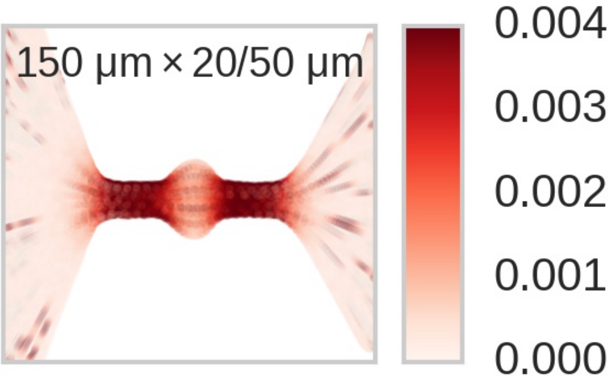

Figure 4.8: **An example resistance map.** In the map, each color corresponds to the local RP amplitude determined from the synchronized RP and imaging data.

After aligning the two time-series and calculating the position of the particle in the channel's coordinate system, we have a time-series of data $x, y, \Delta I/I_p$; in other words, for every event we are able to determine the exact $\Delta I/I_p$ for every position in the particle's trajectory through the channel. The event matching protocol, as well as calculation of the particle's positions in the channel's coordinate frame, are shown in Fig. 4.7.

Armed with the synchronized data set, we can now explore the positional dependencies of the RP signals. The matching between the RP and imaging data allowed us to create 'resistance maps' of the channels, pictures of the channel that show the amplitude of the $\Delta I/I_p$ at various points. An example resistance map is shown in Fig. 4.8. Each data point in the resistance map indicates the position of a single particle at a single point in time, and the color reflects the instantaneous value of $\Delta I/I_p$ at that same time[19]. In the following sections we analyze resistance maps for straight channels and channels with non-constant widths.

4.4.2 Straight channels

The geometries of the straight channels used in this study are shown in Fig. 4.6, top row. The resistance maps determined for these channels are shown in Fig. 4.9. All channels were

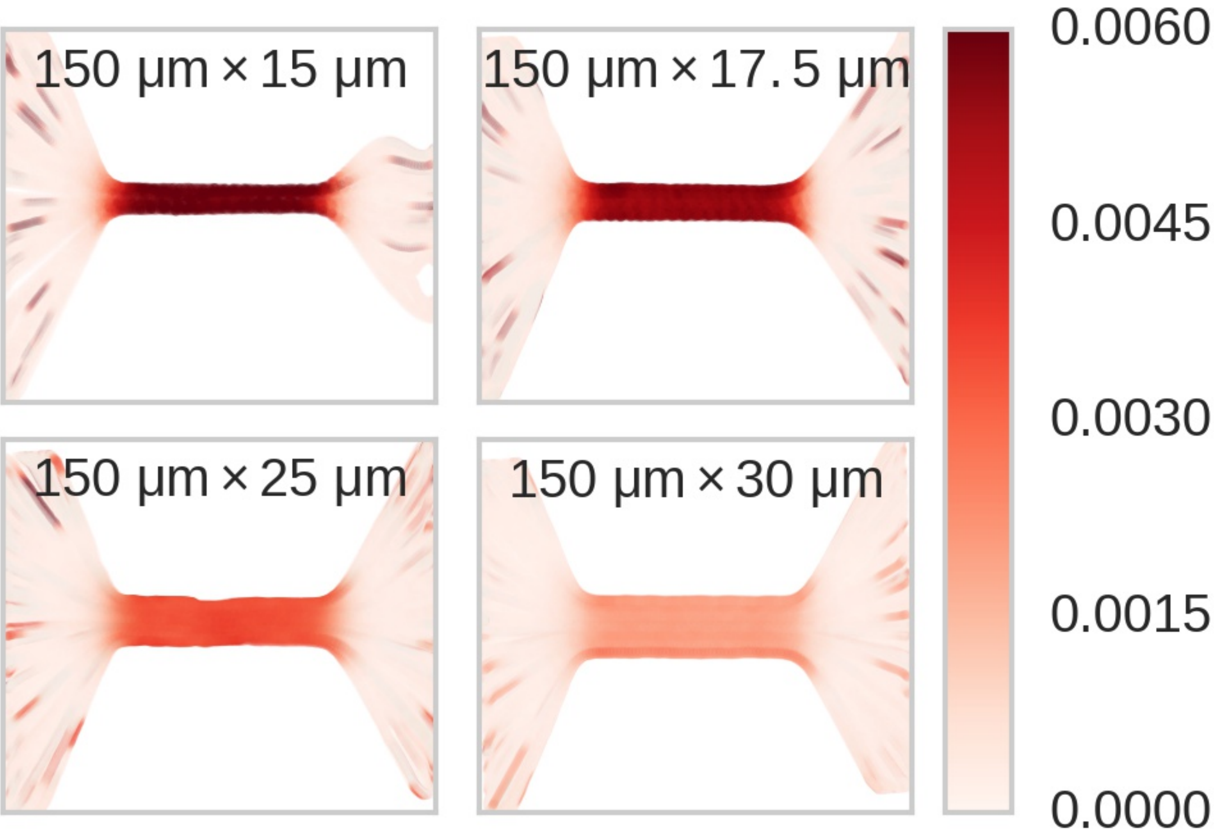

Figure 4.9: **Resistance maps of the straight channels used in this study.** The resistance maps show that the resistance is most concentrated in the micro constriction, and that the resistance is small elsewhere. A region of finite resistance exists between the micro constriction and the reservoir leading up to the channel. This region is known as the channel's access resistance. The color scale shown on the right is applicable to each channel. Whereas the intrachannel color in the smallest channel (15 μm) is a rich, dark red, the colors in the largest channel (30 μm) are in comparison much lighter, indicating a lower resistance for this channel. This relationship is in agreement with our basic intuition for the resistance of conducting elements.

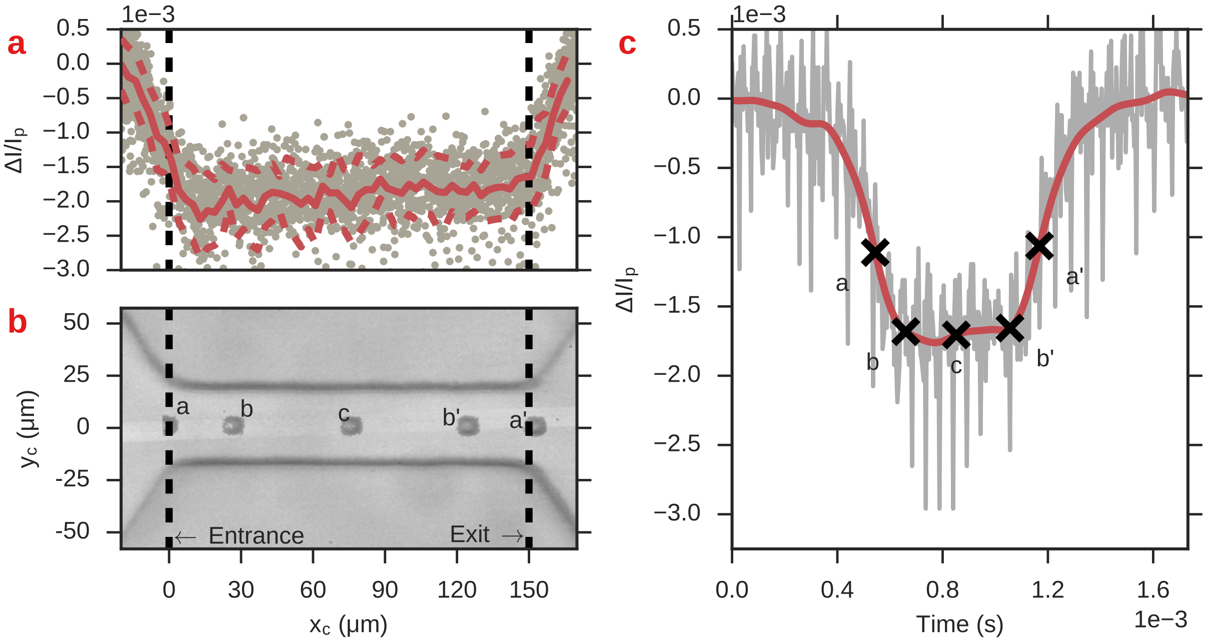

Figure 4.10: **Plot of $\Delta I/I_p$ vs axial-position x_c for polystyrene beads passing through the PDMS channels.** The plots reveal that the current does not reach its maximal value until the particle is well inside the channel, even beyond the point where it first becomes fully encapsulated.

approximately 20 μm in height. The interior regions of the channels show relativeliy darker red colors than the exteriors, indicating a higher resistance in accordance with our expectations. In the immediate vicinity of the channel, there is a region of moderate resistance known as the access resistance, which extends a small distance into the channel. In the rest of this section we delve into these aspects of the resistance map in greater detail.

Position of maximum RP amplitude in the channel

In the traditional RP technique, pulses are usually analyzed for their duration (sometimes called the dwell time) and their amplitude. The pulse duration is a measure of the particle's velocity, and if the particles are driven through the channel electrophoretically or through electroosmosis, this becomes a basis for measurement of the particle or channel ζ-potential, respectively[26]. However, an exact measurement of the dwell time is always somewhat arbitrary because there is no definitive point in the RP signal where we can say the start and stop of the event occurs. Typically some standard is adopted by the researcher for when the beginning and end of an event occur; most researchers choose to use the full-width-at-half-maximum (FWHM) as the points at which the particle enters and exits the channel. The resistance map will allow us to directly observe the current value at the entrance and exits of the channel, and to compare this with the FWHM of the signal to see if this standard is justified. We created plots of the axial position x_c and instantaneous current value $\Delta I/I_p$ for each event for the straight channels studied. Figure 4.10 shows a single event from the recorded RP time series alongside the data of many events plotted in coordinates of $\Delta I/I_p --- x_c$. The figure reveals two interesting features. First, the current does not plateau until the particle is well within the channel, even more than its full diameter. This result is unusual, and suggests that the entrance of the pore has less resistance than its entrance points, even though these points have the same width. Another result is that the point at which the particle crosses the threshold of the channel corresponds very closely to the FWHM of the pulse, a result which suggests that for the purposes of measuring the dwell time of the particle, the FWHM may be a more accurate estimate than a thresholding approach.

Dependence of resistive pulse amplitude on lateral displacement

As mentioned in the introduction to this chapter, off-axis translocation of a particle is expected to significantly effect the amplitude of the RP signal it creates. This effect is significant in sizing applications, where it broadens and shifts the distribution of the particles sizes as measured by RP. In order to better understand the effect of off-axis translocation on the RP amplitude, Berge *et al.* performed experiments with particles driven through pores by an induced pressure [3]. Pressure-driven flow results in a Poiseuille distribution of the fluid

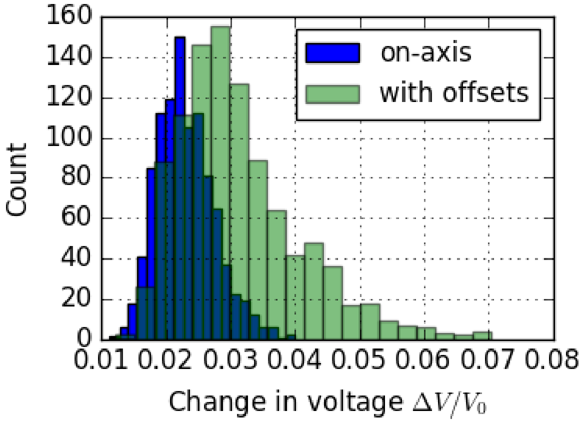

Figure 4.11: **Plot of the measured voltage of simulated particle translocations through a pore, with off-axis contribution according to the results of Berge *et al.* (Eq. 4.3)[3].** The plot reveals the effects of off-axis translocation, namely that the distribution of measured ΔV shifts towards greater values and broadens.

flow velocity, which parabolically varies between its maximum value at the channel axis and zero at the channel wall. Berge *et al.* used their knowledge of Poiseuille flow to determine the lateral offset position y_c of the particles based on their translocation time. They then observed that particles with greater lateral offset also had larger resistive pulse amplitudes, and constructed the following equation to fit the relationship for the two observables

$$\frac{\Delta V}{\Delta V_0} = 1 + \alpha \left(\frac{y_c d}{D} \right)^3 . \tag{4.3}$$

In the above equation, d is the diameter of the particle, D the diameter of the pore, and α was a fitting parameter determined to be between $5 - 7.5$. The equation shows that the distribution of diameters D as determined by RP is both broadened and shifted towards higher diameters by the off-axis effect. Figure 4.11 shows simulated data of particles passing through a pore and the resultant measured $\Delta V/V_0$ (the quantity measured by the authors in his original work).

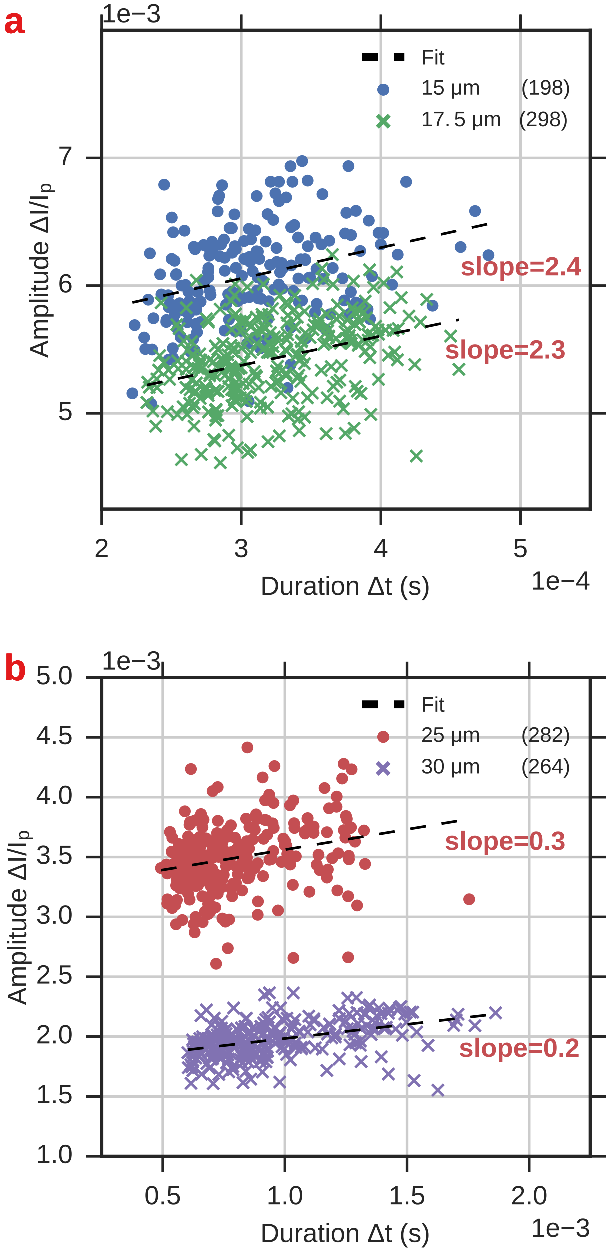

Figure 4.12: **Scatter plot of translocation duration Δt versus event amplitude $\Delta I/I_p$ and linear fits for the four straight channels studied.** The fits reveal the positive correlation between translocation time and off-axis position, an effect also observed by others.

Although the effect was well-established by the authors, it was only indirectly inferred from the data. Using the hybrid RP-IM approach, we can directly measure the effect of off-axis translocations in RP experiments. Before directly showing the relationship, we first confirmed that we observed the same trend observed by Berge *et al*, namely a positive correlation between translocation time and pulse amplitude. This relationship is shown in Fig. 4.12. The scatter data were fit with straight lines, and reveal that not only does the event amplitude increase with increasing translocation time, but that this effect decreases with increasing channel width in accordance with Eq. 4.3.

The results of the direct off-axis measurements are shown in Fig. 4.13. The left column of Fig. 4.13 shows the translocation time Δt versus the off-axis position y_c for the straight channels studied, while the right hand column shows $\Delta I/I_p$ versus y_c for the same events. The left column indicates that the translocation time strongly increases at off-axis positions closer to the channel walls, in accordance with the basic expectation of the non-slip boundary conditions.The right hand figures reveal that the amplitude $\Delta I/I_p$ increases for particles passing closer to the channel walls, in agreement with the results observed by Berge [3] and predicted by Smythe [44]. The relationship between amplitude and position is not as strong as of that between translocation time and position, but in all four channels the trend is still present. The difference between minimum and maximum $\Delta I/I_p$ from the four channels is approximately 8%. This difference, while small, is non-negligible and is in rough agreement with the level of difference found before ($\sim$ 10%). We note that measurement of the current amplitude of a single event is itself an inherently noisey process. First, the baseline must be accurately determined, which is often an ambiguous measurement, especially when dealing with noisey baseline signals. Second, the intrachannel current itself is a noisy measurement due to the noise within the signal and the fact that the current level may slightly change during translocation due to non-perfect smoothness of the PDMS channels. For instance, in Fig. 4.10, we see that the event is not perfectly flat, indicating perhaps that there is a small slope in the height of the channel. Finally, it is possible that the particles travel at different

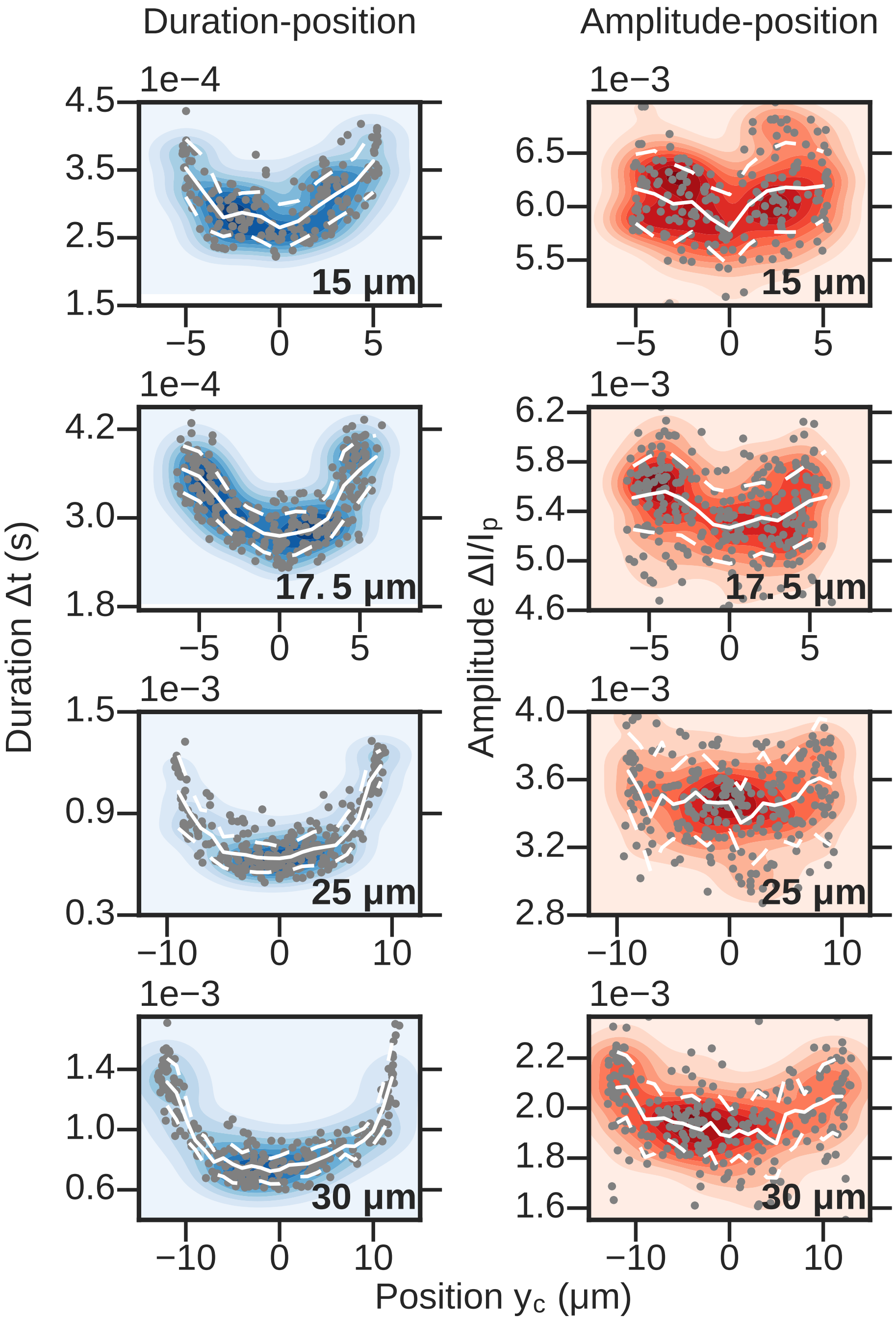

Figure 4.13: **Translocation duration Δt and RP amplitude $\Delta I/I_p$ versus lateral position y_c for four straight channels.**

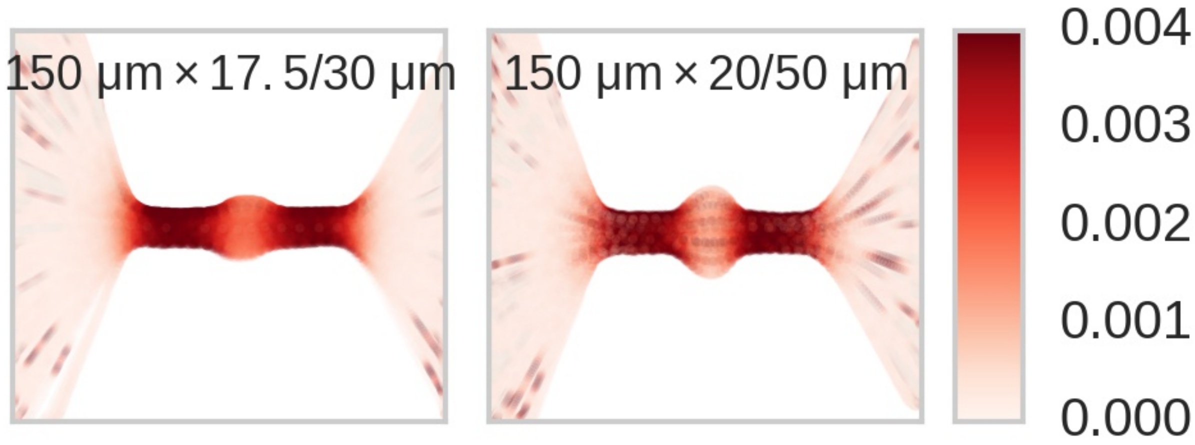

Figure 4.14: **Resistance maps of channels having a central cavity.** The resistance maps show that the resistance is most concentrated in the narrow portions of the channel and less concentrated in the central cavities (as expected from the equation $R = \rho \int dz/A\left(z\right)$).

vertical (z) positions, and this $z-$displacement would have its own lateral displacement effect. If this is the case, it would contribute a significant amount of noise to the relationship we are trying to observe. However, regardless of the noise present in the measurement, each of the channels still directly reveal the trend of off-axis translocation increasing the measured RP amplitude.

4.4.3 Channels with a central cavity

The next section covers channels that have a central cavity. The geometry of the devices is shown in the bottom of Fig. 4.6. All channels had heights of approximately $20\,\mu$m. Resistance maps are shown in Fig. 4.14. The geometry used here is somewhat artificial, and channels having central cavities are not a wide class of channels or pores used in RP studies. However, channels with non-constant widths, and even with widths that discretely changes from one value to another are not uncommon in RP applications. For instance, one of the most commonly used biological nanopores is known as $\alpha -$ hemolysin, which is characterized by having a narrow half and a wide half[1]. However, this particular geometry of

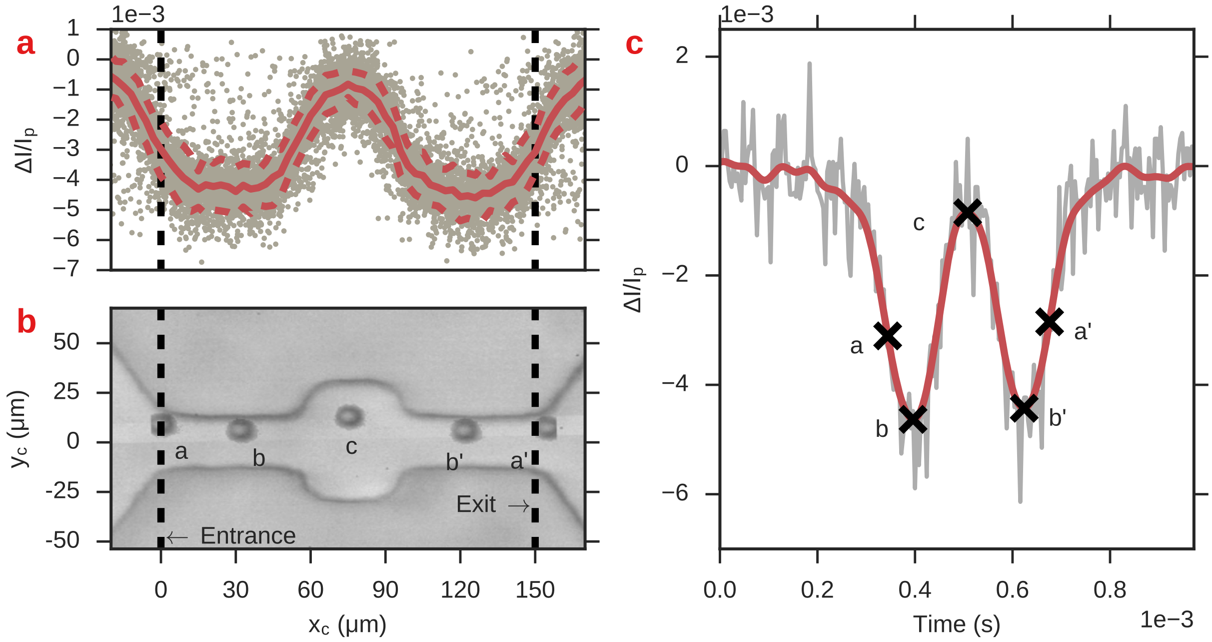

Figure 4.15: Resistive pulse amplitude $\Delta I/I_p$ versus axial position x_c (a) and versus time t (c). The camera image (**b**) shows several stills of particle positions aligned with the instantaneous RP value in the plot above (**a**).

a channel with a central cavity was recently proposed as a platform for creating positionally-dependent hydrodynamic forces that can deform particles in a controlled manner. This channel geometry was promoted as a means of probing the deformability of single human cells, a topic that will be discussed in the next chapter of this dissertation. In the rest of this section, we discuss the distribution of resistance in the channel as determined by the resistance maps, as well as the effects of off-axis translocation of particles. In particular, we find an interesting relationship between off-axis position and pulse amplitude that behaves oppositely to what was found in the previous section on straight channels.

Resistive pulse amplitude in the wide and narrow portions of the channels

Basic physics considerations suggest that the resistance should be more concentrated in the narrow portions of the channel than in the central cavity, and therefore that the RP amplitudes should be larger in the narrow portions as well. This simple feature of the system is confirmed by the shapes of the individual resistive pulses; an example can be found in Fig. 4.15c.

However, a more quantitative description of the distribution of the local resistance in the channel is found in the following equation[8]

$$\Delta R = \frac{4\rho d^3}{\pi D^4}\left[1 - 0.8\left(\frac{d}{D}\right)^3\right]^{-1}. \tag{4.4}$$

Since our experiment measures the current rather than the channel resistance, we can use our experimental data to verify Eq. 4.4 by observing that $\Delta R/R_0 = \Delta I/I_p$, and therefore

$$\frac{\Delta I/I_p|_{x_c=x_{c1}}}{\Delta I/I_p|_{x_c=x_{c2}}} = \frac{\Delta R/R_0|_{x_c=x_{c1}}}{\Delta R/R_0|_{x_c=x_{c2}}} = \frac{\Delta R|_{x_c=x_{c1}}}{\Delta R|_{x_c=x_{c2}}}. \tag{4.5}$$

Equation 4.4 can be substituted into the final expression in 4.5, and therefore the equation enables a means of comparing the experimentally obtained values for $\Delta I/I_p$ with the theoretical equations. This operation was performed for each of the channels with central cavities, with x_{c1} corresponding to the particle occupying the narrow portion of the channel, and x_{c2} corresponding to the particle occupying the exact middle of the cavitated part of the channel. The results are shown in Fig. 4.16. The histograms indicate the distribution of the experimentally measured ratios, while the dashed lines represent the theoretical predictions of equation 4.5. The spread in each distribution is a combination of measurement error on the exact values of the current, an intrinsic (although small) spread in the distribution of sizes of the particles, and perhaps most importantly, the distribution of off-axis positions

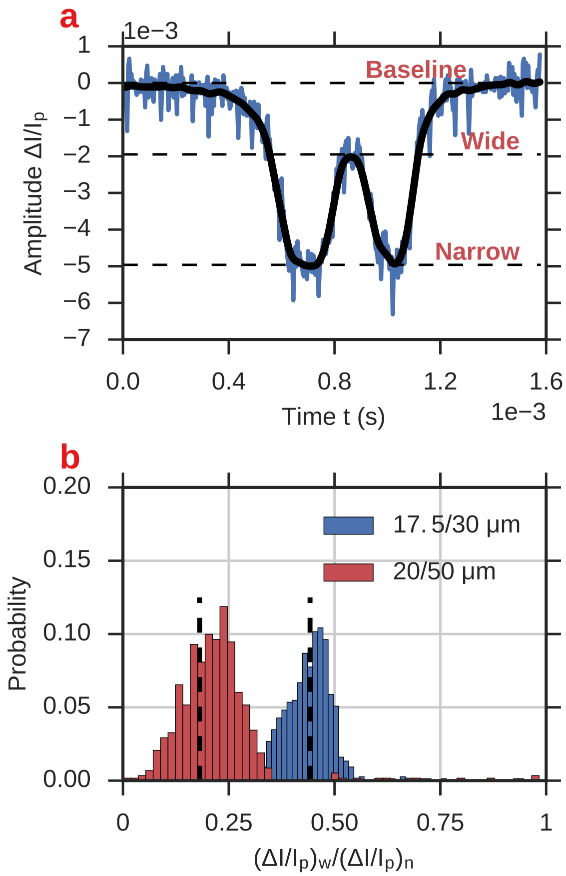

Figure 4.16: **Histograms of the ratios of the pulse amplitude $\Delta I/I_p$ in the narrow portion of the channel and in the central cavity for the two types of cavitated channels studied.** The dashed lines indicate the theoretical values predicted by Eq. 4.5. In both cases, the theoretical predictions closely match the experimentally obtained results.

y_c, which we showed significantly contributed to the measured $\Delta I/I_p$ in the previous section, and which we will further discuss in the next section. While the dashed lines overlap well with the actual distributions, we note that there is a small discrepancy in both cases. Equation 4.5 was derived for spheres moving through cylindrical channels only, and so we expect that our channels, which have rectangular cross-sections, may not adhere perfectly. In using Eq. 4.5, we approximated our channels as cylinders having radii that would yield a cross-sectional area the same as the actual cross-sectional area of the rectangular channels. This approximation will be more accurate for low-aspect ratio cross sections (i.e. squares), and less-so for larger aspect ratio channels. This observation agrees with our findings: the $20-50-20\mu$m channel has a larger aspect ratio in its cavity, and also happens to have a greater discrepancy between the experimental results and the theoretical predictions of Eq. 4.5.

Dependence of resistive pulse amplitude on lateral displacement in narrow and wide (cavity) regions

In the section on straight channels, we looked at the dependence of lateral displacement on the measured current amplitude $\Delta I/I_p$. In this section, we would like to explore the same relationship but this time for the narrow constrictions and central cavity separately. Retracing our footsteps, Fig. 4.17 shows the resistive pulse amplitudes $\Delta I/I_p$ versus translocation time Δt for particles passing through the channels, but this time including both the pulse amplitude in the central cavity in addition to its value in the narrow constrictions. Interestingly, while the positive correlation observed previously is still present in the narrow constriction, we observe a negative correlation between translocation time and pulse amplitude for particles in the cavity. This result suggests that events with longer translocation times, presumably still those translocating close to the walls, will have larger pulse amplitudes in the narrow constriction but smaller pulse amplitudes in the cavities compared to

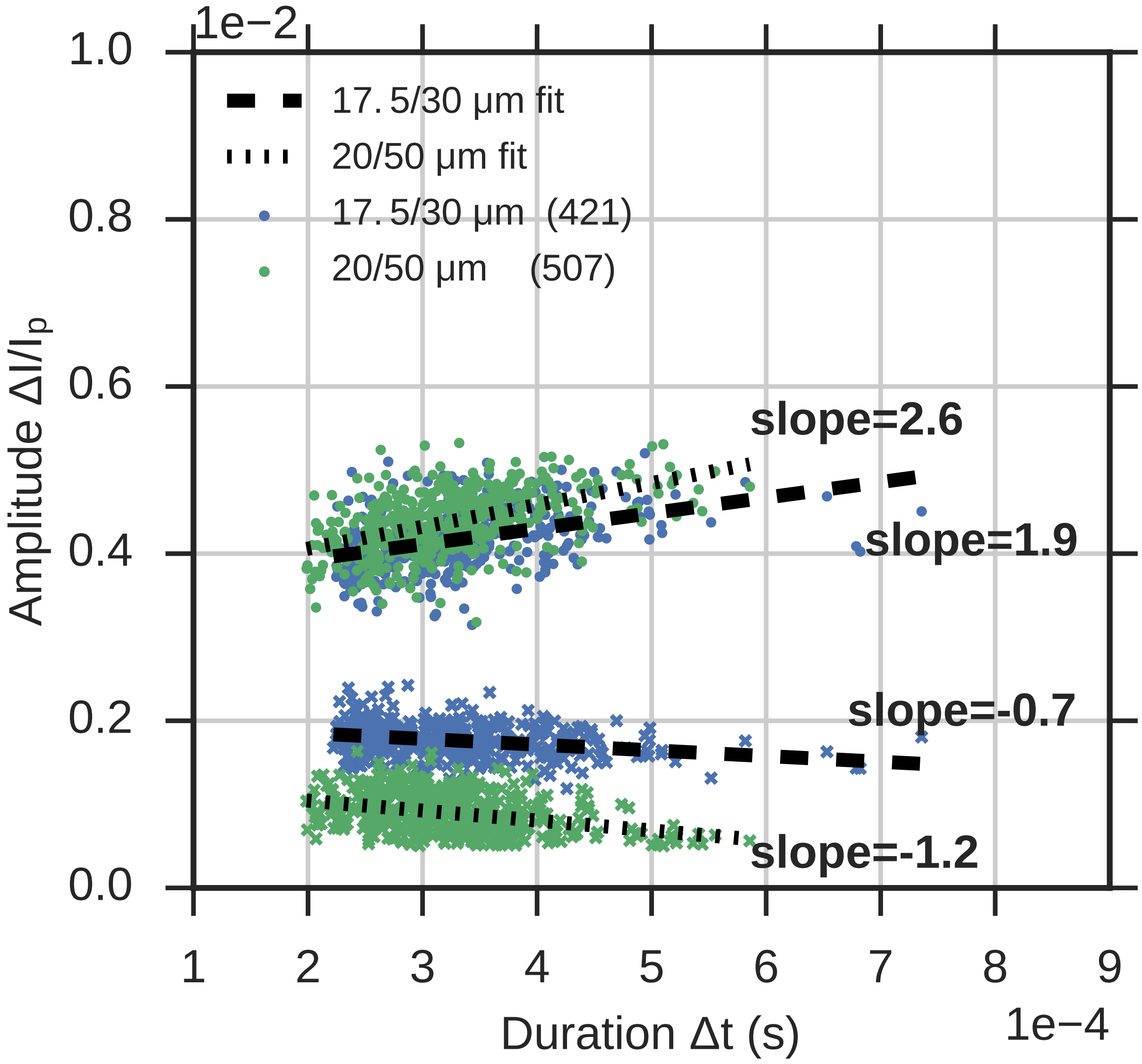

Figure 4.17: **Pulse amplitude $\Delta I/I_p$ in the narrow portion and central cavity versus translocation time Δt for particles passing through the cavitated channels.** The plots reveal a positive correlation between translocation time and pulse amplitude in the narrow portion of the channel, but a negative correlation between translocation time and pulse amplitude measured in the central cavity.

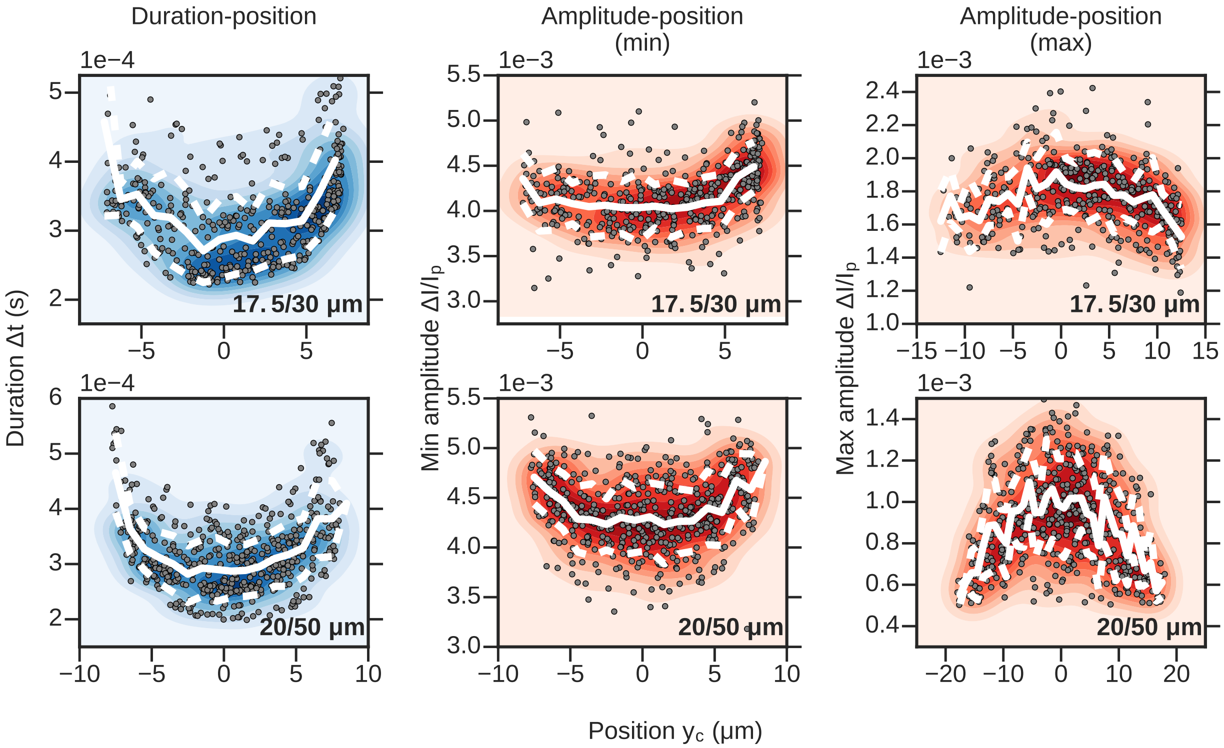

Figure 4.18: **Translocation duration, pulse amplitude in the narrow constriction, and pulse amplitude in the central cavity versus off-axis position for the two channels with central cavities studed in this work.** Straight lines were fit to each distribution. The fits indicate a positive correlation between event amplitude and duration in the narrow constriction, and a negative correlation in the central cavity.

on-axis translocating particles.

In order to directly confirm the connection between off-axis position y_c and pulse amplitude $\Delta I/I_p$, we measured the two values instanteously and plotted the results. Figure 4.18 is analagous to Fig. 4.13, but includes positions when the particle is in the narrow portion of the channel and when it occupies the central cavity. Starting with the left column of the figure, we see that particles that translocated near the wall of the cavity had longer translocation times, in accordance with our expectations from Poiseuille flow profiles. In the case of particles having a central cavity, the fluid flow profiles are undoubtedly more complex than a simple Poiseuille flow; however, we expect that the general trend of a central maximum in the fluid velocity and zero fluid velocity at the channel walls will still hold. The next column shows the relationship between amplitude and lateral position in the narrow part of the channel. Not surprisingly, the plots show an increase in the current amplitude when particles translocate closer to the walls, in accordance with our findings for completely straight channels. Finally, in the third column we plot current pulse amplitude versus off-axis position while the particle occupies the central cavity. First, notice that the spread in y_c is greater than in the cavity. This greater spread reflects the fact that particles translocating close to the wall follow the contours of the channel, and can swing into the cavity during their translocation, having greater off-axis positions than is possible in the narrow portion. The plot reveals a striking difference between the off-axis effect in the narrow and in the wide portions. Instead of increasing the current amplitude, off-axis translocation greatly decreases the current amplitude in the cavity. Furthermore, the decrease in the current amplitude is upwards of 40%, a much greater difference than the maximum of $\sim$ 10% observed for the excess of the current amplitude due to off axis translocation in the narrow portion of the channel. This result has great implications for any RP studies using channels with cavities and or channels with varying widths. To give specific examples, polyethylene terephthalate pores (discussed in 3) have natural undulations in their interior diameter that can have cavity-like features. In the next chapter we discuss how the microfluidic channels discussed here may be used with RP to measure the deformability of cells; in this case, the off-axis translocation effect will be especially significant.

4.5 Conclusion

In this chapter we introduced a hybrid resistive-pulse optical measurement detection platform. The platform may be used to enhance the characterization of single particles by providing new information (features) of their passage. Perhaps most importantly, the platform can be used to validate RP measurements, which are prone to distortion caused by effects related to geometry and position that cannot be verified through the RP signal alone. Therefore, we suggest the greatest use of this hybrid measurement system will be in validating the measurements of specific RP platforms.

However, we must point out that the experiments conducted here are necessarily at the microscale, since, as discussed earlier, optical imaging is only possible above the diffraction limit of 200 nm. Furthermore, we argued earlier that RP experiments are most widely employed to study particles below the optical diffraction limit. Therefore, at first glance it appears that the results presented here are of no use to most RP experiments. However, the positional effects that distort RP measurements are size independent. To understand why, note that the size effects all originate due to the distortion of the electric field along the boundaries present in the system. In the continuum approximation, the electric field lines are scale invariant–they only depend on the particular relative geometry of the system. As a concrete example, a 10 μnm sphere inside a 20 μm cylindrical channel will experience the same positional effects as a 10 nm sphere inside a 20 nm cylindrical channel. That is, the overall *scale* of the physics involved is insignificant; Only the relative sizes of the entities imposing the electrostatic boundary conditions matters. Therefore, we expect that the effects studied in this paper generalize down to the sub-micro scale and beyond. However, we can only claim the physics pertaining to the electrostatics of the problem generalize down to the nanoscale. At the nanoscale, a wealth of new physics presents itself, including electrostatic screening at charged surfaces, electroosmosis, and electrophoresis[25, 40]. Therefore, we do not suggest that this paper's results are directly translatable down to the nanoscale, but rather that the results superimpose with the physics native to the nanoscale. Nevertheless, we believe that the results in this work can serve as useful considerations for understanding RP experiments in nanoscale systems, and the general principle of simultaneous RP and IM can be applied to study other important aspects of RP experiments not covered in this work.

Chapter 5

Resistive pulse studies of cancer cell deformability

5.1 Background & Theory

One of the most important applications in microfluidic technology today is the study of cell populations. One tool for studying cell properties is the flow cytometer, invented in 1965 by Fulwyler [14]. Flow cytometers are a mixture of many individual microfluidic elements combined in series, each with its own function. On the sensing side, flow cytometry makes use of measured scattering of laser light as well as detection of fluorescence signals. Dyes are specifically attached to certain types of antibodies, which then may interact with the cell membranes in the suspension. When the cells are pulsed by lasers in the laser light, the dyes are stimulated to emit their own characteristic fluorescent wavelength, which can be measured to determine which antibodies have interacted with the cell. This type of information is incredibly valuable in determining phenotypic and classification information for the cells. Furthermore, the information garnered from real-time cytometry information can be used to sort cells in real time, in a system known as fluorescence activated cell sorting system (FACS). Cell cytometry is the workhorse of modern day molecular and cellular biology studies, but suffers from the fact that it is a label-dependent method due to the introduction of the dyes. Such labels can adversely affect the the cells' viability that prevents them from being used in a post-interrogation analysis, even after being separated by a system like FACS. Additionally, flow cytometry requires the use of costly fluorescent reagents and skilled technicians that must be present to perform the measurement and to ensure proper calibration of the fluorescence signal *via* the use of fluorescent beads [16].

While flow cytometry focuses on the measurement of cells *via* light scattering and the cells' interaction with specific chemicals, another dimension often not thought of is the cells' mechanical properties, such as their size, shape, and deformability[28]. Size is an obvious discriminating feature between different types of cells, but recently scientists have looked to mechanical stiffness as another useful mechanical phenotype[47]. Cell stiffness, which derives primarily from the cytoskeleton and membrane properties, has been shown to vary from cell to cell, and even between various stages in cells' mitotic cycles[11, 13]. As a concrete example, cancer cells are generally thought to be 'squishier' than non-cancerous cells[58]. For these reasons, developing a method of probing the mechanical stiffness of cells is highly desirable for cell characterization applications, and could serve as a complementary cell phenotyping platform to deformability cytometry.

In order to measure the stiffness of an object, it must be subjected to constrained forces and its response measured. Probably the most straight forward way of exerting a deformation-inducing force is by directly pushing on it, for example by using an atomic force microscopy (AFM) probe. Using AFM, the cell is pushed with a cantilever which simultaneously measures the responsive force, which is related to the Young's modulus of the cell if it is treated as an elastically deformable object. Other similar methods exist, and while they are very accurate and easily interpretable, they suffer from an excruciatingly slow throughput. For instance, using AFM for cell deformation measurement can take a few minutes per cell. For most cell applications a high throughput is necessary, and therefore these applications are not feasible for discovering cell population statistics[28].

Microfluidic platforms constitute a different strategy for inducing and measuring cell deformation. Cells passing quickly through narrow constrictions are subjected to large, anisotropic hydrodynamic forces which can induce a measurable particle deformation. The advantage of this type of method is its extremely large throughput; rather than spending several minutes per particle as in measurements conducted with AFM, thousands of cells per second can be measured in microfluidic platforms. Even within the narrow field of microfluidic-based deformability cytometry, there are multiple types of platforms. Probably the most conceptually simple is a standard microfluidic channel that tightly confines cells passing through it. Due to anisotropies in the hydrodynamic stresses and strains around the particle, it will deform even in a uniformly shaped channel [34, 32].

In traditional microfluidic methods of measuring cell deformability, direct imaging is used to determine the cell shape across different frames in the video, which corresponds to the hydrodynamic load it is under. However, deforming cells in microfluidic channels requires enormous flow rates (a perk in terms of the desirability for high-throughput), and therefore requires immensely fast imaging. This requirement necessitates the use of a high-speed camera used in conjunction with an optical microscope, usually shooting with exposures around $1\,\mu$m. When combined with an optical microscope, such high-speed cameras are capable of capturing cell deformations with high spatial and temporal resolution, and are even capable of resolving the cells' deformation dynamics [28]. Currently high-speed camera imaging is by far the most popular method of capturing cell deformations, but it comes with two serious disadvantages. First, the camera itself adds a large cost to the experimental apparatus, and will likely dwarf the price of any other component in the deformability cytometer. Second, imaging data is inherently highly multidimensional and computationally expensive to analyze. As a result, online analyses conducted during the run of the experiment are usually not possible at ultra high throughputs. The current state-of-the-art in high throughput online analysis (that this author is aware of) is $\sim 100\,\text{cells/second}$, which as far as microfluidic-based methods go is quite slow[34, 32]. While the data can still be stored, processed, and analyzed later, offline analysis does not allow for real-time separation, one of the most highly desirable applications of deformability cytometry.

Instead of using camera imaging, one can instead imagine trying to employ resistive pulse (RP) to measure the deformability of particles. The immediate advantage is a significant reduction in the data bandwidth compared to imaging; while a high-speed camera may generate 1 GB/second, a conservative estimate, RP sensing may generate only 1 MB/second, three orders of magnitude less data. Furthermore, image processing methods are generally more computationally cumbersome than 1D time series analysis.

While it is apparent that resistive pulse is computationally cheaper than imaging analysis, it is most important to demonstrate that deformability can actually be measured via RP sensing. In chapter 3, we discussed the equations for the resistive pulse amplitudes of ellipsoidal objects. For cells that are spheroidal in their unloaded state, ellipsoids are reasonable geometries to expect for the deformation shape in the loaded state, at least as an approximation. If we consider a straight ion conducting channel with an ellipsoidal particle inside it, the aspect ratio and orientation of the particle greatly affects the ionic resistance of the system. Under the assumption that the particles take on ellipsoidal geometries, the shapes will be described as being prolate, oblate, or spherical with respect to the channel's axis. Prolate geometries correspond to an extension of the particle along the channel's axis, while oblate geometries correspond to an axial compression. The difference in the measured

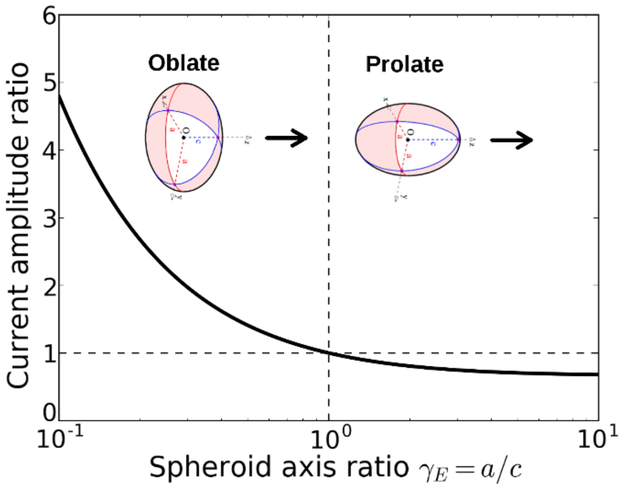

Figure 5.1: **Resistive pulse amplitude $\Delta I/I_p$ for equal volume spheroidal objects relative to a sphere.** The polar axis of the particle is aligned with the channel's axis, so that oblate geometries correspond to motion along the channel axis. The values come from equation 5.1 when the correct shape factor $f_{\|}$ is applied.

resistive pulse amplitude of these particles is given by the following equation:

$$\frac{\Delta I}{I_p} = f_{\|}\frac{v}{V}, \tag{5.1}$$

where v and V are the volume of the particle and channel, respectively, and $f_{\|}$ is a constant known as the 'shape-factor', which depends on the aspect ratio of the ellipsoid.

For spheres, $f_{\|} = 1$, and for prolate and oblate spheroids, $f_{\|} < 1$ and $f_{parallel} > 1$, respectively. Figure 3.2 shows plots of the RP amplitude $\Delta I/I_p$ for ellipsoids of the same volume but different aspect ratios, relative to a sphere. The plot reveals that even for modest deformations, for instance a stretching ratio of 2/3, a mildly oblate ellipsoid, the increase in $\Delta I/I$ is nearly 30%. Similarly, the current $\Delta I/I$ changes for prolate geometries, although to a lesser degree[15].

As mentioned previously, there are many possible types of high-throughput microfluidic

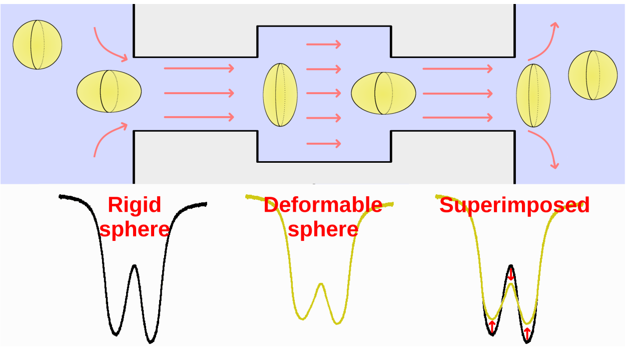

Figure 5.2: **Scheme of the cavitated channel, the pattern of cell deformations it induces, and expected resistive pulse signals of rigid and deformable spheres passing through it.** As the cell passes through the channel, it undergoes a series of shape configuration changes according to the sequence $s \rightarrow p \rightarrow o \rightarrow p \rightarrow s$, where s, p, and o are for spherical, prolate, and oblate respectively. The prolate and oblate geometries have lower and greater resistive pulse amplitudes compared to spheres, respectively, and according to the deformation model described the resistive pulses should deform so that the local minima and maxima are closer in value.

systems than can induce cell deformations. We devised a method that has been shown to be capable of inducing bidirectional deformations (prolate and oblate). The scheme of the channel design along with the model for the cell deformations it induces is shown in Fig 5.2. The key to understanding the channel geometry is to understand the primary hydrodynamic forces that work on a cell and deform it in extensional, i.e., accelerating and decelerating flows. When a cell transitions from a region of high local fluid velocity to low local fluid velocity, there is a greater magnitude of normal stress forces on the back of the particle than on the front. Consequently, the particle is axially compressed into a oblate configuration. Oppositely, when the particle makes the transition from a slow to fast region, the net forces pulling the particle forward are greater than the forces pushing it from behind, elongating it in its direction of motion. This corresponds to the prolate shape configuration. According to this model, one can induce bidirectional shape changes in passing particles by having transitions between regions of slow and fast local fluid flow, and vice versa. This criterion allows for multiple possibilities, but the geometry chosen for our system is described by a channel having a central cavity[60], but otherwise with a straight cross-section. As the cell enters the microchannel, it accelerates and is pulled in, and in the process deforms into a prolate shape. When the cell arrives at the central cavity, the fluid flow is slower and the particle decelerates, becoming oblate. At the end of the cavity, the particle again undergoes an acceleration and deforms back into its prolate shape. Therefore, the cell undergoes the following shape configuration changes as it traverses through the channel:

spherical → prolate → oblate → prolate → spherical.

We seek to find the aspect ratio of the approximate ellipses a/b at various points in the channel. The aspect ratio will remain the same at all points for completely non-deforming particles, but will vary according to the above model for deforming particles, and to a greater degree for the most deformable particles. For the scheme shown in Fig. 5.2, the expected aspect ratio a/b as a function of the axial position adheres to the pattern shown above. The observables of interest might be the minimum and maximum aspect ratios, or perhaps the ratio of the minimum and maximum aspect ratios which would reflect the general elasticity properties of the cells. These are easily obtained directly with the imaging data. However, in the RP signal we measure these observables indirectly, by relating the expected shape of a deformable particle with the actual observed RP signal. Figure 5.2 (bottom) shows the expected transformation of the RP signal under the deformation motif for the cavitated channels. In the narrow regions where a prolate elongation occurs the current amplitude $\Delta I/I_p$ is *decreased*, while in the central cavity where the particle assumes its oblate configuration the amplitude is *increased*. Therefore, in the RP signal the observable of interest might be the ratio of the maximum in the signal (minimum $\Delta I/I_p$) and either of the two minima in the signal (maximum $\Delta I/I_p$), which would be a proxy measurement for the ratios of the aspect ratios calculated directly from imaging data.

5.2 Experiment and data analysis

In order to test the concept of cell deformability cytometry with the channel geometry described above and using RP, we ran microfluidic experiments with cancer cells. The hybrid RP-IM method (described in chapter 4) is employed in order to directly confirm the deformability of the particles as well as to relate the shape changes with the RP signal. In the following sections we describe the experiment's hardware set up, the channel geometries and cell samples used in these experiments, and the data analysis steps that are undertaken. To date, the experiments performed have primarily been focused on analyzing the optical data in the experiments, since measuring their deformability optically is a prerequisite for determining it via the RP signal.

5.2.1 Hardware

The hardware used here is similar to the hardware used in the RP-IM hybrid experiments performed in chapter 4; in particular, a high-speed camera is again employed. The most notable difference is the inclusion of a high luminosity LED. By pulsing the LED at extremely fast rates, the camera's exposure time is effectively reduced, enabling higher time resolution and less blurring of the cells. The F-Sync of the high-speed camera connects to a signal generator *via* a BNC cable, which is programmed to emit a signal each time the camera signals an exposure. By connecting the signal generator to the LED light's control card, the LED can be made to strobe every time the camera takes an exposure, with the strobe time fixed by the output of the signal generator. In most cases, a 500 ns pulse was used, which effectively reduces the camera's exposure time to that time interval.

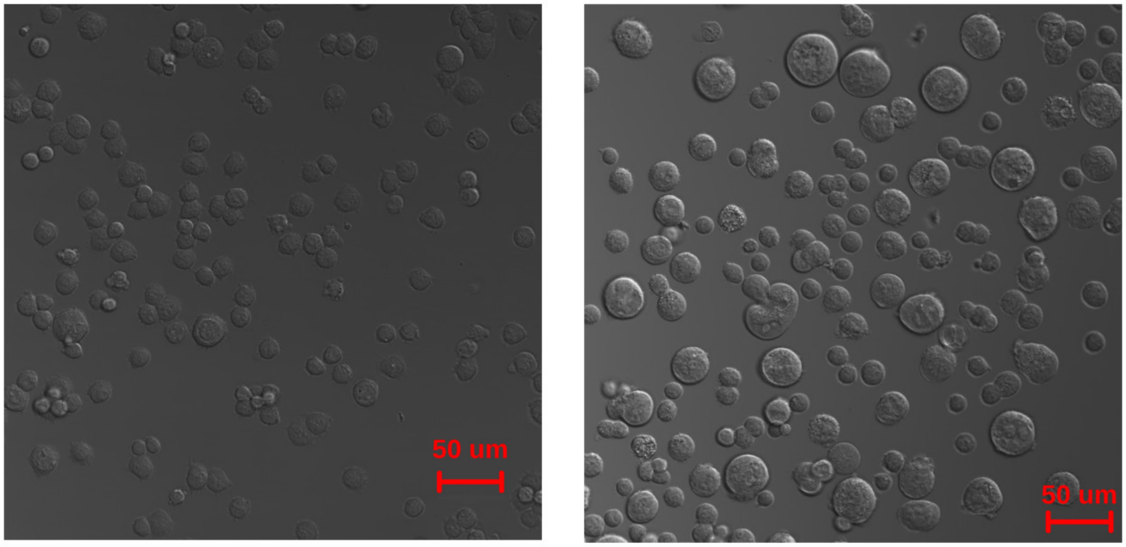

293-T HCT-116

Figure 5.3: **Confocal images of HCT-116 (left) and 293-T (right) cells used in this study.** The HCT-116 cells were chosen for their large deformability; the 293-T cells had unknown deformability properties.

5.2.2 Cells and channels

Two cell lines were specifically selected by collaborators to be used for these experiments. The first, 293-T, an embryonic kidney cell, was selected because it was known to fall into the appropriate size range while having unknown deformability properties. The second cell line chosen was HCT-116, a colorectal cancer cell that is known to be highly deformable. Figure 5.3 shows confocal images of these two types of cells. The cells were suspended in HBSS, a biocompatible buffer with high conductivity. Additionally, the suspension was spiked with 0.5% by weight methylcellulose, a thickening agent that increases the viscosity of the solution and can promote deformation[34]. Lastly, pluronic, a biocompatible surfactant, is added at 0.1% concentration by volume. The final cell suspension had concentration between $0.5 - 1 \times 10^6$ cells/mL.

All of the channels studied had the cavitated design. The most important dimension is the narrow constriction width, which must be just larger than the cells in order to exert large hydrodynamic forces. However, if the channels are too large the cells will sterically deform as they press against the channel walls, which is undesirable due to the complexity it introduces in the analysis of cell deformability. For this reason, channel openings were chosen to be $15\,\mu$m, which provided a tight environment for the cells while allowing most of them to pass through without having to squeeze through the channels. The central cavity was chosen to always have twice the width of the narrow constriction.

5.2.3 Experiment protocol

The cell suspension is drawn into a syringe, which is then mounted to a syringe pump. Tubing is connected from the syringe to the inlet port of the active channel, and another tube is connected to the outlet port, which drains into a collection reservoir. The solution is pushed through the syringe at a fast rate until it enters the channel. Initial experiments were conducted at relatively slow flow rates, around $0.005 - 0.015$ mL/min, however these rates were increased to as high as 0.2 mL/min when analysis of the cells revealed little deformation. When the fluid reaches the electrode at the exit port, the circuit is completed and the ionic current is induced. At this point the data is recorded. While the recording itself is very fast, the data must be transferred to the control computer in order for it to be stored; the onboard camera memory is only sufficient to hold the data of a single recording. The transfer and saving process takes nearly 15 minutes, and over this duration of time the vast majority of cells sediment to the bottom of the tubing and syringe. For this reason, in between data transfers we remove the tubing and syringe and clean them. After recording, the solution is gently mixed to resuspend the cells, and the process of pushing the solution, refocusing the microscope, and recording is repeated. Experiments are repeated in this way for different cell lines, channel geometries, and fluid flow rates. Following the experiments, data is immediatley backed up redundantly to external storage drives where it remains until it is ready for post processing and analysis.

5.2.4 Data analysis

While this device is being characterized and developed, the most important data stream to focus on is the imaging data. The primary observable of interest in this experiment is the shape of the particle. There is no single way of defining the shape of an object, but because we are interested in comparing the RP signals of cells with the theoretical RP amplitudes of ellipses, we determine the shape of the cell by fitting ellipses to its borders across multiple frames. Thus, the objective in demonstrating deformation optically is to fit ellipses with semi-major axis a and semi-minor axis b to cells across multiple frames and track their change in aspect ratio as they pass through the channel. According to the above model, the cells should oscillate between prolate, oblate, and spherical shapes at various points in the channel, and therefore we expect to observe an oscillation of the determined aspect ratio $\gamma = a/b$ between values > 1 and values < 1. The exact shape of the cell is never exactly ellipsoidal, however we find that for most shape configurations it is an adequate approximation.

While the ellipses could be fit manually by determining their width and height in each frame, the number of cells observed—usually ~ 1000 per recording—prohibits this manual measurement. Instead, we devise an image processing pipeline that starts with the raw camera data and results in a calculation of the ellipse fits for every single detection and every single particle passing through the channel. The pipeline works as follows. First, cells are detected in individual frames via a template subtraction method. Then, cells are tracked across frames using a minimum distance approach. These two methods are described in greater detail in chapter 4.

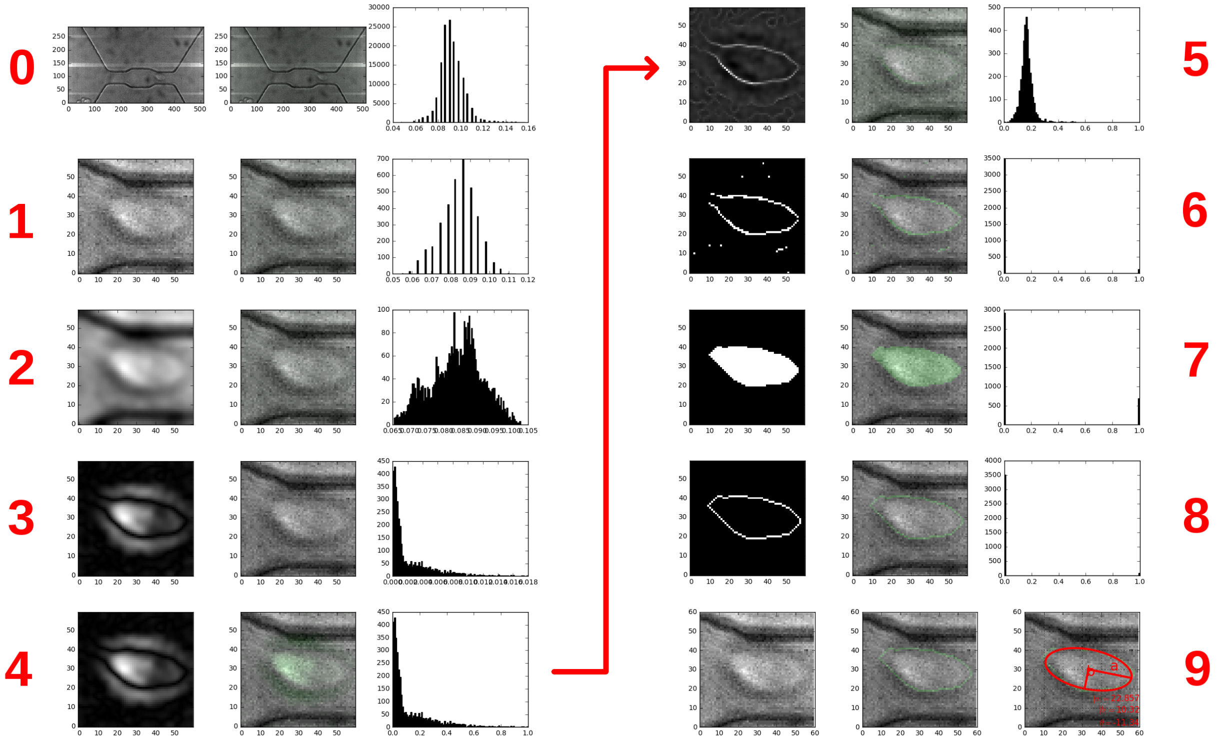

Figure 5.4: **Example ellipse fitting protocol for a single detection within a single event.** The left column of each row shows the current image transformation. The central column shows the raw frame with the pixels shaded green with intensity according to the intensity of the pixels in the transformed image. The right column shows pixel intensity in the processed image. **1:** Raw image. **2:** Image is cropped in the vicinity of the particle. **3:** Template image is subtracted off. **4:** Pixel intensity is rescaled. **5:** Laplacian derivative. **6:** Pixel intensity thresholding. Notice the histogram becomes binary distributed. **7:** Morphological closing of image. **8:** Image is dilated and subtracted from undilated image, leaving a thin shell around the border of the cell. **9:** Ellipse is fit to the cell's border.

After a list of events is determined, ellipses need to be fit to the image of the cell in each frame. A number of preprocessing steps is required to transform the image to a form where this ellipse fitting is possible. One possible ellipse fitting protocol is shown in Fig. 5.4. All processing protocols must reduce the image down to a binary form where the only pixels highlighted are the pixels on the exact boundary of the cell. Operations common to most processing protocols are template subtraction, Gaussian blurring, Laplace derivative transformation, thresholding, and morphological operations such as binary dilation, erosion, and closing. Many of these steps have their own parameters associated with them, and so it is useful to test each of the processing steps and the parameters, plotting the image transformation along the way.

Once the ideal parameters are determined, ellipses are fit to each detection in each cell translocation event. The end result is shown in Fig. 5.4, row 9. Fitting an ellipse to the particle in each frame is useful because many properties of the particle and its translocation can be determined via the ellipse fits. For instance, ellipse fitting yields accurate determination of the central position of the particle, which can be used to accurately determine its trajectory and velocity. Furthermore, once the ellipse is obtained for every frame it is easy to calculate the aspect ratio of the particle during the course of its trajectory and compare with the expectations of the model proposed earlier (Fig. 5.2). The ellipse is fit using a minimization approach, where the ellipse that fits the detected edge pixels best according to a least-squares metric is chosen.

After the ellipses are detected, a number of filtering steps must be enacted to remove undesirable events, including clusters of cells stuck together, cells that are either too large or too small, or cells that pass through the channel with too much lateral displacement. In total, we filter events based on successful detection of their entire trajectory, maximum and minimum radius, maximum and minimum aspect ratio, and maximum displacement from the channel axis. For instance, a particle with aspect ratio too large might correspond to

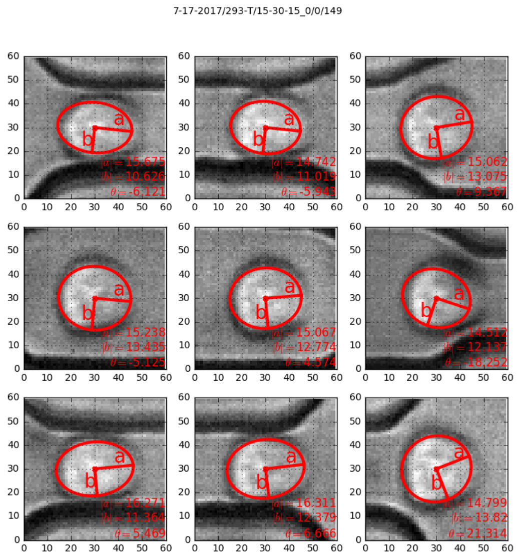

Figure 5.5: **Ellipse fits for a 293-T cell passing through a $15-30-15\mu$m channel at various positions.** Notice that in the narrow portions of the channel the particle assumes a prolate (axially-elongated) shape, while in the central cavity it assumes an oblate (laterally-elongated) shape, in agreement with the motif presented in Fig. 5.2
.

two cells stuck together, with an overall shape more closely resembling a rod than a sphere.

Finally, we have a list of events that have not been filtered out. For these events we calculate various observables based on their ellipses, including their aspect ratio at all points in the channel, their net velocity through the channel, and radius.

5.3 Results & Discussion

The most important question to be answered in the experiments is whether the cells actually deform according to the model proposed. In order to answer this question, we examined specific events to look at their change in aspect ratio as they pass through the channel. Many events consistently show a deformation pattern that subscribes to the model, as shown in Fig. 5.5. On the other hand, there were many events that showed modest to little deformation.

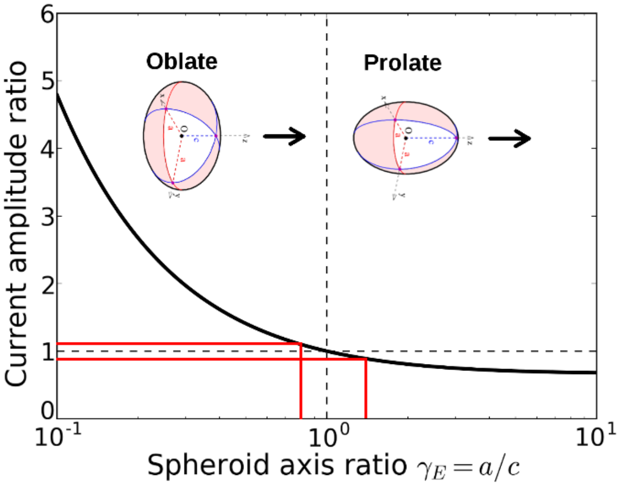

Figure 5.6: **Change in amplitude of ellipsoids relative to spheres, with theoretical predicted difference based on** the maximum deformations we observed in the experiments.

However, this result is not unreasonable; our model does not suggest that all cells must deform, and indeed there may be cells that are quite resilient to deformations, or cases where the hydrodynamic forces were insufficient to generate significant deformation. However, we never observe a trend opposite to the deformation mode posited, i.e. an oblate-to-prolate transition rather than a prolate-to-oblate transition. This observation suggests that, while the magnitude of the effect may be low in some cases, the effect still occurs.

While the deformation motif has been confirmed, the question remains whether the deformation will be observable in the resistive pulse data. As of the time of this writing, no confirmation has been obtained yet. The reason for this is that the high-speed LED introduced in order to increase the time resolution introduced a sizeable noise component to the resistive pulse signal, which prohibits accurate detection of the resistive pulse signal. At the moment, we cannot claim that the deformations have been observed with resistive pulse alone. However, we can *predict* whether such deformations will be evident in the resistive pulse signal by looking at the maximum and minimum aspect ratios the cells attain during their translocation through the channel, and to compare it with the expected resistive pulse amplitude due to the shape change, shown in Fig. 3.2. Current estimates of the maximum deformation observed in the video correspond to ellipses of aspect ratios $a/b = 0.8$ and $a/b = 1.2$. Figure 5.6 shows the expected amplitude changes from the shape change for this magnitude of deformations. We estimate that the difference should be $1.1 - 0.9$, a difference of approximately 20%. If the difference is this large, then the difference should be observable in the resistive pulse baseline when noise improvements are made.

5.4 Conclusion

In this chapter we discussed the importance of measuring the mechanical properties of cells, and introduced microfluidics as a means of inducing measurable deformations of cells. Furthermore, we proposed that resistive pulse sensing can be used to measure the deformations instead of imaging, which will lead to cheaper detection platforms, enable real-time analysis of the cells, and increase the maximum throughput of the detections. We proposed a channel design characterized with a single central cavity that might induce bilateral deformations in cells. We performed experiments with the hybrid resistive pulse-optical imaging set up described in chapter 4 on two different cell lines. While the resistive pulse data is still inconclusive, the imaging data revealed overwhelming evidence for the types of deformations we expected according to the model we developed. While much work remains to be done on this project, we believe its continuation will yield fruitful results, and possibly lead to an all new impedance-based deformability cytometer that is capable of characterizing up to thousands of cells per second.

Chapter 6

Conclusion

In this dissertation I discussed several projects I worked on as part of my PhD work. In the first project, we described experiments conducted with hybrid insulator-conductor nanopores, where the primary motivation was in understanding the conductance properties of the pore itself. The following three chapters describe resistive pulse experiments, which involve studying how the change in conductance of channels can be used to determine the properties of particles passing through them.

In the next few sections, we'll quickly summarize each of the sections of this thesis.

6.1 Introduction

In the introduction we reviewed all of the requisite knowledge for understanding each of the projects in the body of this thesis. Each of these projects ultimately involves ion transport in conducting channels. The physics involved includes electrostatics, statistical mechanics, and fluid mechanics. More specifically, we discussed the Nernst-Planck equations that describe the motions of ions in an electric field and moving fluid medium. We also discussed the motion of the fluid medium itself, described by the famous Navier-Stokes equations. In order to understand the nanoscale effects that give nanopores their interesting conductance properties, we introduced the Poisson-Boltzmann equation, which predicts the formation of the electrical double layer, a small screening layer of counterions present within a small distance of any charged surface in a solution. Some of the consequences of the formation of the electrical double layer were discussed, including surface conductance, electroosmosis, and electrophoresis. The sections on the electrical double layer primarily pertain to the topics of chapters 2 and 3, which were at the nanoscale. Finally, we introduced the application and theory of resistive pulse sensing, the primary topic of this dissertation.

6.2 Ion conductance of nanopores

6.2.1 Ion conductance of hybrid insulating-conducting nanopores

The vast majority of nanopores studied are entirely insulating. However, it is conceivable that one could use metallic (conducting) nanopores instead. As far as electrostatics is concerned, the difference between insulating and conducting bodies is in the electrostatic boundary conditions imposed at their surfaces; in metals, the external applied voltage gradients must be cancelled to ensure no electric fields are present in the body of the conductor. The net result is that free charges in the metal must rearrange themselves in order to cancel the field, and in doing so situate themselves at the surface of the metal. These charge act like any other present charge in the system, including the static surface charges that are present due to the native surface chemistry on insulating surfaces. We developed a hybrid insulator-metallic system by depositing a thin layer of gold on top of a silicon nitride membrane, and drilling through it to create a nanopore. We studied the nanopores' properties by measuring their current-voltage characteristics, and found that the systems behave as rectifying diodes, with large conductances for one voltage polarity and near-zero conductances at the opposite voltage polarity. Furthermore, we found that the direction of the rectification could not be explained by static charges present on the surface of the silicon nitride. With the aid of COMSOL simulations, we showed that the rectification could be explained if free charges in the metal strongly polarized the surface in response to the external voltages. In the 'on' state (high conductance state), the total charge configuration led to enhanced ion sourcing at both ends of the pore, and a conductance value nominally higher than expected for a completely neutral pore. However, in the 'off' state (low conductance), a depletion zone is formed at the junction between the silicon nitride insulator and the gold conductor. This depletion zone leads to a very low conductance in the pore. These pores exhibit novel conductance behaviors that could be exploited in order to insert diode-like elements into ionic circuits. The physics and chemistry of induced charges on conductors present in the solution have seldom been studied, and the results of our experiments confirm that these charges and contribute to the conductance properties of the device just as static charges do.

6.2.2 Resistive pulse studies of mesoscale rods

In chapter 3, we explained how resistive pulse sensing can be extended to measure not only the volume of a passing particle, but the length of the passing particle as well. Particles probe the local pore radius as they translocate, and therefore we can view their resistive pulse amplitudes as 'maps' of the local pore interior. When particles with displacement lengths much shorter than the characteristic length scale of diameter undulations in the pore translocate, they create high resolution mappings of their environment. Oppositely, particles with long length displacements map the pore interior with low resolution. The resistive pulse signals of these long particles can be represented as a moving average of the resistive pulse signals of shorter particles, and by performing such a moving average on the signal of a short particle we can generate a simulated signal of a longer particle. We show that by performing moving averages of the signals of short particles for a variety of lengths, we can compare the resulting transformed signal with the raw signal of the long particle, and in doing so quantitatively measure the length o the unknown particle. In order to compare the similarity of two resistive pulses, we used a computational algorithm known as dynamic time warping. We tested this concept by performing experiments with polystyrene spheres, 'short' silica rods, and 'long' silica rods. We showed that at a qualitative level the resistive pulse signals of the short rods and long rods were very different, namely in that small scale features in the signals of the shorter rods were not present in the signals of the longer rods, in accordance with the previously described model. We employed dynamic time warping to make a quantitative comparison, and found that the distribution of the lengths of the long rods could be accurately recovered using this method. Finally, in the course of running the experiments with short rods we discovered the scale of their resistive pulse amplitudes was far larger than expected for their volumes. The discrepancy between expected resistive pulse amplitude and observed resistive pulse amplitude was as large as a factor of two. In order to explain this result, we considered a model where the rods were rotating extremely rapidly in the solution. This type of rapid rotation could 'stir' the local ion solution in their vicinity, reducing its effective conductivity. Furthermore, we argued that this type of rotation could be physically realizable due to the random undulations in the channel which create non-uniform electric fields, and therefore induce a large torque on the rods.

6.2.3 Hybrid resistive pulse-optical platform

Many equations exist for predicting the resistive pulse amplitudes of various particles, however the vast majority of these equations are only approximations that do not take into account geometry-dependent effects present in the channel. For instance, the equations for RP amplitude all assume channels with lengths much greater than their diameter, eliminating the confounding effects of the channel's entrance and exit. We argued that these effects may be important for certain channel geometries, and that often the ideal geometries used to derive analytical solutions may not always be realizable. In order to better understand the confounding position and geometry dependent effects, we devised an experimental platform using transparent planar microfluidic channels that were simultaneously measured with resistive pulse and optical imaging. Polystyrene bead suspensions were driven through the channel with a syringe, while the resistive pulse signal and video were simultaneously recorded. After the data was recorded, the two independent data streams were synchronized so that every frame in the camera data matched with a single data point in the resistive pulse signal corresponding to the same instant in time. The matched signals were then used to create 'resistance maps' of the channels, two-dimensional color maps where the color of each data point corresponds to the resistive pulse amplitude at that exact location. The resistance maps were used to explore positional effects of the resistive pulse amplitudes; for instance, we were able to directly show that translocation of particles off-axis yielded larger resistive pulse amplitudes, and that the amplitude does not attain its maximal value until the particle is well inside the channel. Additionally, we used the resistance map to study the positional dependence of resistive pulse amplitudes in channels with non-constant widths. In order to perform the previously mentioned steps, a library for analyzing the hybrid resistive pulse optical measurements was developed.

6.2.4 Particle deformability cytometry using resistive pulse sensing

In chapter 5, we explained how channels with central cavities can induce repeatable deformations of non-rigid particles, and developed a model for how the deformations would occur in the channel's geometry. Deformability if an important mechanical property of cells that can be used to discriminate between different types, and therefore the ability to rapidly and accurately measure cell deformability is a highly sought-after application. While the most obvious way to measure deformation is optically, we explain how deformation could be measured with a pure resistive pulse approach instead. Resistive pulse sensing is computationally lighter than optical imaging, and would allow for greater throughputs of cells while still allowing for online analysis. In order to test our model for cell deformations in cavitated channels, we performed experiments on two different cell types using the hybrid resistive pulse-optical platform introduced in chapter 4. We showed the observed deformations agreed with the predictions of our model. At the time of the writing of this thesis, the obtained results are still preliminary and the platform's development is ongoing. We briefly discussed the hurdles that would be necessary to overcome in order to realize a device capable of high-throughput cell deformation measurements using the resistive pulse signal alone, including tailoring the channel geometry and improving the signal-to-noise ratio of the current measurements.

6.3 Closing remarks

This dissertation is focused on advancing various applications involving ion conducting channels, especially in nanopores and in microfluidic channels. While most of the projects (but not all) were brought to a satisfying conclusion, much work remains to be done. It is the author's hope that future graduate students interested in one or more of the subjects presented will be able to use this thesis as a starting point and develop the ideas further.

Bibliography

[1] Y. Astier, O. Braha, and H. Bayley. Toward single molecule dna sequencing: direct identification of ribonucleoside and deoxyribonucleoside 5-monophosphates by using an engineered protein nanopore equipped with a molecular adapter. *J. Am. Chem. Soc.*, 128(5):1705–1710, 2006. PMID: 16448145.

[2] L. I. Berge, J. Feder, and T. Jøssang. A novel method to study singleparticle dynamics by the resistive pulse technique. *Rev. Sci. Instrum.*, 60(8):2756–2763, 1989.

[3] L. I. Berge, T. Jossang, and J. Feder. Off-axis response for particles passing through long apertures in coulter-type counters. *Meas. Sci. Technol.*, 1(6):471, 1990.

[4] L. Bocquet and E. Charlaix. Nanofluidics, from bulk to interfaces. *Chem. Soc. Rev.*, 39:1073–1095, 2010.

[5] W. Choi, Z. W. Ulissi, S. F. E. Shimizu, D. O. Bellisario, M. D. Ellison, and M. S. Strano. Diameter-dependent ion transport through the interior of isolated single-walled carbon nanotubes. 4:2397 EP –, Sep 2013. Article.

[6] W. H. Coulter. Means for counting particles suspended in a fluid, 1953.

[7] R. W. DeBlois and C. P. Bean. Counting and sizing of submicron particles by the resistive pulse technique. *Rev. Sci. Instrum.*, 41(7):909–916, 1970.

[8] R. W. DeBlois, C. P. Bean, and R. K. Wesley. Electrokinetic measurements with submicron particles and pores by the resistive pulse technique. *J. Colloid Interface Sci.*, 61(2):323–335, 1977.

[9] R. W. DeBlois and R. K. Wesley. Sizes and concentrations of several type c oncornaviruses and bacteriophage t2 by the resistive-pulse technique. *J. Virol.*, 23(2):227–233, Aug 1977.

[10] D. C. Duffy, J. C. McDonald, O. J. A. Schueller, and G. M. Whitesides. Rapid prototyping of microfluidic systems in poly(dimethylsiloxane). *Anal. Chem.*, 70(23):4974–4984, 1998.

[11] E. Elson. Cellular mechanics as an indicator of cytoskeletal structure and function. *Annual Review of Biophysics and Biophysical Chemistry*, 17(1):397–430, 1988. PMID: 3293593.

[12] J. Feng, K. Liu, R. D. Bulushev, S. Khlybov, D. Dumcenco, A. Kis, and A. Radenovic. Identification of single nucleotides in mos2 nanopores. *Nat. Nanotechnol.*, 10(12):1070–1076, Dec 2015.

[13] D. A. Fletcher and R. D. Mullins. Cell mechanics and the cytoskeleton. *Nature*, 463(7280):485–492, Jan 2010. 20110992[pmid].

[14] M. J. Fulwyler. Electronic separation of biological cells by volume. *Science*, 150(3698):910–911, 1965.

[15] D. Golibersuch. Observation of aspherical particle rotation in poiseuille flow via the resistance pulse technique: I. application to human erythrocytes. *Biophys. J.*, 13(3):265–280, 1973.

[16] D. R. Gossett, H. T. K. Tse, S. A. Lee, Y. Ying, A. G. Lindgren, O. O. Yang, J. Rao, A. T. Clark, and D. Di Carlo. Hydrodynamic stretching of single cells for large population mechanical phenotyping. *Proc. Natl. Acad. Sci. U. S. A.*, 109(20):7630–7635, 2012.

[17] Z. D. Harms, K. B. Mogensen, P. S. Nunes, K. Zhou, B. W. Hildenbrand, I. Mitra, Z. Tan, A. Zlotnick, J. P. Kutter, and S. C. Jacobson. Nanofluidic devices with two pores in series for resistive-pulse sensing of single virus capsids. *Anal. Chem.*, 83(24):9573–9578, 2011.

[18] R. R. Henriquez, T. Ito, L. Sun, and R. M. Crooks. The resurgence of coulter counting for analyzing nanoscale objects. *Analyst*, 129:478–482, 2004.

[19] P. Hinkle, T. M. Westerhof, Y. Qiu, D. J. Mallin, M. L. Wallace, E. L. Nelson, P. Taborek, and Z. S. Siwy. A hybrid resistive pulse-optical detection platform for microfluidic experiments. *Scientific Reports*, 7(1):10173, 2017.

[20] L. M. Innes, C.-H. Chen, M. Schiel, M. Pevarnik, F. Haurais, M. E. Toimil-Molares, I. Vlassiouk, L. Theogarajan, and Z. S. Siwy. Velocity profiles in pores with undulating opening diameter and their importance for resistive-pulse experiments. *Anal. Chem.*, 86(20):10445–10453, 2014.

[21] Z. Jiang, M. Mihovilovic, J. Chan, and D. Stein. Fabrication of nanopores with embedded annular electrodes and transverse carbon nanotube electrodes. *J. Phys.: Condens. Matter*, 22(45):454114, 2010.

[22] J. Kasianowicz, E. Brandin, D. Branton, and D. Deamer. Characterization of individual polynucleotide molecules using a membranechannel. *Proc. Natl. Acad. Sci. U. S. A.*, 93(24):13770–13773, 1996.

[23] E. Keogh and C. A. Ratanamahatana. Exact indexing of dynamic time warping. *Knowledge and Information Systems*, 7(3):358–386, Mar 2005.

[24] M. J. Kim, B. McNally, K. Murata, and A. Meller. Characteristics of solid-state nanometre pores fabricated using a transmission electron microscope. *Nanotechnology*, 18(20):205302, 2007.

[25] B. J. Kirby. *Micro- and Nanoscale Fluid Mechanics.* Cambridge University Press, 2010.

[26] D. Kozak, W. Anderson, R. Vogel, S. Chen, F. Antaw, and M. Trau. Simultaneous size and -potential measurements of individual nanoparticles in dispersion using size-tunable pore sensors. *ACS Nano*, 6(8):6990–6997, 2012.

[27] A. Kuijk, A. van Blaaderen, and A. Imhof. Synthesis of monodisperse, rodlike silica colloids with tunable aspect ratio. *J. Am. Chem. Soc.*, 133(8):2346–2349, 2011. PMID: 21250633.

[28] J. Lin, D. Kim, H. T. Tse, P. Tseng, L. Peng, M. Dhar, S. Karumbayaram, and D. Di Carlo. High-throughput physical phenotyping of cell differentiation. *Microsystems and Nanoengineering*, 3:17013 EP –, May 2017. Article.

[29] L. Luo, S. R. German, W.-J. Lan, D. A. Holden, T. L. Mega, and H. S. White. Resistive-pulse analysis of nanoparticles. *Annu. Rev. Anal. Chem.*, 7(1):513–535, 2014. PMID: 24896310.

[30] A. McMullen, H. W. de Haan, J. X. Tang, and D. Stein. Stiff filamentous virus translocations through solid-state nanopores. *Nat. Commun.*, 5:1–10, Jun 2014.

[31] J. Menestrina, C. Yang, M. Schiel, I. Vlassiouk, and Z. S. Siwy. Charged particles modulate local ionic concentrations and cause formation of positive peaks in resistive-pulse-based detection. *The Journal of Physical Chemistry C*, 118(5):2391–2398, 2014.

[32] A. Mietke, O. Otto, S. Girardo, P. Rosendahl, A. Taubenberger, S. Golfier, E. Ulbricht, S. Aland, J. Guck, and E. Fischer-Friedrich. Extracting cell stiffness from real-time deformability cytometry: Theory and experiment. *Biophys. J.*, 109(10):2023 – 2036, 2015.

[33] M. Nishizawa, V. P. Menon, and C. R. Martin. Metal nanotubule membranes with electrochemically switchable ion-transport selectivity. *Science*, 268(5211):700–702, 1995.

[34] O. Otto, P. Rosendahl, A. Mietke, S. Golfier, C. Herold, D. Klaue, S. Girardo, S. Pagliara, A. Ekpenyong, A. Jacobi, M. Wobus, N. Topfner, U. F. Keyser, J. Mansfeld, E. Fischer-Friedrich, and J. Guck. Real-time deformability cytometry: on-the-fly cell mechanical phenotyping. *Nat Meth*, 12(3):199–202, Mar 2015. Brief Communication.

[35] A. J. Pascall and T. M. Squires. Induced charge electro-osmosis over controllably contaminated electrodes. *Phys. Rev. Lett.*, 104:217–252, Feb 2010.

[36] M. Pevarnik, K. Healy, M. E. Toimil-Molares, A. Morrison, S. E. Ltant, and Z. S. Siwy. Polystyrene particles reveal pore substructure as they translocate. *ACS Nano*, 6(8):7295–7302, 2012.

[37] J.-F. Pietschmann, M.-T. Wolfram, M. Burger, C. Trautmann, G. Nguyen, M. Pevarnik, V. Bayer, and Z. Siwy. Rectification properties of conically shaped nanopores: consequences of miniaturization. *Phys. Chem. Chem. Phys.*, 15:16917–16926, 2013.

[38] Y. Qiu, P. Hinkle, C. Yang, H. E. Bakker, M. Schiel, H. Wang, D. Melnikov, M. Gracheva, M. E. Toimil-Molares, A. Imhof, and Z. S. Siwy. Pores with longitudinal irregularities distinguish objects by shape. *ACS Nano*, 9(4):4390–4397, 2015. PMID: 25787224.

[39] T. Sannomiya, H. Dermutz, C. Hafner, J. Vrs, and A. B. Dahlin. Electrochemistry on a localized surface plasmon resonance sensor. *Langmuir*, 26(10):7619–7626, 2010.

[40] R. B. Schoch, J. Han, and P. Renaud. Transport phenomena in nanofluidics. *Rev. Mod. Phys.*, 80:839–883, Jul 2008.

[41] Z. Siwy and F. Fornasiero. Improving on aquaporins. *Science*, 357(6353):753–753, 2017.

[42] R. M. M. Smeets, U. F. Keyser, N. H. Dekker, and C. Dekker. Noise in solid-state nanopores. *Proceedings of the National Academy of Sciences*, 105(2):417–421, 2008.

[43] W. R. Smythe. Flow around a spheroid in a circular tube. *Phys. Fluids*, 7(5):633–638, 1964.

[44] W. R. Smythe. Offaxis particles in coulter type counters. *Rev. Sci. Instrum.*, 43(5):817–818, 1972.

[45] J. Sonnefeld. Determination of surface charge density parameters of silicon nitride. *Colloids and Surfaces A: Physicochemical and Engineering Aspects*, 108(1):27 – 31, 1996.

[46] T. M. Squires and M. Z. Bazant. Induced-charge electro-osmosis. *J. Fluid Mech.*, 509:217252, June 2004.

[47] M. N. Starodubtseva. Mechanical properties of cells and ageing. *Ageing Research Reviews*, 10(1):16 – 25, 2011. Cell Motility and Ageing.

[48] A. J. Storm, J. H. Chen, X. S. Ling, H. W. Zandbergen, and C. Dekker. Fabrication of solid-state nanopores with single-nanometre precision. *Nat. Mater.*, 2(8):537–540, Aug 2003.

[49] S. P. Surwade, S. N. Smirnov, I. V. Vlassiouk, R. R. Unocic, G. M. Veith, S. Dai, and S. M. Mahurin. Water desalination using nanoporous single-layer graphene. *Nat Nano*, 10(5):459–464, May 2015. Article.

[50] F. Traversi, C. Raillon, S. Benameur, K. Liu, S. Khlybov, M. Tosun, D. Krasnozhon, A. Kis, and A. Radenovic. Detecting the translocation of dna through a nanopore using graphene nanoribbons. *Nat. Nanotechnol.*, 8(12):939–945, Dec 2013.

[51] M. Tsutsui, Y. He, K. Yokota, A. Arima, S. Hongo, M. Taniguchi, T. Washio, and T. Kawai. Particle trajectory-dependent ionic current blockade in low-aspect-ratio pores. *ACS Nano*, 10(1):803–809, 2016.

[52] M. Tsutsui, S. Hongo, Y. He, M. Taniguchi, N. Gemma, and T. Kawai. Single-nanoparticle detection using a low-aspect-ratio pore. *ACS Nano*, 6(4):3499–3505, 2012.

[53] R. H. Tunuguntla, R. Y. Henley, Y.-C. Yao, T. A. Pham, M. Wanunu, and A. Noy. Enhanced water permeability and tunable ion selectivity in subnanometer carbon nanotube porins. *Science*, 357(6353):792–796, 2017.

[54] B. M. Venkatesan and R. Bashir. Nanopore sensors for nucleic acid analysis. *Nat. Nanotechnol.*, 6(10):615–624, Oct 2011.

[55] I. Vlassiouk and Z. S. Siwy. Nanofluidic diode. *Nano Lett.*, 7(3):552–556, 2007. PMID: 17311462.

[56] P. Waduge, R. Hu, P. Bandarkar, H. Yamazaki, B. Cressiot, Q. Zhao, P. C. Whitford, and M. Wanunu. Nanopore-based measurements of protein size, fluctuations, and conformational changes. *ACS Nano*, 11(6):5706–5716, 2017. PMID: 28471644.

[57] M. Wanunu. Nanopores: A journey towards {DNA} sequencing. *Phys. Life Rev.*, 9(2):125–158, 2012.

[58] W. Xu, R. Mezencev, B. Kim, L. Wang, J. McDonald, and T. Sulchek. Cell stiffness is a biomarker of the metastatic potential of ovarian cancer cells. *PLOS ONE*, 7(10):1–12, 10 2012.

[59] K. Zhou, L. Li, Z. Tan, A. Zlotnick, and S. C. Jacobson. Characterization of hepatitis b virus capsids by resistive-pulse sensing. *J. Am. Chem. Soc.*, 133(6):1618–1621, 2011.

[60] K. H. L. M. I. M. S. M. P. Zuzanna S. Siwy, Kenneth J. Shea. Faster resistive-pulse sensing together with physical and mechanical characterization of particles and cells, 2014.